DISSERTATION

Optical Properties of Semiconductor Nanostructures

ausgeführt zum Zwecke der Erlangung des akademischen Grades
eines Doktors der technischen Wissenschaften

eingereicht an der Technischen Universität Wien
Fakultät für Elektrotechnik und Informationstechnik
von

Mahdi Moradinasab

Wien, im März 2015 _____

Abstract

Nanostructures made from graphene and graphene related materials or from traditional compound semiconductors are promising building blocks for light sources and detectors in a broad frequency range. By cutting graphene into a few nanometer-wide nanoribbon, the bandgap can be tuned to a certain extent by the confinement of the electronic wave function. One dimensional graphene nanoribbons and superlattices provide precisely tunable energy gaps for optical applications. The optical properties of such nanostructures are investigated. The nearest neighbor tight-binding model is employed to describe the electronic bandstructure. In addition, an analytical solution for the dispersion relation and the wave functions are introduced in this study. Based on developed models, selection rules for optical transitions of each structure are obtained. The results are verified against first principles calculations. Single-layer hexagonal boron nitride can be patterned into nanoribbons which exhibit large enough band gaps and qualitatively different properties from those of graphene related materials. Embedding graphene nanostructures in boron nitride lattices increases flexibility of bandgap engineering for optical transitions. The optical properties of such embedded graphene nanoribbons and superlattices are investigated. The optical spectrum, the quantum efficiency, and the photoresponsivity of those nanostructures are evaluated and their application in photodetector devices is investigated. The role of line-edge roughness on the optical properties of such devices is carefully studied.

Since the intersubband transition energy can be varied to cover a broad wavelength range, intersubband optoelectronic devices are very agile in frequency. For a quantum cascade laser, both the emission frequency and optical gain can be tailored by design of the heterostructure. Employing the flexibility offered by bandstructure engineering, we present an approach to use quantum cascade lasers for ultrashort pulse generation in the infrared and terahertz frequency range. Laser design parameters, including the barrier and well thicknesses and applied electric field are modified for maximizing the laser performance and desired dynamic operation. For this purpose, particle swarm optimization — a multi-variable multi-objective optimization algorithm — is employed. For short pulse generation, we study passive mode locking in a ring cavity quantum cascade laser where the instability condition is introduced by means of a saturable absorber. The effects of saturable absorber and pumping strength on the instability threshold are investigated. Various quantum cascade laser designs, including three-well vertical, superlattice, and terahertz designs, are employed in the optimization study. A large optical gain below the instability threshold is achieved for the optimized quantum cascade laser designs. To analyze the optimized structure

TU Bibliothek
Your knowledge hub
WIEN

above the instability threshold, numerical calculations based on the Maxwell-Bloch equations are performed. A finite-difference discretization scheme is employed to find the evolution of electric field, polarization, and population inversion in the spatial and time domain. The results indicate side-mode instabilities due to Risken-Nummedal-Graham-Haken-like instability.

Kurzfassung

Nanostrukturen aus Graphen und verwandten Materialien oder aus traditionellen Verbindungshalbleitern bilden die Grundbausteine für Lichtquellen und -detektoren in einem breiten Frequenzspektrum. Strukturiert man Graphen in Streifen von wenigen Nanometern Breite, sogenannte Nanoribbons, so entsteht durch die Einschränkung der elektronischen Wellenfunktion eine Bandlücke. Eindimensionale Graphen-Nanoribbons und -Übergitter ermöglichen es, die Bandlücke für optische Anwendungen genau einzustellen. In dieser Arbeit werden die optischen Eigenschaften solcher Nanostrukturen untersucht. Um die elektronische Bandstruktur zu beschreiben, wird die Tight-Binding-Methode verwendet. Es werden analytische Lösungen für die Dispersionsrelation und die Wellenfunktion angegeben. Aus den entwickelten Modellen erhält man Auswahlregeln für die optischen Übergänge in konkreten Strukturen. Die Ergebnisse werden anhand von ab initio Rechnungen verifiziert. Nanoribbons aus einatomigen Bornitrid-Schichten weisen eine wesentlich größere Bandlücke als Graphen-basierte Nanostrukturen auf. Durch Einbetten von Graphen-Nanostrukturen in Bornitrid kann die Bandlücke für optische Übergänge noch flexibler eingestellt werden. Die optischen Eigenschaften von eingebetteten Graphen-Nanoribbons und -Übergittern werden untersucht. Dazu zählen die Spektralverteilung, die Quanteneffizienz und die Empfindlichkeit. Auch der Einfluss der Kantenrauigkeit auf die optischen Eigenschaften wird sorgfältig untersucht. Die mögliche Anwendung dieser Nanostrukturen in Photodetektoren wird beleuchtet.

Da die Übergangsenergie zwischen Subbändern und die damit verbundene Wellenlänge stark variiert werden kann, können Intersuband-optoelektronische Bauelemente für Frequenzen in einem großen Bereich ausgelegt werden. In einem Quantenkaskadenlaser können sowohl die Emissionsfrequenz als auch die optische Verstärkung durch den geeigneten Entwurf der Heterostruktur eingestellt werden. Es wird ein spezielles Quantenkaskadenlaser-Design vorgestellt, das zur Erzeugung ultrakurzer Pulse im Infrarot- und Terahertzbereich geeignet ist. Dabei werden die Entwurfparameter wie Schichtdicken und elektrische Feldstärke so eingestellt, dass die Lasereigenschaften optimiert werden und gleichzeitig das gewünschte dynamische Verhalten gewährleistet wird. Zu diesem Zweck wird das Verfahren der Partikelschwarm-Optimierung, einem mehrkriteriellen Optimierungsalgorithmus, angewendet. Für die Erzeugung ultrakurzer Pulse wird die passive Modenkopplung in einem Quantumkaskadenlaser mit einem Ringresonator untersucht, bei dem die Instabilitätsbedingung durch Einbringen eines sättigbaren Absorbers erzeugt wird. Der Einfluss des Absorptionskoeffizienten und der Pumpstärke auf die Stabilitätsgrenze wird untersucht. In der

Optimierungsstudie werden drei verschiedene Quantumkaskadenlaser-Designs verwendet: ein Drei-Wannen vertikales Design, ein Übergitter-Design und ein Terahertz-Design. Das optimierte Design weist eine gute optische Verstärkung unterhalb der Stabilitätsgrenze auf. Um die optimierte Struktur jenseits der Stabilitätsgrenze zu analysieren, werden die Maxwell-Bloch Gleichungen numerisch gelöst. Das Zeitverhalten des elektrischen Feldes, der Polarisation und der Besetzungsinversion wird mit Hilfe eines Finite-Differenzen-Verfahrens numerisch bestimmt. Die Ergebnisse zeigen, dass in den untersuchten Strukturen die Risken-Nummendal-Graham-Haken- Instabilität auftritt.

Acknowledgment

I thank all the kind people who helped and supported me to do this doctoral thesis.

First and foremost, I would like to express my sincere gratitude to my supervisor Prof. Hans Kosina, for the continuous support of my PhD study and research, for his patience, help, and motivation. My sincere thanks goes to Dr. Mahdi Pourfath for his help and support in all the time of research and writing of this thesis.

The Institute for Microelectronics has supported me to complete my thesis. My special thanks goes to Prof. Siegfried Selberherr and Prof. Erasmus Langer for providing excellent working conditions, for the possibility to work at such a prestigious place, and for the opportunity to attend several international scientific conferences.

I also want to express my gratitude to other members of the institute. I would like to thank the following (in alphabetical order):
Oskar Baumgartner, Markus Bina, Hajdin Ceric, Johann Cervenka, Raffaele Alberto Coppeta, Paul Ellinghaus, Lado Filipovic, Lidija Filipovic, Joydeep Ghosh, Klaus-Tibor Grasser, Alexander Grill, Wolfgang Gös, Ewald Haslinger, Philipp Hehenberger, Yury Illarionov, Markus Jech, Markus Kampl, Hossein Karamitaheri, Manfred Katterbauer, Hiwa Mahmoudi, Alexander Makarov, Andreas Morhammer, Mihail Nedjalkov, Neophytos Neophytou, Roberto Orio, Dmitry Osintsev, Vassil Palankovski, Santo Papaleo, Marco Rovitto, Florian Rudolf, Karl Rupp, Gerhard Rzepa, Franz Schanovsky, Prateek Sharma, Anderson Singulani, Zlatan Stanojevic, Viktor Sverdlov, Michael Thesberg, Oliver Triebl, Stanislav Tyaginov, Bianka Ullmann, Michael Waltl, Josef Weinbub, Yannick Wimmer, Thomas Windbacher, Renate Winkler, and Wolfhard Zisser.

I also want to thank my friends, especially Behzad Ebrahimi, who accompanied me during my student days and curiously followed my life as a researcher.

Last but not the least, I would like to thank my parents, for supporting me spiritually throughout my life.

Contents

List of Figures

List of Tables

List of Abbreviations

AGNR	$\cdots$	Armchair graphene nanoribbon
AGNRBN	$\cdots$	Armchair graphene nanoribbon in boron nitride
BNSL	$\cdots$	Boron-nitride-passivated armchair graphene nanoribbons superlattice
CNT	$\cdots$	Carbon nanotube
cw	$\cdots$	continuous-wave
DFT	$\cdots$	Density functional theory
DOS	$\cdots$	Density of states
GGA	$\cdots$	Generalised gradient approximation
GNR	$\cdots$	Graphene nanoribbon
FIR	$\cdots$	Far-infrared
HSL	$\cdots$	Hydrogen-passivated armchair graphene nanoribbons superlattice
ISB	$\cdots$	Intersubband
JDOS	$\cdots$	Joint density of states
LDA	$\cdots$	Local density approximation
LDOS	$\cdots$	Local density of states
LER	$\cdots$	Line-edge-roughness
MC	$\cdots$	Monte Carlo
MIR	$\cdots$	Mid-Infrared
NEGF	$\cdots$	Non-equilibrium Green's function
QCD	$\cdots$	Qantum cascade detector
QCL	$\cdots$	Qantum cascade laser
QW	$\cdots$	Qantum well
3QW	$\cdots$	Three-well
RNGH	$\cdots$	Risken-Nummedal-Graham-Haken
SA	$\cdots$	Saturable absorber
SIESTA	$\cdots$	Spanish initiative for electronic simulations with thousands of atoms
SL	$\cdots$	Superlattice
TB	$\cdots$	Tight-binding
THz	$\cdots$	Terahertz
ZGNR	$\cdots$	Zigzag graphene nanoribbon

1. Introduction

For more than 35 years, semiconductor nanostructures have been investigated for a large number of applications in technology including lasers, photodetectors, light emitting diodes, and transistors. Nowadays, these structures are considered to be even more perspective for novel applications. This is why after such a long period the intensive research performed in this field even grows further.

If the geometrical extent of a semiconductor, typically embedded in the matrix of another semiconductor, is reduced in one, two or three directions of space below the size of the "de Broglie wavelength" of a charge carrier which is on the order of a few nanometers, it is called a nanostructure [1].

The electrical and optical properties of low-dimensional structures, including their interactions such as electron-electron, electron-hole, and electron-photon interaction, depend qualitatively on the dimensionality of the structure and quantitatively on details of the geometry of the structure such as size and shape, and on the distribution of the atoms inside [1]. The electronic properties in turn control the linear and nonlinear optical and electronic transport properties. Thus "geometrical architecture" opens enormous opportunities for designing completely novel materials or heterostructures.

The far-infrared (FIR) frequency range is roughly defined as 30-300 μm or 4-40 meV and is often referred to as the terahertz frequency range 1-10 THz [2–4], see Fig. 1.1. FIR electromagnetic radiation is important in many applications such as radio astronomy, environmental monitoring, plasmon diagnostics, laboratory spectroscopy, telecommunications, medicine etc. and in the characterization of nanoscale condensed matter materials. In recent years, the generation, propagation and detection of FIR electromagnetic radiation using two-dimensional semiconductor systems or other semiconductor nanostructures has become one of the most rapidly expanding fields in photonics, optoelectronics and condensed matter physics. However, the terahertz frequency range cannot be directly accessed. Diode lasers are ideal sources because they are cheap, compact and very efficient. However, the semiconductor bandgap places a limitation on emission frequency. The longest-wavelength diode lasers ($\sim 30\mu m$) are based on narrow gap lead-salt semiconductors [5]. While these lead-salt lasers have been quite successful for high resolution spectroscopy, they are still limited to cryogenic operation and provide relatively low power. On the other end of the spectrum, semiconductor transistors can be used to generate 100 GHz oscillators [6]. Molecular gas lasers are one of the practical laser sources for the FIR, but they have limited
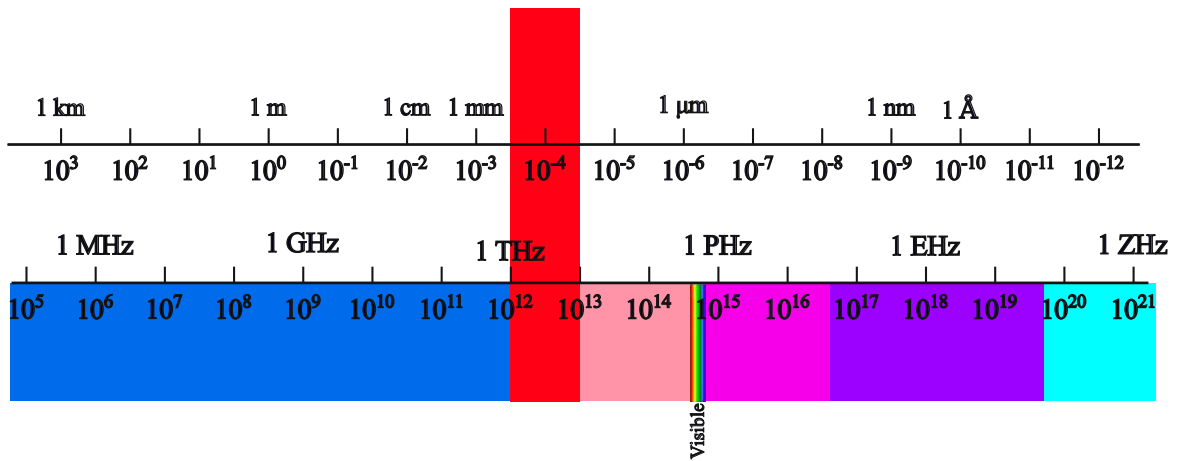
Figure 1.1.: The terahertz spectrum is located between the optical domain and the microwave domain.

lasing frequencies. They are also somewhat unwieldy as they require high voltage supplies and are usually rather bulky.

Semiconductor nanostructures are most promising candidates to solve the lack of suitable sources and detectors in the FIR frequency range. Graphene nanostructures [7–12] and quantum cascade devices [13–22] promise efficient operation in a broad frequency range. Electronically, pure graphene is a gapless semiconductor. Since the potential usefulness of graphene in electronic and photonic applications cannot be fully tapped unless a bandgap can be engineered, bandgap engineering of graphene has attracted much research interest recently. In gapped graphene, a vertical linear response peak is predicted when the photon frequency matches the bandgap energy. Stripped into a few nanometer-wide graphene nanoribbon, the bandgap can be tuned to a certain extent by the confinement of electronic wave function. One dimensional graphene nanoribbons and superlattices provide precise tunable energy gaps for optical applications.

Bandgap engineering of graphene-based structures could result in devices operating in the terahertz domain. Bandgap engineering for terahertz operation is also possible in intersubband quantum cascade heterostructures [23]. Intersubband optical devices have several advantages over conventional interband semiconductor devices. Most useful is the fact that the emission frequency is determined by the design of the heterostructure and can hence be tailored to the application. This is especially useful for infrared applications where small bandgap materials become difficult to find and work with. Also, since the envelope functions extend over a well (tens of Angstroms), the dipole moment for the intersubband transition is typically several orders of magnitude larger than that of an atomic transition.

1.1. Graphene-Based Structures

In October 2004, graphene, a one-atomic layer of carbon with a honeycomb structure, started a revolution in science and technology. Physicists reported that they had prepared graphene and observed the electric field effect in their samples [24]. Shortly after, this new material attracted the attention in many areas of research including condensed matter, material physics, chemistry, and device physics. Graphene-based structures such as graphene nanoribbons (GNRs) [25], nanorods [26] quantum dots [27], and p-n junctions [28] have been successfully fabricated.

To understand graphene in more details, it is useful to consider it as the single layer limit of graphite (Fig.1.2). In this light, the extraordinary properties of honeycomb carbon are not really new. Abundant and naturally occurring, graphite has been known as a mineral for nearly 500 years. Even in the middle ages, the layered morphology and weak dispersion forces between adjacent sheets were utilized to make marking instruments, much in the same way that we use graphite in pencils today. More recently, these same properties have made graphite an ideal material for use as a dry lubricant, along with the similarly structured but more expensive compounds hexagonal boron nitride and molybdenum disulfide [29].

An extraordinarily high carrier mobility of more than 2×10^5 cm^2/Vs [30–32] makes graphene a major candidate for future electronic applications. Today a growing number of groups are successfully fabricating graphene transistors [33]. Major chip-makers are now active in graphene research and the International Technology Roadmap for Semiconductors, the strategic planning document for the semiconductor industry, considers graphene to be among the candidate materials for post-silicon electronics [34] and terahertz applications [35]. Graphene is also regarded as a pivotal material in the emerging field of spin electronics due to spin coherence even at room temperature [36, 37].

One of the many interesting properties of Dirac electrons in graphene is the drastic change of the conductivity of graphene-based structures with the confinement of electrons. Structures that realize this behavior are carbon nanotubes (CNTs) and graphene nanoribbons (GNRs), which impose periodic and zero boundary conditions, respectively, on the transverse electron wave-vector. In CNT-based devices control over the chirality and diameter and thus of the associated electronic bandgap remains a major technological problem. GNRs do not suffer from this problem and are thus recognized as promising building blocks for nanoelectronic devices [38]. GNRs less than 10nm wide with ultrasmooth edges have been fabricated [39].

GNRs can be considered as a graphene sheet tailored along a certain direction and can be accordingly classified as of armchair or zigzag shape, see Fig. 1.3(a) and (b). Tight-binding calculations predict that ZGNRs are always metallic while AGNRs may be either metallic or semiconducting depending on their direction and width [40, 41]. The edges of GNRs can significantly affect the electronic properties of the ribbon. In the
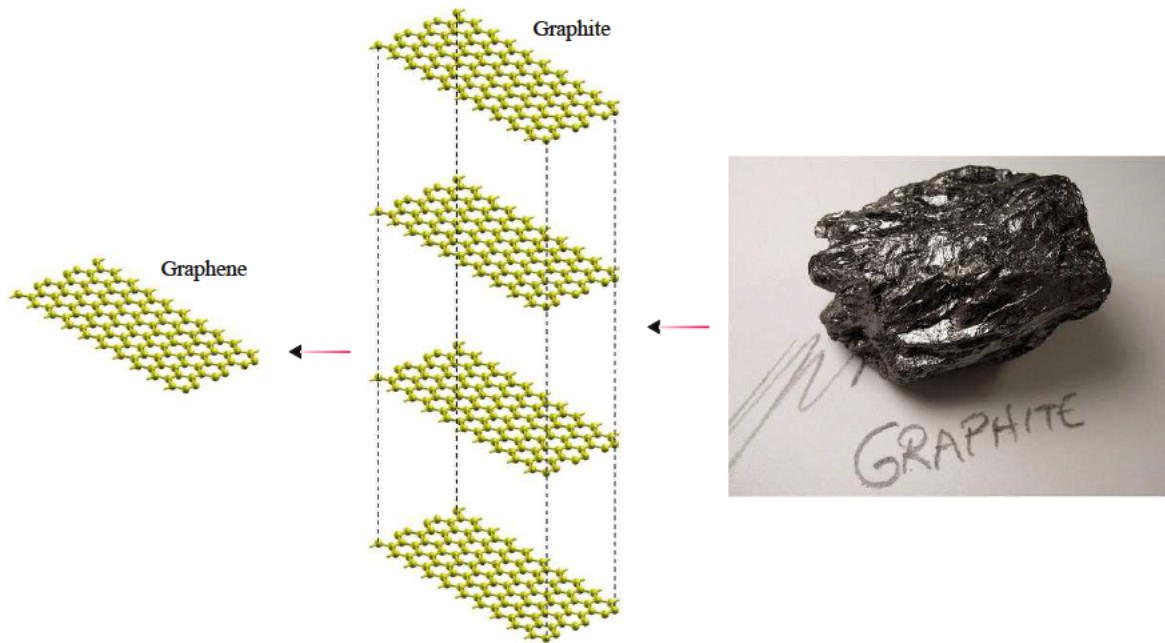
Figure 1.2.: Graphene is a single layer honeycomb lattice of carbon atoms. Graphite can be viewed as a stack of graphene layers.

electronic band structure of GNRs with zigzag edges a flat band, which corresponds to localized states at the edges, appears around the Fermi level [41, 42]. However, such states do not appear in GNRs with armchair edges (AGNRs) [41].

The controllable alteration of graphene by high-precision lithography [39, 43, 44] and chemical functionalization [45] has enabled modulation of the electronics, optical and thermal properties of these structures. A recent experimental study has reported ultra-smooth patterning of graphene nanoribbons with modulated widths which can be regarded as finite segments of GNR-based superlattices [39], see Fig. 1.3(c). Such structures can behave as multiple quantum wells and exhibit interesting quantum effects [46] such as resonant tunneling [47].

Due to possible application in nanoelectronics [38], photonics [48, 49], and spintronics [50], intensive scientific research is being carried out on graphene-based structures.

1.1.1. Electronic Properties

Graphene is composed of carbon atoms arranged in a hexagonal structure, as shown in Fig. 1.4. The structure can be seen as a triangular lattice with a basis of two atoms per unit cell. The lattice vectors can be written as

$$\mathbf{a_1} = \frac{a}{2}(3, \sqrt{3}), \ \mathbf{a_2} = \frac{a}{2}(3, -\sqrt{3}) \tag{1.1}$$

4
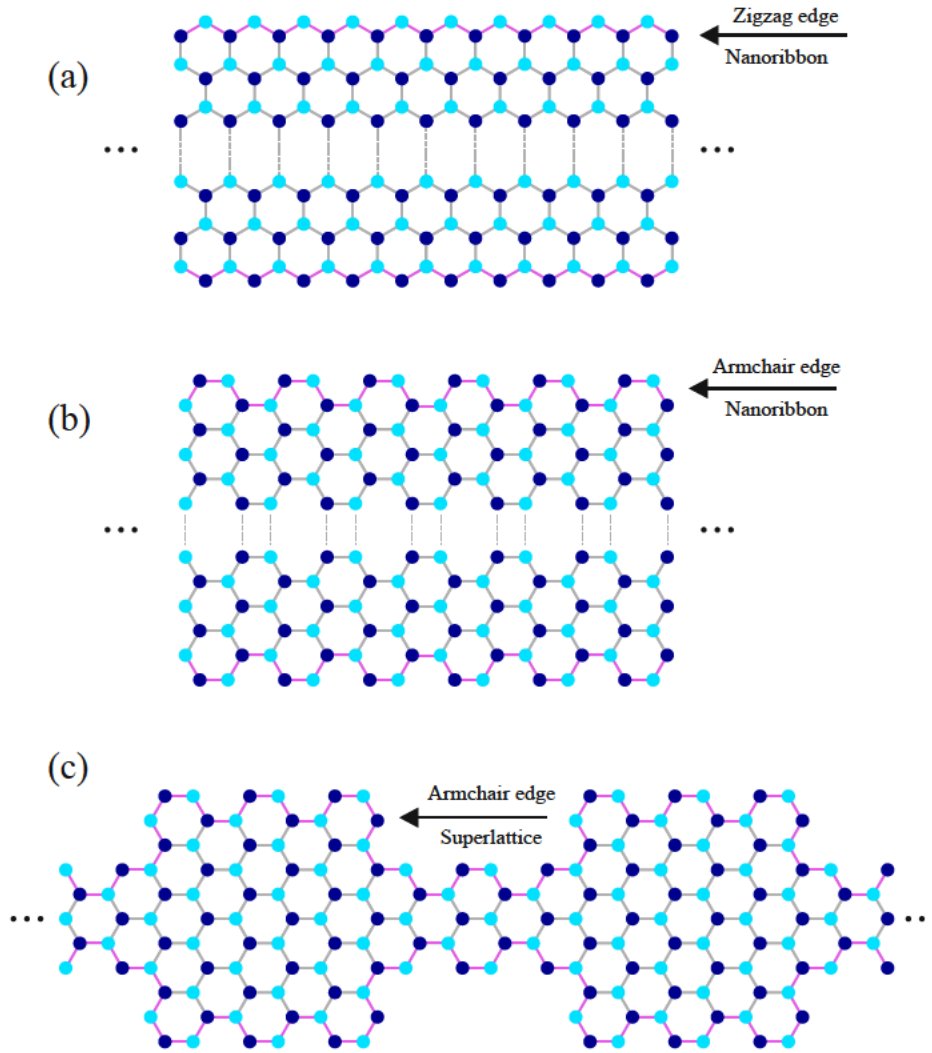
Figure 1.3.: Schematic of (a) zigzag and (b) armchair edge configurations of GNRs. The position of the edge is indicated by the pink line. (c) An armchair edge graphene superlattice structure.

where $a \approx 1.42$ Å is the carbon-carbon bond length. The reciprocal lattice vectors are given by

$$\mathbf{b_1} = \frac{2\pi}{3a}(1, \sqrt{3}), \ \mathbf{b_2} = \frac{2\pi}{3a}(1, -\sqrt{3}) \tag{1.2}$$

Of particular importance for the physics of graphene are the two points K and K′ at the corners of the Brillouin zone. These are named Dirac points for reasons that will become clear later. Their positions in momentum space are given by

$$\mathbf{K} = \left(\frac{2\pi}{3a}, \frac{2\pi}{3\sqrt{3}a}\right), \ \mathbf{K'} = \left(\frac{2\pi}{3a}, -\frac{2\pi}{3\sqrt{3}a}\right) \tag{1.3}$$

5
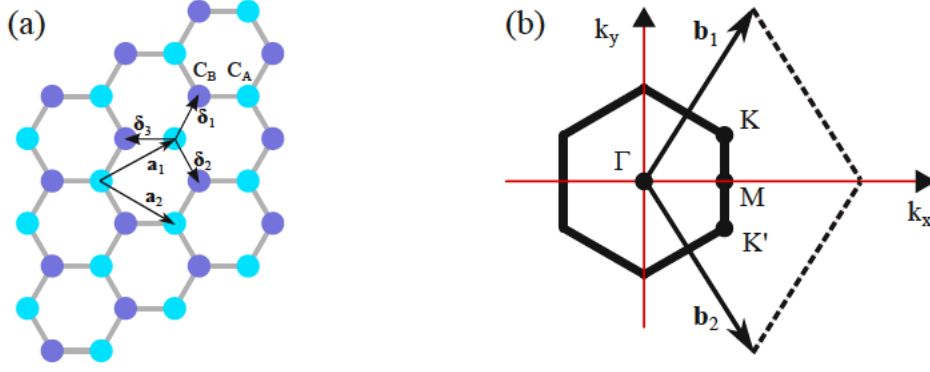
Figure 1.4.: Honeycomb lattice and its Brillouin zone. (a) Lattice structure of graphene, composed of two interpenetrating triangular lattices ($\mathbf{a_1}$ and $\mathbf{a_2}$ are the lattice unit vectors, and δ_i, $i = 1, 2, 3$ are the nearest-neighbor vectors). (b) Corresponding Brillouin zone. The Dirac cones are located at the K and K' points.

The three nearest-neighbor vectors in real space are

$$\boldsymbol{\delta_1} = \frac{a}{2}(1, \sqrt{3}), \ \boldsymbol{\delta_2} = \frac{a}{2}(1, -\sqrt{3}), \ \boldsymbol{\delta_3} = -a(1,0) \tag{1.4}$$

while the six second-nearest neighbors are located at $\boldsymbol{\delta'_1} = \pm\mathbf{a_1}$, $\boldsymbol{\delta'_2} = \pm\mathbf{a_2}$, $\boldsymbol{\delta'_3} = \pm(\mathbf{a_2} - \mathbf{a_1})$. The tight-binding Hamiltonian for electrons in graphene considering that electrons can hop to both nearest- and next-nearest-neighbor atoms has the form (we use units such that $\hbar = 1$)

$$H = -t \sum_{<i,j>,\sigma} \left(a_{\sigma,i}^\dagger b_{\sigma,i} + H.c. \right) - t' \sum_{\ll i,j \gg,\sigma} \left(a_{\sigma,i}^\dagger a_{\sigma,i} + b_{\sigma,i}^\dagger b_{\sigma,i} + H.c. \right), \tag{1.5}$$

where $a_{\sigma,i}$ annihilates an electron with spin σ ($\sigma = \uparrow, \downarrow$) and $a_{\sigma,i}^\dagger$ creates an electron with spin σ on site R_i on sublattice A. An equivalent definition is used for sublattice B. The nearest-neighbor hopping energy between different sublattices is $t \approx 2.7$ eV, and t' is the next nearest-neighbor hopping energy in the same sublattice. The value of t' is not well known but ab initio calculations [51] indicate $0.02t \lesssim t' \lesssim 0.2t$ depending on the tight-binding parametrization. These calculations also include the effect of third-nearest-neighbors hopping, which has a hopping parameter of around 0.07 eV. A tight-binding fit to cyclotron resonance experiments [52] gives $t' \approx 0.1$ eV.

The two-dimensional energy dispersion relations of graphene can be calculated by solving the eigen-value problem for the Hamiltonian. In the Slater-Koster scheme [53] one gets

$$H = \begin{bmatrix} 0 & f(\mathbf{k}) \\ -f^*(\mathbf{k}) & 0 \end{bmatrix}, \tag{1.6}$$

where

$$f(\mathbf{k}) = -t \left(1 + e^{i\mathbf{k}\cdot\mathbf{a_1}} + e^{i\mathbf{k}\cdot\mathbf{a_2}}\right) = -t \left(1 + 2e^{\frac{i3k_x a}{2}} \cos\left(\frac{\sqrt{3}k_y a}{2}\right)\right). \tag{1.7}$$

Solution of the secular equation $\det(H - EI) = 0$ leads to the spectrum

$$E_\pm(\mathbf{k}) = \pm t \sqrt{1 + 4\cos\left(\frac{\sqrt{3}k_y a}{2}\right)\cos\left(\frac{3}{2}k_x a\right) + 4\cos^2\left(\frac{\sqrt{3}k_y a}{2}\right)}, \tag{1.8}$$

which is symmetric around zero energy. Here, $t' = 0$ was assumed.

Electrical conduction is determined by the states around the Fermi energy and so it is useful to develop an approximate relation that describes the linear dispersion relation around $E=0$. This can be done by replacing the expression for Eq. 1.7 with a Taylor expansion around one Dirac point $\mathbf{k} = \mathbf{K}$ where the energy gap is zero. To simplify the derivation, we define a new wave vector relative to $\mathbf{K}$ which is called $\mathbf{k}'$

$$\mathbf{k}' = \mathbf{k} - \mathbf{K} = (k_x - \frac{2\pi}{3a}, k_y - \frac{2\pi}{3\sqrt{3}a}), \tag{1.9}$$

so we have

$$f(\mathbf{k}') = -t \left(1 - 2e^{\frac{i3k_x' a}{2}} \cos\left(\frac{\sqrt{3}k_y' a}{2} + \frac{\pi}{3}\right)\right). \tag{1.10}$$

Now we consider the dispersion relation $E(k')$ which hols $E(0) = 0$. The Taylor expansion for new wave vector around $(0,0)$ gives

$$f \approx k_x' \left[\frac{\partial f}{\partial k_x'}\right]_{k'=0} + k_y' \left[\frac{\partial f}{\partial k_y'}\right]_{k'=0}. \tag{1.11}$$

It is straightforward to evaluate the partial derivatives

$$\left[\frac{\partial f}{\partial k_x'}\right]_{k'=0} = \frac{i3at}{2}, \qquad \left[\frac{\partial f}{\partial k_y'}\right]_{k'=0} = -\frac{3at}{2}, \tag{1.12}$$

therefore

$$f(\mathbf{k}') \approx \frac{i3at}{2}(k_x' + ik_y'). \tag{1.13}$$

The corresponding energy dispersion relation (Eq. 1.8) shows a linear dependence on the relation wavenumber $|k'| = \sqrt{k_x'^2 + k_y'^2}$

$$E(\mathbf{k}') = \pm|f(\mathbf{k}')| = \pm\frac{3at}{2}|\mathbf{k}'| \tag{1.14}$$
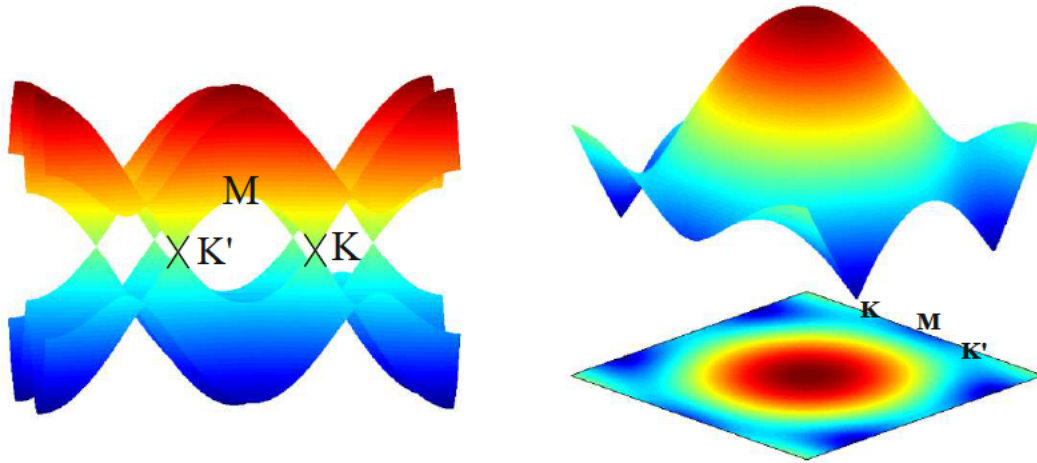
Figure 1.5.: The energy dispersion relations for graphene are shown through the whole region of the Brillouin zone. The lower and the upper surfaces denote the valence π and the conduction π^* energy bands, respectively. The coordinates of high symmetry points are $\Gamma = (0,0)$, $K = (2\pi/3a, 2\pi/3\sqrt{3}a)$, and $M = (2\pi/3a, 0)$. The energy values at the K, M, and Γ points are 0, t, and $3t$, respectively.

Figure 1.5 shows the electronic energy dispersion relations for graphene as a function of the two-dimensional wave-vector $\mathbf{k}$ in the hexagonal Brillouin zone. For finite values of t', the electron-hole symmetry is broken and the π and π^* bands become asymmetric.

The points K and K', which specify six locations in momentum space, are called Dirac points, see Fig. 1.5. The conduction and valence bands meet at the Dirac points so graphene is a zero-gap material. The term "massless Dirac fermions" is used to refer to linear dispersion relation $E_\pm(\mathbf{k})$ in Eq. 1.14. Electrons propagating through graphene behave as massless Dirac fermions because of the linear relation between their energy and their momentum [54].

1.1.2. Optical Properties

Graphene has interesting properties which allow multiple functions of signal emitting, transmitting, modulating, and detection to be realized in one material. Graphene shows superior properties compared to silicon and III-V semiconductors in terms of its high thermal conductivity ($\sim$ 36 times higher than Si and $\sim$ 100 times higher than GaAs), high optical damage threshold [55] (a few orders of magnitude higher than Si [56] and GaAs [57]), and high third-order optical nonlinearities ($\sim 3.3 \times 10^{-16}$ coulomb) [58, 59].

Due to the unique electronic structure in which conical-shaped conduction and valence bands meet at the Dirac point (Fig. 1.5), the optical conductance of pristine monolayer

graphene is frequency-independent in a broad range of photon energies [60]. It is argued [61,62] that the high-frequency (dynamic) conductivity G for Dirac fermions [63] in graphene should be a universal constant equal to [64]

$$G_l(\omega) = G_0 \equiv e^2/4\hbar, \qquad (1.15)$$

where index "l" refers to the real part, ω is the radian frequency, e is electron charge, and $\hbar$ is reduced Planck's constant. As a direct consequence of this universal optical conductance, the optical transmittance of pristine graphene is also frequency-independent and solely determined by the fine structure constant $\alpha = (1/4\pi\epsilon_0)(e^2/\hbar c)$, where c is the speed of light, $\epsilon_0 = 1/\mu_0 c^2$ is the permitivity of vacuum, and μ_0 is the permeability of vacuum. In the International System of Units (SI), c, ϵ_0, and μ_0 are exactly known constants. The optical transmittance of pristine graphene is defined as [65]

$$T = \left(1 + \frac{\pi\alpha}{2}\right)^{-2} \approx 1 - \pi\alpha \approx 0.977. \qquad (1.16)$$

When scaled to its atomic thickness, graphene actually shows strong broadband absorption per unit mass of the material ($\pi\alpha = 2.3\%$), which is ~ 50 times higher than GaAs of the same thickness [60,64,66]. The reflectance under normal light incidence is relatively weak and written as $R = 0.25\pi^2\alpha^2 T = 1.3 \times 10^{-4}$, which is much smaller than the transmittance [60]. The absorption of few-layer graphene can be roughly estimated by scaling with the number of layers ($T \cong 1 - N\pi\alpha$). In principle, a low sheet resistance can be attained without sacrificing the properties of transparency too much (i.e., tens of $\Omega/\square$ for $T > 90\%$). As such, it is believed that few-layer graphene can potentially replace ITO (indium tin oxide) as transparent conductors for applications in solar cells [67–69] and touch screens [70–72] in cases when it is sufficiently doped [65].

Based on the exciting optical properties of graphene, many graphene-based photonic and optoelectronic applications have been developed [70,73,74]. In this thesis we study the application of graphene-based structures as photodetectors (Fig. 1.6). Photodetectors measure the photon flux or optical power by converting the absorbed photon energy into electrical current [70]. They are used in various common devices in both science and technology [75], such as remote controls, televisions and DVD players. Modern light detectors are usually made using III-V semiconductors, such as gallium arsenide. When light strikes these materials, each absorbed photon creates an electron-hole pair (internal photoeffect). These pairs then separate and produce an electrical current. The spectral bandwidth is typically limited by the material's absorption [75]. For example, photodetectors based on group IV and III-V semiconductors suffer from the 'long-wavelength limit', as these become transparent when the incident energy is smaller than the bandgap [75]. A wide photon energy absorption range from the ultraviolet to terahertz could be covered by graphene-based photodetectors [60,76–78]. The response time is ruled by the carrier mobility [75] which is huge in graphene and thus ultrafast photodetectors are feasible [70].
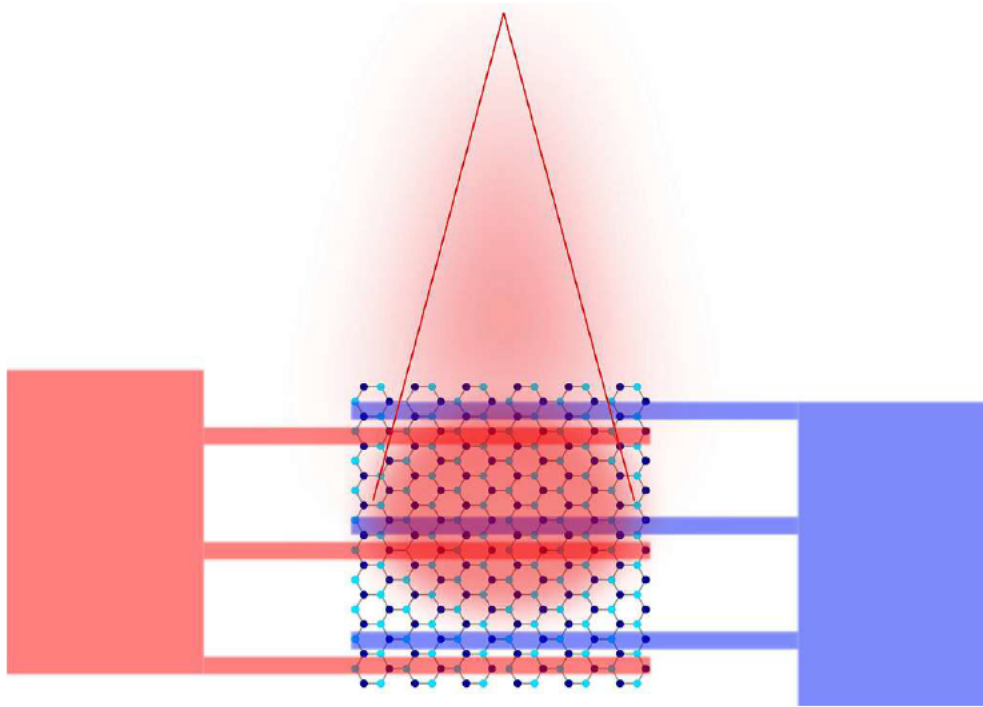
Figure 1.6.: Schematic of a graphene photodetector.

The photoelectrical response of graphene has been widely investigated both experimentally and theoretically [48, 79–82]. A photoresponse up to 40 GHz is reported for graphene photodetectors in [82]. The operating bandwidth is mainly limited by the time constant resulting from the device resistance and capacitance. Xia et al. reported an RC-limited bandwidth of about 640 GHz [82], which is comparable to traditional photodetectors [83]. However, the maximum possible operating bandwidth of photodetectors is typically restricted by their transit time [75].

The first application of graphene as a photodetector has been demonstrated in [84]. A detectable current has been reported that is attributed to the band bending at the metal/graphene interface [85]. Photocurrents have also been obtained at single/bilayer graphene interfaces [86] and graphene p-n junctions [87]. More recent studies concentrate on increasing the photoresponsivity of the graphene devices [88] and extending their operation range to longer wavelengths [89]. Recent photocurrent generation experiments in graphene show a strong photoresponse near metal/graphene interfaces, with an internal quantum efficiency of 15-30% despite its gapless nature [80, 81, 84]. Moreover, graphene photodetectors can potentially operate at speeds > 500GHz [82].

Although an external electric field can efficiently generate photocurrent with an electron-hole separation efficiency of over 30% [80], zero source-drain bias and dark current operations could be achieved by using the internal electric field formed near the metal

electrode-graphene interfaces [48,82]. However, the small effective area of the internal electric field could decrease the detection efficiency [48,82], as most of the generated electron-hole pairs would be out of the electric field region, thus recombining, rather than being separated. The internal photocurrent efficiencies (15-30%; Refs [80,82]) and external responsivity (generated electric current for a given input optical power) of ~ 6.1 mA per Watt reported so far [48] are relatively low compared with current photodetectors [75]. This is mainly due to limited optical absorption when only one single layer graphene is used, short photocarrier lifetimes and small effective photodetection areas (~ 200 nm in [82]).

1.2. Quantum Cascade Structures

Before the invention of diode lasers, a semiconductor laser based on transitions between Landau levels in a strong magnetic field was proposed by Lax in 1960 [90]. This is the first proposal of a semiconductor laser in which the optical transition occurs between low dimensional states of the same band (conduction or valence) rather than by the recombination of electron-hole pairs across the semiconductor bandgap [91]. The idea of a unipolar laser was then ignored for many years because only 2 years after the proposal of Lax the first diode laser was demonstrated [92]. This exploit drew all the attention of the semiconductor community on bandgap lasers and began the race for the first diode laser continuous-wave (cw) operation at room temperature. The race ended in 1970 when this goal was reached by the first AlGaAs/GaAs heterostructure laser at nearly the same time by Alferov's group at the Ioffe Institute in St. Petersburg [93] and by Panish et al. [94] at Bell Labs (Murray Hill, NJ).

The effort to improve the performance of diode lasers and the development of the transistor technology in III-V compounds had an enormous impact on the epitaxial growth techniques of thin semiconductor layers and gave rise to the concept of two-dimensional structures such as quantum wells (QWs) and inversion layers [95]. The confinement of carriers in semiconductor quantum wells and superlattices leads to formation of energy levels and subbands. Figure 1.7 shows the conduction band of a quantum well which splits into subbands.

In 1970, Esaki and Tsu [96] proposed the use of heterostructures for applications in optoelectronics. Kazarinov and Suris [97] were the first to propose intersubband transitions to design a laser. The quantum cascade laser (QCL) is a special kind of semiconductor laser, usually emitting mid-infrared light. Such a laser operates on laser transitions not between different electronic bands, but instead on intersubband transitions of a semiconductor structure. The first QCL was demonstrated by Federico Capasso in 1994 at Bell Labs for a wavelength of 4.2 μm, [98] and in 2001 Alessandro Tredicucci developed the first MIR QCL, operating at 68 μm [99]. QCLs have since then achieved significant performance improvements and are poised to become the dominant laser sources in the mid- and far-infrared spectral ranges. Lasing has been
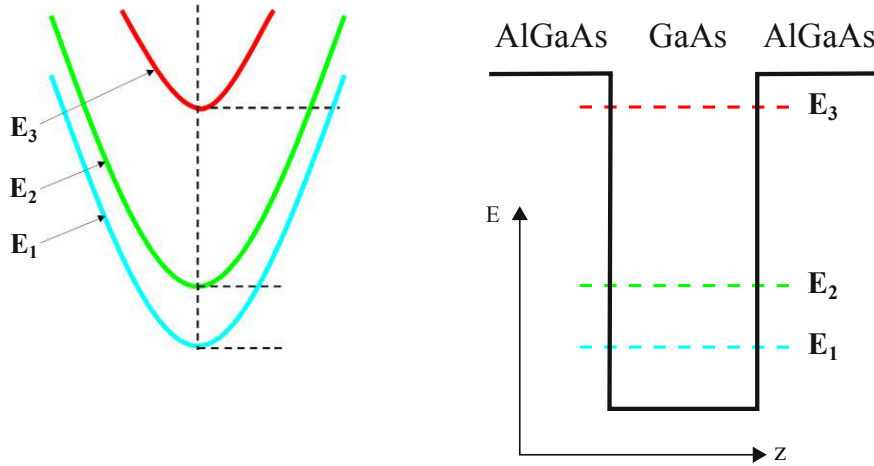
Figure 1.7.: Subbands in a quantum well. The potential well caused by the Al-GaAs/GaAs layer structure gives rise to bound states localized in the well. In k-space, there exist continuous subbands as the electrons are not confined in the plane of the well.

obtained at wavelengths ranging from 3.4-24 μm [98, 100] in the mid-infrared and 60-161 μm in the far-infrared [101].

The general principles of QCL operation are illustrated in Fig. 1.8. Shown are two active regions, i.e. the quantum well and barrier regions that support the electronic states between which the laser transition is taking place, and schematically the intermediate injector region. We draw the conduction band edge of the InGaAs QWs and the AlInAs barriers using the 520 meV low-temperature conduction band-offset usually associated with the materials' compositions (In$_{0.53}$Ga$_{0.47}$As, Al$_{0.48}$In$_{0.52}$As) lattice matched to the InP substrate. An external electric field is applied as visualized by the linear slope of the electronic potential. Solving the Schrödinger equation results in the energy levels drawn and the moduli squared of the wave functions. The wave functions and energy levels of each stage are shown. The lasing subbands are indicated with bold solid/bold dashed lines.

The QW thicknesses in the active region are selected such that the energy separation between level 3 and 2 corresponds to the desired wavelength. The energy separation between level 2 and 1 is deliberately chosen to be very close to the energy of the LO-phonon modes of the InGaAs/AlInAs/active region materials. Under an appropriate applied bias, electrons tunnel from the injector region into energy level 3, the upper laser state, of the active region. Electrons scatter from this level into both lower-lying levels 2 and 1, very rapidly emitting LO-phonons. The scattering time between levels 2, the lower laser state, and level 1 is ultra-short due to the resonant nature of this transition with the LO-phonon. Therefore, population inversion occurs between the laser levels 3 and 2 and laser action is possible. Electrons need only be supplied fast
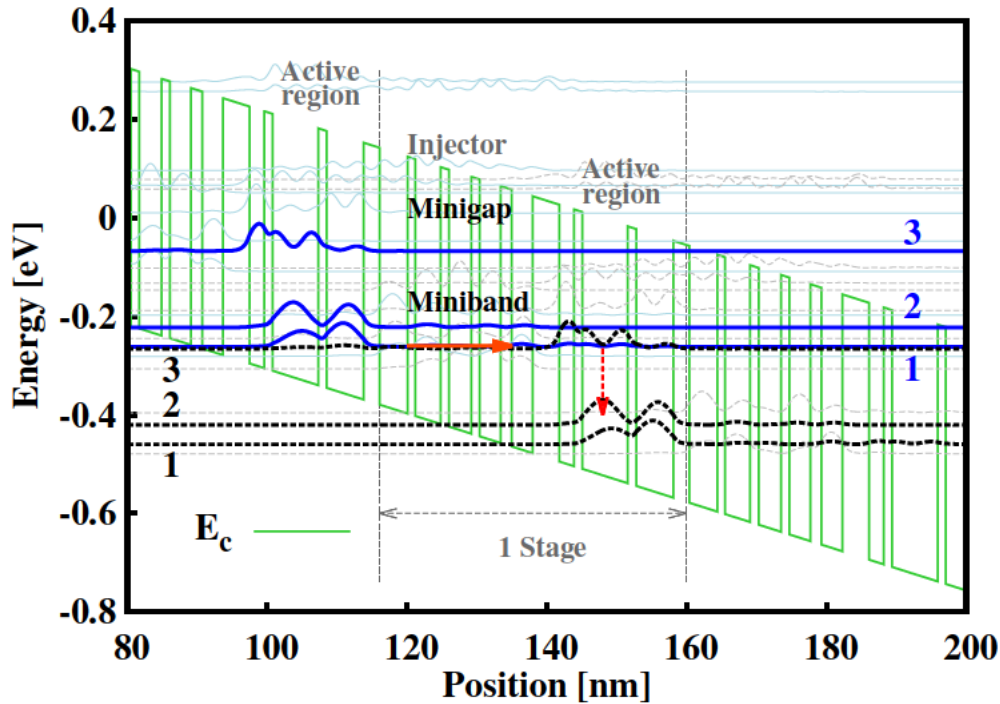
Figure 1.8.: Schematic conduction band energy diagram of two QCL active regions with the intermediate injector region and the moduli squared of the wave functions involved in the laser transition (labelled 1, 2, and 3). The laser transition is indicated by the vertical arrow, the electron flow by the horizontal arrow.

enough into level 3 by tunneling from the preceding injector region, and need to exit from levels 2 and more so from level 1 into the following downstream injector region at a high rate by tunneling. Inside the injector region and brought about by the externally applied electric field, electrons gain again in energy (relative to the band bottom) and are injected into the following downstream active region.

Typical QCLs have a cascade containing 20 to 30 active regions alternated with injector regions, although laser action has been achieved for a single active region [102], and has been tested for as many as 100 active regions [103]. A key feature of QCLs is the ability to cascade N modules together, so that a single injected electron can emit many photons, which allows for a differential quantum efficiency greater than unity.

In QCLs, three aspects mainly influence laser performance. First of all, optimization of the active region design, in order to ensure efficient carrier injection in the upper lasing state and carrier extraction out of the lower lasing state. Second, epitaxial growth optimization and third, optimization of the fabrication process, which is crucial to reduce optical losses and improve the laser thermal conductance [104]. Concerning the optimization of the laser design, many schemes have been proposed [105–107],

13

however, a systematic study of the laser design was never permitted due to the large number of variables involved [104].

Since their inception in 1994 many designs of QCLs have emerged, and can basically be characterized by their number of QWs in the active region and the spatial extent and number of the wave functions in the active regions [108]. Three high-performance structures are introduced in the following.

1.2.1. Three-Well Vertical Design

The structure discussed in the last section (Fig. 1.8) is called a three-well (3QW) vertical-transition QCL in which a thin well is inserted between the injector region and an active region (which could also be termed a two-well vertical-transition active region). The additional QW leads to a significant reduction of electron scattering (leakage) from the injector directly into the laser ground state 2 and also level 1 [108]. The improvement led to the first high-performance, room temperature operation of QCLs [109]. This laser design, emitting at $8\mu m$ wavelength, provides high optical gain and concomitant robust laser action [110].

The active region, shown in Fig. 1.8, consists of three InGaAs QWs closely coupled by thin InAlAs barriers. At the appropriate electric field, corresponding to the measured laser threshold, the upper laser level (level 3) is separated from the lower laser level (level 2). The lower laser level is closely coupled to the ground state (level 1) of the active region, such that the two levels are strongly anti-crossed. This increases the matrix element z_{32} with respect to z_{31} and maximizes the scattering time between levels 3 and 2 with respect to the scattering time between levels 3 and 1. The energy difference between levels 2 and 1, designed to efficiently deplete the lower laser level of electrons via resonant LO-phonon scattering.

The injector 'miniband' — more accurately, the manifold of energy levels in the injector — has been designed to be 'flat'. Its ground level is located below the upper laser level. Even the next-higher level of the injector miniband is energetically lower than the upper laser level. The injector has been doped in the center part. Therefore, at laser threshold, electrons are not injected from the Fermi-surface into the upper laser level. Furthermore level 1 of the preceding active region is in resonance with level 3 of the following active region, allowing for resonant carrier transport between successive active regions without significant carrier relaxation in the injector. In comparison, the relaxation time within the injector is long since the energy separation to the adjacent lower energy level is well below the LO-phonon energy and the ground level of the injector region is partly filled with electrons.

The 3QW vertical-transition design has this advantage that it avoids a too early 'shut-down' of the laser due to suppression of resonant tunneling [111]. Once the electric field increases and the resonance between levels 1 and 3 is destroyed, there is still strong injection from the ground state of the injector, allowing for a wide dynamic range
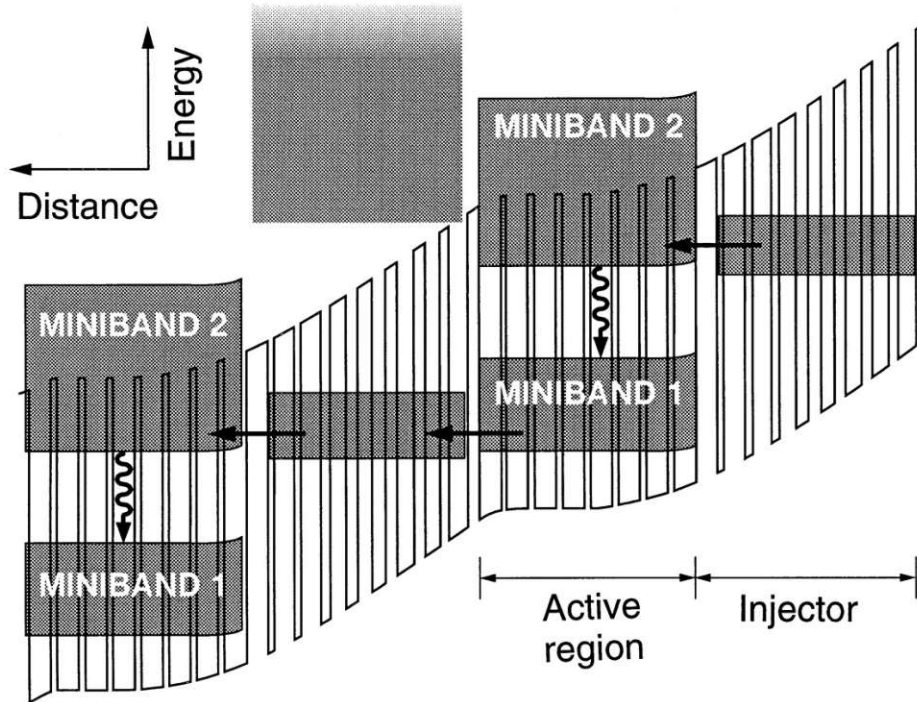
Figure 1.9.: Conduction-band structure of the original SL-QCL. Two active region SLs with the preceding injector regions are shown. The minibands are indicated by gray regions. Laser action, as denoted by the wavy arrows, takes place across the first minigap 2-1. Adapted from [112].

of current and concomitant high optical power [108]. The 3QW vertical-transition design is employed in the performance optimization and instability study presented in Sec. 5.2.

1.2.2. Superlattice Design

A different design of QCLs, which was first introduced in 1997, is the superlattice (SL) active region [112]. In short, laser action takes place between minibands, rather than between the subbands of few and single [113] well active region QCLs. High optical gain, large current carrying capabilities, and weaker temperature sensitivity are the advantages of SL-QCLs. However, they can generally only be applied for the longer-wavelength range (i.e. $\lambda \geq 7\mu m$, for lattice-matched InP-based SL-QCLs) as the wider minibands take up more energy space than simple subbands [108].

In general, semiconductor SLs consist of a periodic stack of nanometer-thick layers of QWs and barriers. The period of this artificial crystal is typically much larger than the lattice constant of the bulk crystalline constituents. This superimposed periodic crystal potential splits the conduction band (and the valence bands as well) along the

direction normal to the layers into a series of narrow (typically, tens to a few hundreds of meV wide) minibands separated by energy gaps ('minigaps') in the strong-tunnel-coupling regime. For a given set of materials, miniband and minigap widths can be engineered by suitable choice of the layer thicknesses. In the generic case of the simple periodic SL, however, those widths are not independent of each other [108].

Figure 1.9 illustrates the original interminiband SL-QCL concept and its first realization [112]. Electrons are injected electrically from a preceding, equally doped, injector region directly into the ground state near the bottom of the second 'upper' miniband, as was the case with the simple three-well active region discussed previously. From there, electrons can make an optical transition to the top of the lower miniband. In k-space, this transition occurs at the boundary of the mini-Brillouin-zone.

In QCLs, the inter-miniband scattering processes are generally dominated by LO-phonon emission. Specifically, an electron thermalized near the bottom of the higher miniband can relax down to states near the top of the lower miniband by scattering via LO-phonon emission employing a high momentum transfer. This process is characterized by a comparatively long scattering time of ~ 10 ps. Within each miniband, the electrons relax much faster — in a few tenths of a picosecond — by intra-miniband scattering, because it involves the emission of small-wavevector optical phonons. The resulting large ratio of relaxation times of inter- versus intra-miniband scattering events ensures an intrinsic population inversion across the minigap [108].

A second unique design feature of the SL-QCL is the high oscillator strength for the optical transition at the mini-Brillouin zone boundary of the SL. The oscillator strength of radiative transitions between the first two minibands of a SL increases with wavevector and is maximum at the zone boundary [114]. In particular, it strongly increases with decreasing barrier thickness. In the original SL-QCL structure shown in Fig. 1.9, the wavelength was selected as 8 μm, using an eight-period SL with 1 nm thick AlInAs barriers and 4.3 nm thick InGaAs QWs in lattice-matched composition. The structure was optimized for maximum oscillator strength with an optical dipole matrix element of 3.6 nm, i.e. approximately twice as large as that of similar-wavelength QCLs featuring few-well active regions.

1.2.3. Diagonal Transition Design

The third type of active region we discuss here is called 'diagonal' transitions active region in which the upper and lower state wave functions are clearly located in spatially different regions. The 3QW and SL-QCLs designs described in the previous two sections had in common that the wavefunctions directly involved in laser action, i.e. the upper and lower laser state, are essentially located in the same region of real space.

The two wave functions being collocated has several distinctive consequences. First, from an energy level point of view, the energy separation of the two states is largely

independent of the applied electric field in a fairly wide range around the design field. This gives lasers based on such a vertical design a clear robustness in terms of wavelength versus applied voltage and, as a consequence, also versus temperature. On the other hand, and relating to the calculation of the gain coefficient, the collocation of the wave functions leads to a comparatively large optical dipole matrix element, but also comparatively short electron scattering times. Both are a result of the large overlap of the wave functions of upper and lower laser states [108].

In contrast to 3QW vertical transitions, QCLs based on such active regions show a strong dependence of the wavelength on the applied electric field through a voltage-induced Stark effect. The design parameters are furthermore characterized through a smaller dipole matrix element but also clearly longer scattering times, thus allowing again for sufficient gain to achieve laser action [108]. These lasers can operate up to room temperature and are exploited for large wavelength tunability [115]. This particular design can be used to fabricate QCLs that operate under both bias polarities and with nearly independent attributes, such as two different wavelengths [116] depending on bias polarity.

1.2.4. Short Pulse Generation

Ultrashort pulses with large instantaneous intensities from mode-locked lasers are key elements for many important applications such as time-resolved measurements [117, 118], optical parametric generation [119], coherent control [120], four-wave mixing [121], and frequency combs [122].

The word mode-locking describes the locking of multiple axial modes in a laser cavity. By enforcing coherence between the phases of different modes, pulsed radiation can be produced. Mode-locking is a resonant phenomenon. By a relatively weak modulation synchronous with the roundtrip time of radiation circulating in the laser, a pulse is initiated and can be made shorter on every pass through the resonator. The shortening process continues unabated, until the pulse becomes so short and its spectrum so wide that pulse lengthening mechanisms or spectrum narrowing processes spring into action, such as finite bandwidth of the gain. The history of laser mode-locking is a progression of new and better ways to generate shorter and shorter pulses, and of improvements in the understanding of the mode-locking process.

To date, the most common approach to generate short pulses in the mid-infrared molecular "fingerprint" region relies on the down-conversion of short-wavelength mode-locked lasers through nonlinear processes. These systems are usually bulky, expensive and typically require a complicated optical arrangement [123]. Design degrees of freedom in QCLs such as emission wavelength, gain spectrum [124], carrier transport characteristics, and optical dispersion make the QCL a unique candidate to serve as a semiconductor source of ultra-short pulses at MIR and THz domains. There is, however, an obstacle of fundamental origin that has so far prevented achieving ultrashort

pulse generation in QCLs [125,126]. In intersubband transitions, the carrier relaxation is extremely fast because of optical phonon scattering. As a result, the gain recovery time in QCLs, determined both by upper state lifetime and by the electron transport through the cascade heterostructure, is typically on the order of a few picoseconds [127] which is an order of magnitude smaller than the cavity roundtrip time of 40-60 ps for a typical 2-3 mm-long laser cavity [123]. According to conventional mode-locking theory, this situation prevents the occurrence of stable passive mode-locking. However, under these conditions the elusive Risken-Nummedal-Graham-Haken (RNGH)-like instability can be possible in QCLs [125].

A saturable absorber is an optical component with a certain optical loss, which is reduced at high optical intensities. This can occur, e.g., in a medium with absorbing dopant ions, when a strong optical intensity leads to depletion of the ground state of these ions. Similar effects can occur in semiconductors, where excitation of electrons from the valence band into the conduction band reduces the absorption for photon energies just above the bandgap energy. The main applications of saturable absorbers are passive mode locking and Q switching of lasers, i.e., the generation of short pulses. However, saturable absorbers are also useful for purposes of nonlinear filtering outside laser resonators, e.g. for cleaning up pulse shapes, and in optical signal processing. In lasers with a relatively long gain recovery time compared to the cavity round-trip time, the instability caused by a saturable absorber (SA) can often lead to passive mode locking [128].

We investigate the passive mode locking with saturable absorber in QCLs operating at MIR and THz. The effects of saturable absorber and pumping strength on the instability characteristics are studied. A numerical calculation based on the Maxwell-Bloch equations is performed to analyze the dynamics of QCLs, see Sec. 5.3.

1.3. Outline of This Work

In this work, we analyze the optical properties of semiconductor nanostructures and their application in photodetectors and lasers. Graphene with various geometrical structures embedded in boron-nitride lattices is studied as a new material. Quantum cascade lasers and detectors are studied in this thesis.

Chapter 2 investigates the optical properties of armchair graphene nanoribbons (AG-NRs) and graphene nanoribbons embedded in boron nitride (BN) lattices. The first principle calculations, the tight-binding model, and the non-equilibrium Green's function formalism employed in this study are presented in Sec. 2.1. In Sec. 2.2, the optical matrix elements and transition rules are discussed. Dielectric response, quantum efficiency, and photoresponsivity of AGNRs/BN are discussed in Sec. 2.3. Finally, Sec. 2.4 provides concluding remarks for this chapter.

18

Chapter 3 describes the analytical approach to approximate the wave functions and energy dispersion in zigzag graphene nanoribbons (ZGNRs). The electronic structure of ZGNRs is derived analytically in Sec. 3.1. The wavenumber approximations to reach analytical models for the dispersion relation and the wave function are derived in Sec. 3.2. In Sec. 3.3, optical matrix elements and transition rules of ZGNRs are obtained from the model. The two approximations used in our models and the derived optical properties are discussed in Sec. 3.4. Finally, Sec. 3.5 draws concluding remarks for this chapter.

In chapter 4, graphene superlattice-based photodetectors are discussed. The optical properties of one dimensional superlattices formed by AGNRs embedded in BN superlattices are presented in Sec. 4.1. The line-edge roughness model is described in Sec. 4.2. This chapter is concluded in Sec. 4.3.

In Chapter 5, the application of quantum cascade structures for the MIR and terahertz region is discussed. An optimization and dynamics study of quantum cascade lasers (QCLs) is presented. Section. 5.1 describes the transport and optimization models. In Sec. 5.2, the simulation results for performance optimization are presented and discussed. Dynamics of QCLs is studied in Sec. 5.3. Quantum cascade detectors are presented in Sec. 5.4.

Chapter 6 finally summarizes the thesis with conclusions.

2. Optical Properties of Armchair Graphene Nanoribbons

Armchair graphene nanoribbons (AGNRs) have recently attracted much interest as they are recognized as promising building blocks for nanoelectronic devices [38]. AGNRs, a type of graphene nanoribbons (GNRs) with armchair edges, introduce a tunable band-gap which is suitable for electrical and optical applications [70].

Single-layer hexagonal boron nitride (h-BN) and boron nitride nanoribbons (BNNRs), which are regarded as the III-V analogs of graphene and GNRs, respectively, have been synthesized and studied in recent years [129–132]. Theoretical and experimental results have shown that the sp^2 bonding in the BN lattice gains an ionic character due to different electronegativity of B and N, that causes the optical and electronic properties of BN and BNNRs to be substantially different from that of graphene and GNRs [131]. Unlike graphene, which is a zero-gap material, h-BN has a wide bandgap of approximately 5.9eV and shows good insulating behavior [133].

BNNRs are expected to be produced using a single-layer h-BN as the starting material [131]. The similarity of the crystal structures of BN and graphene gives rise to thermodynamically stable two-dimensional structures containing isolated regions of graphene and BN [132, 134]. It has been shown that AGNRs embedded in BN sheets (AGNRs/BN) are semiconductors [132]. Due to the relatively large ionicities of boron and nitrogen, BN-confined AGNRs exhibit a generally larger bandgap compared to H-passivated AGNRs [135, 136]. These hybrid C-BN structures can be synthesized by approaches such as thermal catalytic CVD methods [134].

A relatively large bandgap of graphene nanoribbons incorporated in a BN lattice renders them as suitable candidates for opto-electronic applications. Structures composed of GNRs and BNNRs introduce more flexibility for electronic and opto-electronic applications. In this chapter, we investigate for the first time a theoretical study of the optical properties of graphene and graphene/BN nanoribbons.

2.1. Models

2.1.1. First Principle Calculations

Density functional theory (DFT) is a quantum-mechanical method used in chemistry and physics to calculate the electronic structure of many-body systems, in particular atoms, molecules, and the condensed phases [137, 138]. With this theory, the properties of a many-electron system can be determined by using functionals, i.e. functions of another function, which in this case is the spatially dependent electron density. Hence the name density functional theory comes from the use of functionals of the electron density [139]. DFT is among the most popular and versatile methods available in condensed-matter physics, computational physics, and computational chemistry [140].

DFT has been very popular for calculations in solid-state physics since the 1970s [138]. However, DFT was not considered accurate enough for calculations in quantum chemistry until the 1990s, when the approximations used in the theory were greatly refined to better model the exchange and correlation interactions. In many cases the results of DFT calculations for solid-state systems agree quite satisfactorily with experimental data [141, 142]. Computational costs are relatively low when compared to traditional methods, such as Hartree-Fock theory and its descendants based on the complex many-electron wave function.

The major problem with DFT is that the exact functionals for exchange and correlation are not known except for the free electron gas. However, approximations exist which permit the calculation of certain physical quantities quite accurately [141]. An approximation to the exchange-correlation term is used. It is called the local density approximation (LDA). For any small region, the exchange-correlation energy is the approximated by that for jellium of the same electron density. In other words, the exchange-correlation hole that is modelled is not the exact one — it is replaced by the hole taken from an electron gas whose density is the same as the local density around the electron [143].

In physics, LDA is the most widely used approximation, where the functional depends only on the density at the coordinate where the functional is evaluated [144]

$$E_{\mathrm{XC}}^{\mathrm{LDA}}[n] = \int \epsilon_{\mathrm{XC}}(n) n(\vec{r}) \mathrm{d}^3 r. \tag{2.1}$$

The local spin-density approximation (LSDA) is a straightforward generalization of the LDA to include electron spin:

$$E_{\mathrm{XC}}^{\mathrm{LSDA}}[n_\uparrow, n_\downarrow] = \int \epsilon_{\mathrm{XC}}(n_\uparrow, n_\downarrow) n(\vec{r}) \mathrm{d}^3 r. \tag{2.2}$$

Highly accurate formula for the exchange-correlation energy density $\epsilon_{\text{XC}}(n_\uparrow, n_\downarrow)$ have been constructed from quantum Monte Carlo simulations of Jellium [145]. Jellium, also known as the uniform electron gas or homogeneous electron gas, is a quantum mechanical model of interacting electrons in a solid where the positive charges (i.e. atomic nuclei) are assumed to be uniformly distributed in space whence the electron density is a uniform quantity as well in space [146].

The interesting point about this approximation is that although the exchange-correlation hole may not be represented well in terms of its shape, the overall effective charge is modelled exactly [146]. This means that the attractive potential which the electron feels at its centre is well described. Not only does the LDA approximation work for materials with slowly varying or homogeneous electron densities but in practise demonstrates surprisingly accurate results for a wide range of ionic, covalent and metallic materials [146].

An alternative, slightly more sophisticated approximation is the generalised gradient approximation (GGA) [147–149] which estimate the contribution of each volume element to the exchange-correlation based upon the magnitude and gradient of the electron density within that element. GGA are still local but also take into account the gradient of the density at the same coordinate:

$$E_{XC}^{\text{GGA}}[n_\uparrow, n_\downarrow] = \int \epsilon_{XC}(n_\uparrow, n_\downarrow, \vec{\nabla} n_\uparrow, \vec{\nabla} n_\downarrow) n(\vec{r}) \mathrm{d}^3 r. \tag{2.3}$$

Using GGA very good results for molecular geometries and ground-state energies have been achieved.

In this work, the imaginary part of the dielectric function is calculated by DFT to investigate the optical properties of studied structures [150]. If the incident light is assumed to be polarized along the transport direction (x-axis), the imaginary part of the dielectric function in the linear response regime is given by [150]

$$\varepsilon_{\text{i}}(\omega) = \frac{1}{4\pi\varepsilon_0} \left(\frac{2\pi\mathrm{e}}{m\omega}\right)^2 \sum_{\mathbf{k_x}} |p_{c,v}|^2 \delta(E_c(k_x) - E_v(k_x) - \hbar\omega)$$
$$\times \left[f(E_v(k_x)) - f(E_c(k_x)) \right], \tag{2.4}$$

where $\hbar\omega$ is the energy of the incident photons and $p_{c,v}$ are the momentum matrix elements for optical transitions. The Dirac delta is approximated by a Gaussian function with a broadening factor of 0.1 eV.

The summation in Eq. 2.4 can be converted into an energy integration by introducing the joint density of states (JDOS) defined as

$$D_j(\hbar\omega) = \frac{1}{\pi} \int_{S_{k_x}} \frac{dS}{|\nabla_{k_x}(E_c(k_x) - E_v(k_x))|}, \tag{2.5}$$

where S_{k_x} is the constant energy surface defined by $E_c(k_x) - E_v(k_x) = \hbar\omega$.

The real part of the dielectric function $\varepsilon_r(\omega)$ can be evaluated from the imaginary part using the Kramers-Kronig relation [150]. The interband dielectric function is related to the optical conductivity by $\varepsilon(\omega) = 1 + 4\pi i\sigma(\omega)/\omega$ [151].

For DFT calculations, we employed the Spanish Initiative for Electronic Simulations with Thousands of Atoms (SIESTA) package [152] with the following parameters: double-ζ basis set with additional orbitals of polarization for total energies and electronic band-structures calculations, the generalized gradient approximation method, Perdew-Burke-Ernzerhof (PBE) as the exchange-correlation function, and the Troullier-Martins scheme for the norm-conserving pseudopotential calculations [135]. A grid cutoff of 210 Ry is used and the Brillouin zone sampling is performed by the Monkhost pack mesh of k-points. A mesh of $(128 \times 8 \times 1)$ has been adopted for discretization of k-points and a broadening factor of 0.1eV is assumed for the joint density of states calculation, and the convergence criterion for the density matrix is taken as 10^{-4}.

2.1.2. Tight-Binding Model

In graphene three σ bonds hybridize in an sp^2 configuration, whereas the other $2p_z$ orbital, which is perpendicular to the graphene layer, forms π covalent bonds. Each atom in an sp^2-coordination has three nearest neighbors, located $a_{cc} = 1.42$ Å away, see Fig. 2.1. It is well known that the electronic and optical properties of GNRs are mainly determined by the π electrons [153]. To model these π electrons, a nearest neighbor tight-binding approximation has been widely used [51, 154]. Based on this approximation the Hamiltonian can be written as:

$$H = t \sum_{\langle p,q \rangle} (|A_p\rangle\langle B_q| + |B_q\rangle\langle A_p|), \qquad (2.6)$$

$|A_p\rangle$ and $|B_q\rangle$ are atomic wave functions of the $2p_z$ orbitals centered at lattice sites and are labeled as A_p and B_q, respectively, $\langle p,q \rangle$ represent pairs of nearest neighbor sites p and q, $t = \langle A_p|H|B_q\rangle \approx -2.7$eV is the transfer integral, and the on-site potential is assumed to be zero.

To study AGNR/BN, however, a TB model incorporating at least two nearest neighbors is required [135]. Reference [135] has shown that the band structure of AGNRs/BN can be calculated within the desired precision assuming the orthogonality of atomic orbitals and considering the effect of more nearest neighbors for each atom. Reference [155] shows that taking the effect of the first three neighboring atoms into consideration results in a good agreement with first principles calculations. Also, considering the second nearest neighbor carbon atoms in TB calculations will shift the dispersion relation by a constant value, [155] thereby affecting the optical transition

23
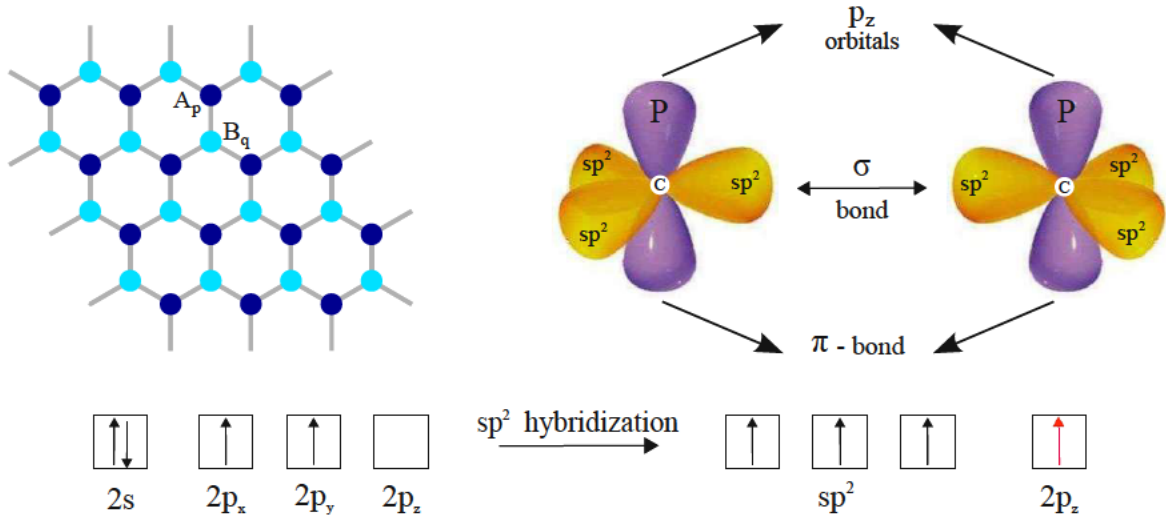
Figure 2.1.: Schematic view of the sp^2 hybridization. The orbitals form angles of $120°$.

rules. Therefore, up to second nearest neighbors are included in our work employing the parameters reported in Ref. [135].

To investigate the optical response of AGNRs/BN, the incident light is assumed to be polarized along the transport direction (x-axis). Particularly, it is shown that the photocurrent is maximized for photons polarized along the longitudinal direction of the structure, [156] which are the main source for interband transitions [151, 157, 158].

2.1.3. Non-Equilibrium Green's Function

Over the past decade the non-equilibrium Green's function formalism has been widely employed to investigate various nano electronic devices [159]. Four types of Green's functions are defined as the non-equilibrium statistical ensemble averages of the single particle correlation operator. The greater Green's function, $G^>$, and the lesser Green's function, $G^<$, deal with the statistics of carriers. The retarded Green's function, G^R, and the advanced Green's function, G^A, describe the dynamics of carriers. Under steady-state condition the equation of motion for the Green's functions can be written as [159]:

$$G^R(E) = \left[\left(E + i0^+ \right) I - H - \Sigma^R(E) \right]^{-1} \tag{2.7}$$

$$G^{\gtrless}(E) = G^R(E)\Sigma(E)^{\gtrless}G^A(E) \tag{2.8}$$

where H is the Hamiltonian matrix. In this formalism the effect of various interactions is included in the self-energy term:

$$\Sigma^R = \Sigma_1^R + \Sigma_2^R + \Sigma_s^R, \tag{2.9}$$

24

where Σ_1 and Σ_2 are the self-energies of the left/right contacts and Σ_s is the scattering self-energy. The self-energy due to electron-photon interaction is considered in this work. The Hamiltonian of the electron-photon interaction can be written as [160,161]:

$$\hat{H}_{\text{e-ph}} = \sum_{\langle i,j \rangle} \frac{\text{q}}{\text{m}_0} \hat{\mathbf{A}} \cdot \langle i|\hat{\mathbf{p}}|j \rangle \ , \tag{2.10}$$

where $\hat{\mathbf{p}}$ is the momentum operator and $\hat{\mathbf{A}}$ is the vector potential. In second quantization the vector potential is given by

$$\hat{\mathbf{A}} = \mathbf{a}\sqrt{\frac{\hbar I_\omega}{2N_\omega \omega \epsilon c}} \left(\hat{b}e^{-i\omega t} + \hat{b}^\dagger e^{+i\omega t} \right) \tag{2.11}$$

The direction of $\hat{\mathbf{A}}$ is determined by the polarization of the field, which is denoted by the unit vector $\mathbf{a}$.

As atomic orbitals in tight-binding are unknown, to evaluate the matrix elements of the momentum, it is common to use the gradient approximation [162] where the following commutator relation is used $\hat{\mathbf{p}} = (i\text{m}_0/\hbar)[\hat{H}, \hat{\mathbf{r}}]$.

Based on this approximation, for a transition from a state $|m\rangle$ to a final state $|l\rangle$, the momentum matrix elements ($p_{x_{l,m}} = \langle l|\hat{p}_x|m\rangle$) are

$$p_{x_{l,m}} = (i\text{m}_0/\hbar)\langle l|\hat{H}\hat{x} - \hat{x}\hat{H}|m\rangle. \tag{2.12}$$

The momentum matrix elements are therefore given by [163]

$$p_{x_{l,m}} = (x_m - x_l)\frac{i\text{m}_0}{\hbar}\langle l|\hat{H}|m\rangle. \tag{2.13}$$

Therefore, one can rewrite the electron-photon interaction Hamiltonian as:

$$\hat{H}_{\text{e-ph}} = \sum_{\langle l,m \rangle} M_{l,m} \left(\hat{b}e^{-i\omega t} + \hat{b}^\dagger e^{+i\omega t} \right) \hat{a}_l^\dagger \hat{a}_m \tag{2.14}$$

$$M_{l,m} = (x_m - x_l)\frac{ie}{\hbar} \left(\frac{\hbar\sqrt{\epsilon_r \mu_r}}{2N_\omega \omega \epsilon c}I_\omega \right)^{1/2} \langle l|\hat{H}_0|m\rangle \tag{2.15}$$

where x_m denotes the position of the carbon atom at site m and N_ω is the photon population number with the frequency ω.

The *photon flux* (I_ω), is defined as the number of photons per unit time per unit area [160,164]:

$$I_\omega \equiv \frac{N_\omega \text{c}}{\mathcal{V}\sqrt{\epsilon_\text{r} \mu_\text{r}}} = P_\text{op}/(\hbar\omega), \tag{2.16}$$

where ϵ_r and μ_r are the relative dielectric and magnetic susceptibility, $\mathcal{V}$ is the volume,

and P_{op} is the incident power flux. The incident light is assumed to be monochromatic with a power of $P_{\mathrm{op}} = 100\mathrm{kW/cm}^2$, and polarized along the longitudinal axis, see Fig. 4.1.

We employed the lowest order self-energy of the electron-photon interaction based on the self-consistent Born approximation [165]:

$$
\begin{aligned}
\Sigma_{l,m}^{<}(E) = \sum_{p,q} M_{l,p} M_{q,m} \\
\times \left[N_\omega G_{p,q}^{<}(E - \hbar\omega) + (N_\omega + 1) G_{p,q}^{<}(E + \hbar\omega) \right]
\end{aligned}
\tag{2.17}
$$

where the first term corresponds to the excitation of an electron by the absorption of a photon and the second term corresponds to the emission of a photon by de-excitation of an electron.

2.2. Optical Matrix Elements

The interband optical matrix element for a transition from an eigenstate in the valence subband to another eigenstate in the conduction subband is calculated in Sec. 2.1.3. These matrix elements determine the selection rules for optical transitions [166]. A zero matrix element means a forbidden transition. To determine a transition rule, it is sufficient to determine the symmetry of the transition matrix element. If the symmetry of this element spans the totally symmetric representation of the point group to which the unit cell belongs then its value is not zero and the transition is allowed. Otherwise, the transition is forbidden. Assuming a uniform potential profile across the ribbon's width, the subband's wave functions are either symmetric or anti-symmetric along the y-axis direction ($\psi_{c/v}(-y) = \pm\psi_{c/v}(y)$). Therefore, the momentum matrix elements are non-zero for interband-transitions from the symmetric (anti-symmetric) to the symmetric (anti-symmetric) wave functions. This transition rule results in transitions from subbands with odd (even) to odd (even) indices in AGNRs/BN, which is described later.

Figure. 2.2 shows the structure of an AGNR/BN represented by AGNRn_{cc}BNm_{bn}, where n_{cc} is the number of carbon dimers in the unit cell of the AGNR and $m_{bn} = m_{bnu} + m_{bnl}$ is the summation of the upper and lower BNNRs dimers.

The wave functions at the sublattices A and B of an AGNR$_{20}$BN$_{40}$ at $k_x = 0$ are shown in Fig. 2.3. $C_{A/B}$, $N_{A/B}$, and $B_{A/B}$ represent the components of the wave functions at a carbon, nitrogen, and boron atom at some sublattice A or B. The wave function of each subband is the summation of the wave functions at these two sublattices. For example, the wave functions for the subband indices $n_v = 60$ (Fig. 2.3(g) and (h)), $n_c = 2$ (Fig. 2.3(i) and (j)), and $n_c = 60$ (Fig. 2.3(a) and (b)) are anti-symmetric. Therefore, as discussed before, the matrix elements are non-zero for transitions from $n_v = 60$ to $n_c = 2$ and $n_c = 60$. The transitions from $n_v = 59$ to $n_c = 1$ and
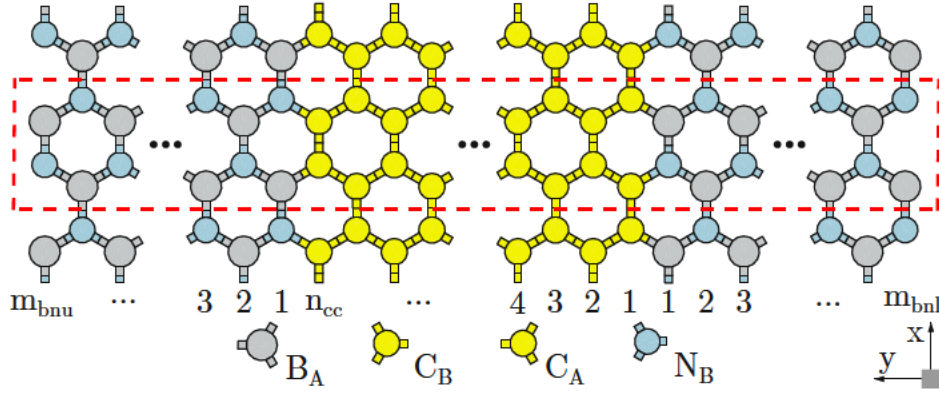
Figure 2.2.: The structure of an AGNRn_{cc}BNm_{bn}. The incident light is assumed to be polarized along the x-direction. $C_{A/B}, N_{A/B}$, and $B_{A/B}$ represent a carbon, a nitrogen, and a boron atom at the sublattice A or B.

$n_c = 59$ are also possible as their respective wave functions are symmetric. With the same analysis, a transition from the highest valence subband to the lowest conduction subband ($n_v = 1$ to $n_c = 1$) is possible in AGNRs/BN, see Fig. 2.3(m) and (n) and Fig. 2.3(k) and (l).

To obtain the transition rules, momentum matrix elements should be calculated. The total wave functions of the system is given by [167]

$$|\psi\rangle = C_A|\psi_A\rangle + C_B|\psi_B\rangle \ . \tag{2.18}$$

The Bloch wavefunctions $|\psi_A\rangle$ and $|\psi_B\rangle$ can be expressed as a linear combination of atomic wavefunctions of $2p_z$ orbitals $|A_p\rangle$ and $|B_q\rangle$. Due to translational invariance along the x direction one obtains

$$|\psi_A\rangle = \frac{1}{\sqrt{\Omega_A}} \sum_{p=1}^{N} e^{ik_x x_p^A} \phi_p |A_p\rangle \ , \qquad |\psi_B\rangle = \frac{1}{\sqrt{\Omega_B}} \sum_{p=1}^{N} e^{ik_x x_p^B} \phi_p |B_p\rangle \ , \tag{2.19}$$

where $\Omega_{A/B}$ are the normalization factors, N is the number of A and B sublattices in the unit-cell of the GNR, $x_p^{A/B}$ are the x-positions of the pth A/B-type carbon atom, ϕ_p is the y direction component of the wavefunctions at the pth lattice site. We impose hard-wall boundary conditions [168] at the edges, $\phi_0 = 0$ and $\phi_{N+1} = 0$. Therefore, one can assume that the component of the wavefunctions in the y direction form standing waves

$$\phi_p = \sin\left(\frac{\pi n}{N+1}p\right) = \sin(n\theta p), \qquad n = 1, 2, \ldots, N. \tag{2.20}$$

where n is the band index. For convenience the notation $\theta = \pi/(N+1)$ is introduced. Assuming the normalization condition $\langle\psi_A|\psi_A\rangle = \langle\psi_B|\psi_B\rangle = 1$, [168] the prefactors
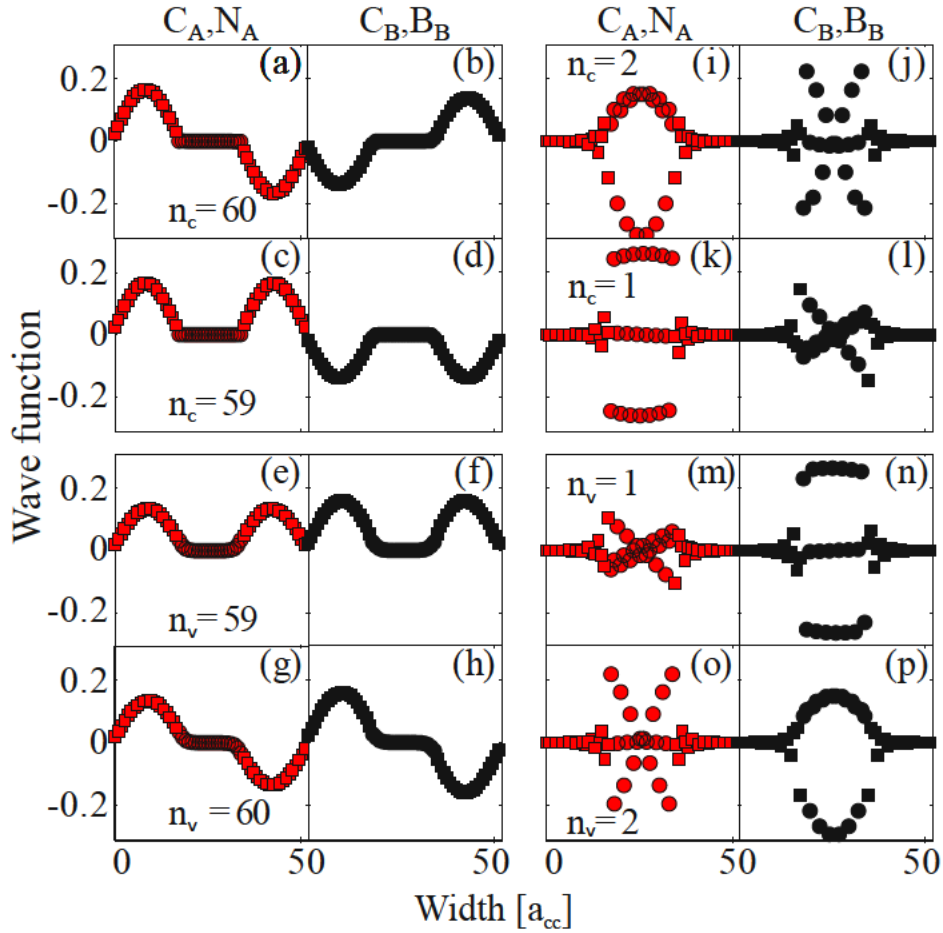
Figure 2.3.: The wavefunctions of a $AGNR_{20}BN_{40}$ at C_A (red circles), N_A (red squares), C_B (black circles), and B_B (black squares). $n_c = 1$ ($n_v = 1$) represents the lowest conduction (highest valence) subband.

are obtained as $\Omega_A = \Omega_B = N_x(N+1)/2$, where N_x is the number of unit cells along the x direction. For a perfect and uniform ribbon we just need to perform the calculations over one unit-cell, therefore, from here on we assume $N_x = 1$. Finally, the coefficients C_A and C_B in Eq. 2.18 are found by solving the Schrödinger equation, $H|\psi\rangle = E|\psi\rangle$, resulting in $C_B = \pm C_A e^{-i\varphi_n(k_x)}$, where $\varphi_n(k_x)$ is defined as

$$e^{i\varphi_n(k_x)} = \frac{f_n(k_x)}{|f_n(kx)|}, \tag{2.21}$$

in which $f_n(k_x) = e^{ik_x a_{cc}} + 2e^{-ik_x a_{cc}/2}\cos(n\theta)$. To satisfy the normalization condition, $|C_A|^2 + |C_B|^2 = 1$, one can choose $C_A = 1/\sqrt{2}$ and $C_B = \pm e^{-\varphi_n(k_x)}/\sqrt{2}$. The

28

wavefunction is given by

$$|\pm, n, k_x\rangle = \frac{1}{\sqrt{(N+1)}} \left[\sum_{p=1}^{N} \left(e^{ik_x x_p^A} \sin(n\theta p)|A_p\rangle \mp e^{-i\varphi_n(k_x)} e^{ik_x x_p^B} \sin(n\theta p)|B_p\rangle \right) \right], \tag{2.22}$$

where the notation $|\pm, n, k_x\rangle \equiv |\psi_n^\pm(k_x)\rangle$ is introduced and $\pm$ denote the conduction and the valence bands, respectively.

Based on Eq. 2.22, one can approximate the wave functions of an H-AGNR at pth atomic site with $\sin(n\theta p)$ functions, where n is the subband index and $\theta = \pi/(N+1)$. Considering such wave functions, the momentum matrix elements are

$$p_{n,m}(k_x) = \frac{1}{(N+1)} \frac{i m_0}{\hbar} t a_{cc} \left[\sum_{p=1}^{N} \sin(n\theta p) \sin(m\theta p) \right] F_{n,m}(k_x). \tag{2.23}$$

According to this equation, only transitions between valence and conduction subbands with the same band-index are allowed (shown in Appendix A). As shown in Fig. 2.3, the wave functions for AGNRs/BN are not necessarily a single sinusoidal function. The Fourier series of these wave functions contain sinusoidal functions with different arguments and coefficients, which results in more allowed interband-transitions compared to H-AGNRs. Non-zero terms and the symmetry properties of the AGNR/BN wave functions indicate that the interband-transitions between subbands with the same parity are allowed (odd to odd and even to even). This transition rule is more restricted for conventional H-AGNRs where the wave functions consist of complete sine terms (see Eq. A.5) [169]. The rules are also different from that of ZGNRs where interband-transitions from subbands with odd (even) indices to subbands with even (odd) indices are allowed. [170].

2.3. Dielectric Response

We compare our TB results with first principles calculations introduced in Sec. 2.1.1. The optical polarization vector is assumed to be along the transport direction similar to the assumption made in the TB calculation.

Figure 2.4(a) exhibits $\varepsilon_i(\omega)$ and the JDOS of $AGNR_{20}BN_{40}$. In the energy range $0 < \hbar\omega < 2$ eV the JDOS has maxima at $\hbar\omega = 0.3019$, 0.62214, 0.92657, 0.91883, 1.2289, 1.5256, and 1.7349 eV. However, only four of these maxima ($\hbar\omega = 0.3019$, 0.91883, 0.92657, and 1.5256 eV) appear in $\varepsilon_i(\omega)$. From the electronic band-structure in Fig. 2.4(b) it can be shown that the peaks in $\varepsilon_i(\omega)$ are related to transitions from $n_v = 1$ to $n_c = 1$ (A), $n_v = 1$ to $n_c = 3$ (B), $n_v = 2$ to $n_c = 2$ (C), and $n_v = 2$ to $n_c = 4$ (D). Disappeared peaks in $\varepsilon_i(\omega)$ are due to zero momentum matrix elements
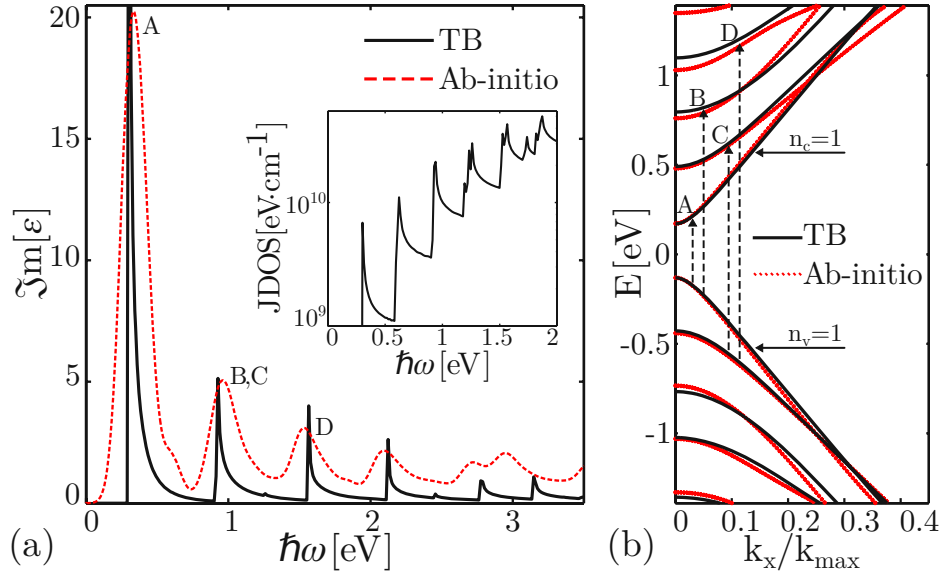
Figure 2.4.: (a) The dielectric function of an $AGNR_{20}BN_{40}$ based on TB (solid line) and first principle calculations (dashed line). The inset shows the related JDOS using the TB model. (b) The electronic band-structure of an $AGNR_{20}BN_{40}$ from TB (solid line) and first principle calculations (red dotted line).

in Eq. 2.4. This transition rule confirms previous results which are explained by the symmetry properties of the wave functions.

Figure 2.4(a) compares the dielectric functions of an $AGNR_{20}BN_{40}$ obtained from TB and first principle calculations. Excellent agreement between these results confirms the transition rules obtained from TB calculations. The energy of the first peak matches well, however, the discrepancies increase for higher peaks. This behavior is related to the differences between the predicted energy-gaps obtained from SIESTA and TB at higher energies, see Fig. 2.4(b).

In order to investigate AGNRs/BN for photodetection application, we study the quantum efficiency defined as $\alpha = (I_{ph}/q)/(P_{op}/\hbar\omega)$, where I_{ph} is the photo current and P_{op} is the incident optical power. We assumed that all absorbed photons contribute to the photo current, such that the quantum efficiency can be calculated from the dielectric function (Eq. 2.4). A quantum efficiency of $6-16\%$ for graphene is reported in Ref. [82] and a maximum quantum efficiency ranging from 9% to 11% is reported for H-AGNRs in Ref. [171]. Figure 2.5 shows the calculated quantum efficiency as a function of the incident photon energy at various GNR widths. The efficiency is maximized when the photon energy matches the bandgap of the nanoribbon (the first peak for each structure). Our results indicate a peak of quantum efficiency in the range of $14-15\%$ for AGNRs/BN. The quantum efficiencies of photodetectors based on AGNRs/BN and H-AGNRs are compared in Fig. 2.5. Due to the presence of more allowed transitions a wider absorption spectrum is achieved in AGNRs/BN compared

30
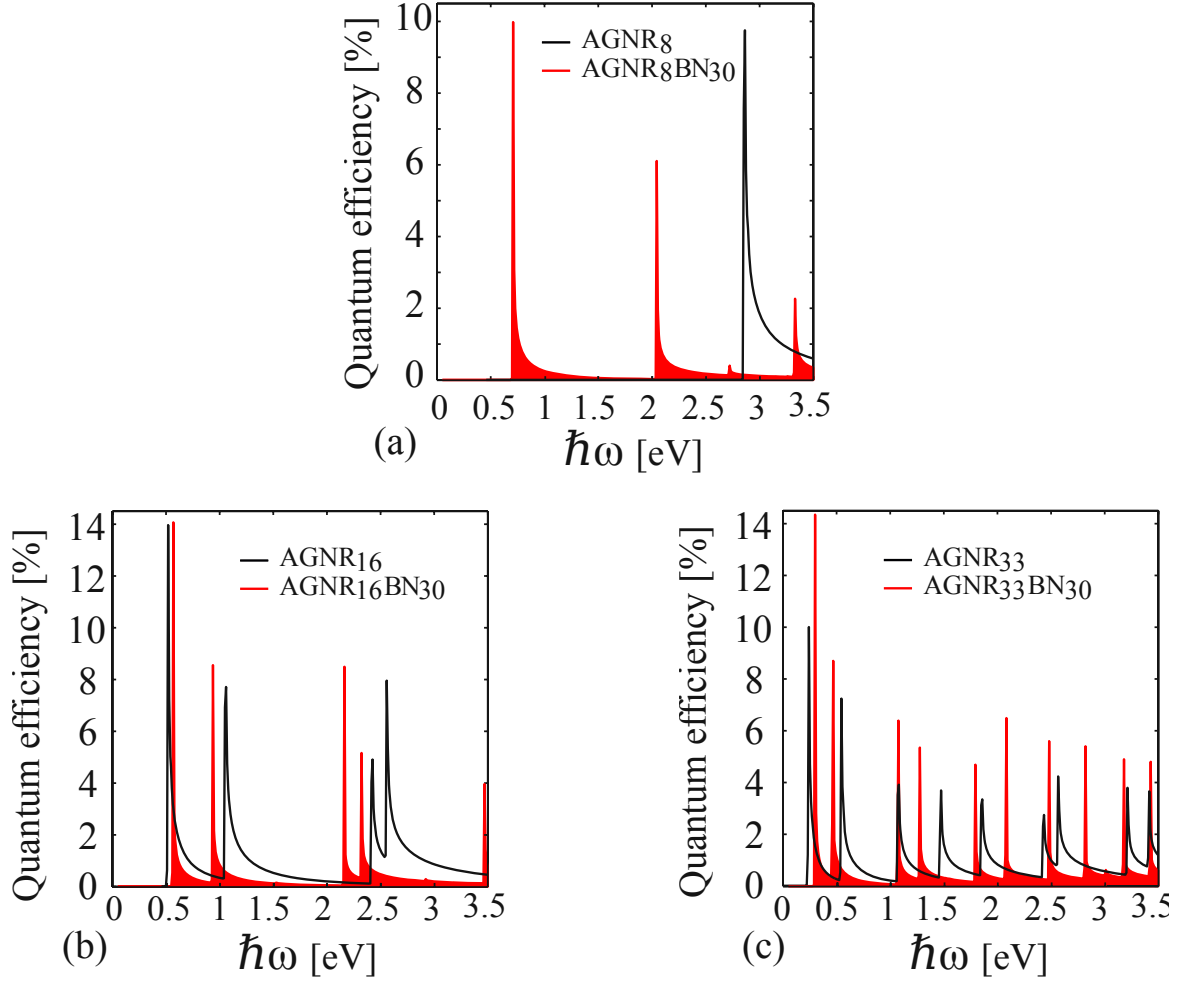
Figure 2.5.: The quantum efficiency of an (a) $AGNR_8BN_{30}$, (b) $AGNR_{16}BN_{30}$, and (c) $AGNR_{33}BN_{30}$ compared to a H-AGNRs with the same indices.

to H-AGNRs. As a H-AGNR with index 8 is metallic, the first peak is related to the second energy-gap and appears at 2.88 eV whereas the $AGNR_8BN_{30}$ shows three peaks below that energy due to energy-gap opening, see Fig. 2.5(a). In Fig. 2.5, the quantum efficiency decreases for the first energies, but increases at higher energies, see for example the sixth peak for $AGNR_{33}BN_{30}$ (Fig. 2.5(c)). This is due to different effective masses of different subbands which affect the JDOS. According to Eq. 2.4, a larger JDOS leads to a larger absorption of photons and a higher quantum efficiency.

We also investigate the photoresponsivity given by (I_{ph}/P_{op}). Our calculations give an upper limit for the photoresponsivities of 0.336 A/W, 0.239 A/W, and 0.202 A/W for photon energies near the bandgaps of $AGNR_8BN_{30}$, $AGNR_{16}BN_{30}$, and $AGNR_{33}BN_{30}$ respectively. Due to the higher quantum efficiency of AGNRs/BN compared to AG-NRs, a higher photoresponsivity is obtained for the same input optical power of 10^7 W/m^2.

2.4. Conclusions

In summary, we theoretically studied the optical properties of AGNRs/BN, employing TB calculations. We demonstrate that in AGNRs/BN only optical transitions from subbands with odd (even) indices to subbands with odd (even) indices are allowed. This transition rule is more restricted for AGNRs and completely different from that of ZGNRs. Our TB results are in agreement with first principle calculations which verifies the accuracy of our model. The applicability of AGNRs/BN as photodetectors is investigated. Our results indicate that due to more allowed transitions compared to conventional GNRs a larger photo current in AGNR/BN structures can be achieved. The results render AGNRs/BN as suitable candidates for infrared photodetectors and future optoelectronic applications.

3. Optical Properties of Zigzag Graphene Nanoribbons

The energy band structure of AGNRs can be obtained by making the transverse wavenumber discrete, in accordance with the edge boundary condition, which is analogous to the case of carbon nanotubes where periodic boundary conditions apply [172]. An analytical model for the dispersion relation and the wave functions of AGNRs is presented in Ref. [168]. However, because in ZGNRs the transverse wavenumber depends not only on the ribbon width but also on the longitudinal wavenumber, the energy band structure cannot be obtained simply by slicing the bulk graphene band structure. Therefore, exact analytical models can not be derived for ZGNRs [172]. In this chapter, we present two approximations for the wavenumber of ZGNRs which result in simple analytical expressions for band-structure and wave functions. We show that the analytical model is valid for a wide range of GNR indices.

3.1. Electronic Band Structure

The structure of graphene consists of two types of sublattices A and B, see Fig. 3.1. We start with the Hamiltonian (Eq. 2.6) and wave functions (Eq. 2.18 and Eq. 2.19) of graphene and derive the analytical expressions for ZGNRs.

To obtain ϕ_p in wave functions $|\psi_A|$ and $|\psi_B|$, one can substitute the ansatz for the wave functions into the Schrödinger equation. An A-type carbon atom at some atomic site n has one B-type atom at some atomic site $N - n$ and two B-type neighbors at $N - n + 1$, see Fig. 3.1:

$$\begin{cases} tf \ \phi^B_{N-n+1} + t \ \phi^B_{N-n} = E \ \phi^A_n, \\ t \ \phi^A_{n-1} + tf \ \phi^A_n = E \ \phi^B_{N-n+1} \ , \end{cases} \tag{3.1}$$

replacing the index n with $n + 1$ in the second relation of Eq. 3.1, one obtains:

$$\phi^B_{N-n} = (1/E)(t\phi^A_n + tf\phi^A_{n+1}). \tag{3.2}$$

Substituting this relation in Eq. 3.1 one can rewrite Eq. 3.1 as:

$$C\phi^A_n = \phi^A_{n+1} + \phi^A_{n-1} \ , \tag{3.3}$$
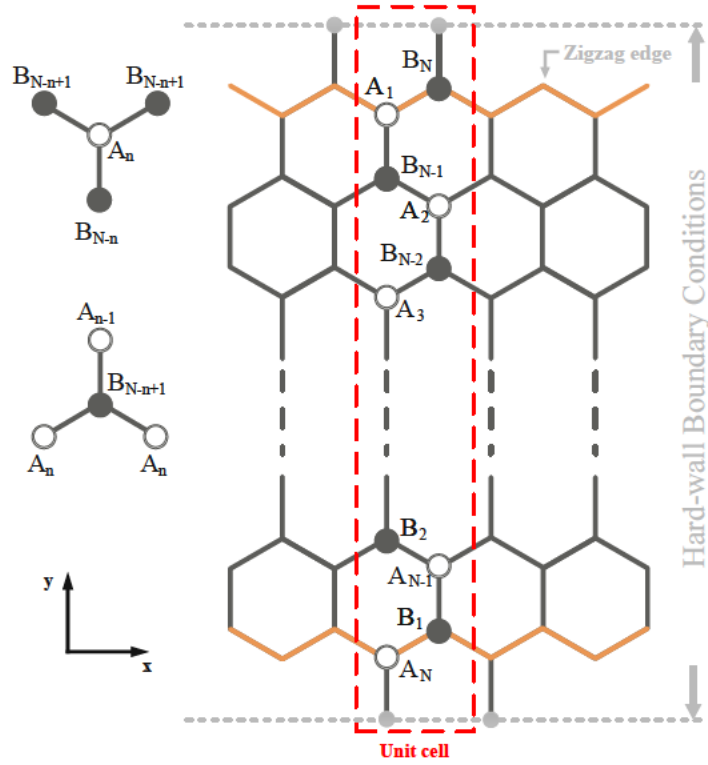
Figure 3.1.: The structure of a GNR with zigzag edges along the x direction. Each unit cell consists of N atoms at the sublattice A or B. A hard wall boundary condition is imposed on the both edges.

with:

$$C = \frac{(E/t)^2 - f^2 - 1}{f} \quad \text{and} \quad f = 2\cos(\mathbf{k}.\mathbf{a}/2) = 2\cos\left(\frac{\sqrt{3}}{2}k_x a_{cc}\right). \tag{3.4}$$

Due to symmetry, a similar relation holds for the B-type carbon atoms:

$$C\phi_n^B = \phi_{n+1}^B + \phi_{n-1}^B. \tag{3.5}$$

Considering the boundary condition $\phi_0^A = \phi_0^B = 0$, the solution to the recursive formula is given by (see Appendix B.2):

$$\phi_n^B = \frac{\left(\frac{C + \sqrt{C^2 - 4}}{2}\right)^n - \left(\frac{C - \sqrt{C^2 - 4}}{2}\right)^n}{\sqrt{C^2 - 4}}\phi_1^B. \tag{3.6}$$

Depending on the values of C, Eq. 3.4 can have three different solutions. For $|C| > 2$, ϕ_n^B has a hyperbolic solution where the wave function is localized at the edges of the

ribbon:

$$\phi_n^B = \frac{2\sinh(n\theta)}{\sqrt{C^2 - 4}}\phi_1^B \; , \tag{3.7}$$

where θ is given by:

$$C = 2\cosh(\theta). \tag{3.8}$$

For $C = \pm 2$, the amplitude of the wave function increases linearly with n. This critical case appears at the transition point from localized states to delocalized states. For $|C| < 2$, $\sqrt{C^2 - 4}$ is a pure imaginary number. The solution ϕ_n^B is, therefore, given by:

$$\phi_n^B = \frac{\left(\dfrac{C + i\sqrt{4 - C^2}}{2}\right)^n - \left(\dfrac{C - i\sqrt{4 - C^2}}{2}\right)^n}{i\sqrt{4 - C^2}}\phi_1^B \tag{3.9}$$

$$\phi_n^B = \frac{2\sin(n\theta)}{\sqrt{4 - C^2}}\phi_1^B = \frac{\sin(n\theta)}{\sin(\theta)}\phi_1^B \; , \tag{3.10}$$

where θ is the wavenumber and is given by

$$C = 2\cos(\theta). \tag{3.11}$$

Under this condition the wave function has an oscillatory behavior and is not localized.

The prefactors C_A and C_B in Eq. 2.18 are found to be $C_A = \pm C_B$, see Appendix B.1. To simplify the equations we assume $\phi_1^{A/B} = \sin(\theta)$.

Therefore, the wave functions become

$$|\psi\rangle = \frac{1}{\sqrt{\Omega}}\sum_{n=1}^{N} e^{ik_x x_n^A}\sin(n\theta)|A_n\rangle \pm \frac{1}{\sqrt{\Omega}}\sum_{n=1}^{N} e^{ik_x x_n^B}\sin(n\theta)|B_n\rangle. \tag{3.12}$$

To obtain the normalization factor Ω, one has to impose the following condition [168] in the Eq. 2.19:

$$\langle\psi_A|\psi_A\rangle = \langle\psi_B|\psi_B\rangle = 1/2. \tag{3.13}$$

By substuting Eq. 3.12 in Eq. 3.13 one obtains

$$\langle\psi_A|\psi_A\rangle = \frac{1}{\Omega}\sum_{n=1}^{N}\left(\sin^2(n\theta)\right) = 1/2. \tag{3.14}$$

It is straightforward to obtain $\Omega_{A/B} = \Omega$ as

$$\Omega = 2\sum_{n=1}^{N} \sin^2(n\theta) = N - \frac{\sin(N\theta)}{\sin(\theta)}\cos((N+1)\theta)$$

$$= \frac{1}{2}\left(1 + 2N - \frac{\sin(2N+1)\theta}{\sin(\theta)}\right). \tag{3.15}$$

In principle θ can not be derived analytically for ZGNRs. However, two approximations for θ are discussed in Sec. 3.2. Using the analytical approximated θ calculated in Eq. 3.28, Eq. 3.15 can be simplified as

$$\Omega = N + 1/2. \tag{3.16}$$

In order to obtain the respective energy spectrum, Eq. 3.4 can be written as

$$E = \pm t\left[Cf + f^2 + 1\right]^{1/2}. \tag{3.17}$$

By substituting Eq. 3.4 and Eq. 3.11 in Eq. 3.17, the energy dispersion relation takes the form

$$E = \pm t\left[1 + 4\cos^2\left(\frac{\sqrt{3}}{2}k_x a_{cc}\right) + 4\cos\left(\frac{\sqrt{3}}{2}k_x a_{cc}\right)\cos(\theta)\right]^{1/2}. \tag{3.18}$$

3.2. Wave Functions

In the following, the relation between θ and k_x is obtained. Setting $n = N + 1$ in Eq. 3.1 gives

$$E\phi_0^B = t\phi_N^A + 2t\cos\left(\frac{\sqrt{3}}{2}k_x a_{cc}\right)\phi_{N+1}^A. \tag{3.19}$$

On the other hand the wave functions for $n = N$ and $n = N+1$ are given by Eq. 3.10

$$\phi_N^A = \frac{\sin(N\theta)}{\sin(\theta)}\phi_1^A,$$

$$\phi_{N+1}^A = \frac{\sin((N+1)\theta)}{\sin(\theta)}\phi_1^A. \tag{3.20}$$

By imposing a hardwall boundary condition, $\phi_0^B = 0$, Eq. 3.19 can be rewritten as

$$t\frac{\sin(N\theta)}{\sin(\theta)}\phi_1^A + 2t\cos\left(\frac{\sqrt{3}}{2}k_x a_{cc}\right)\frac{\sin((N+1)\theta)}{\sin(\theta)}\phi_1^A = 0, \tag{3.21}$$

36
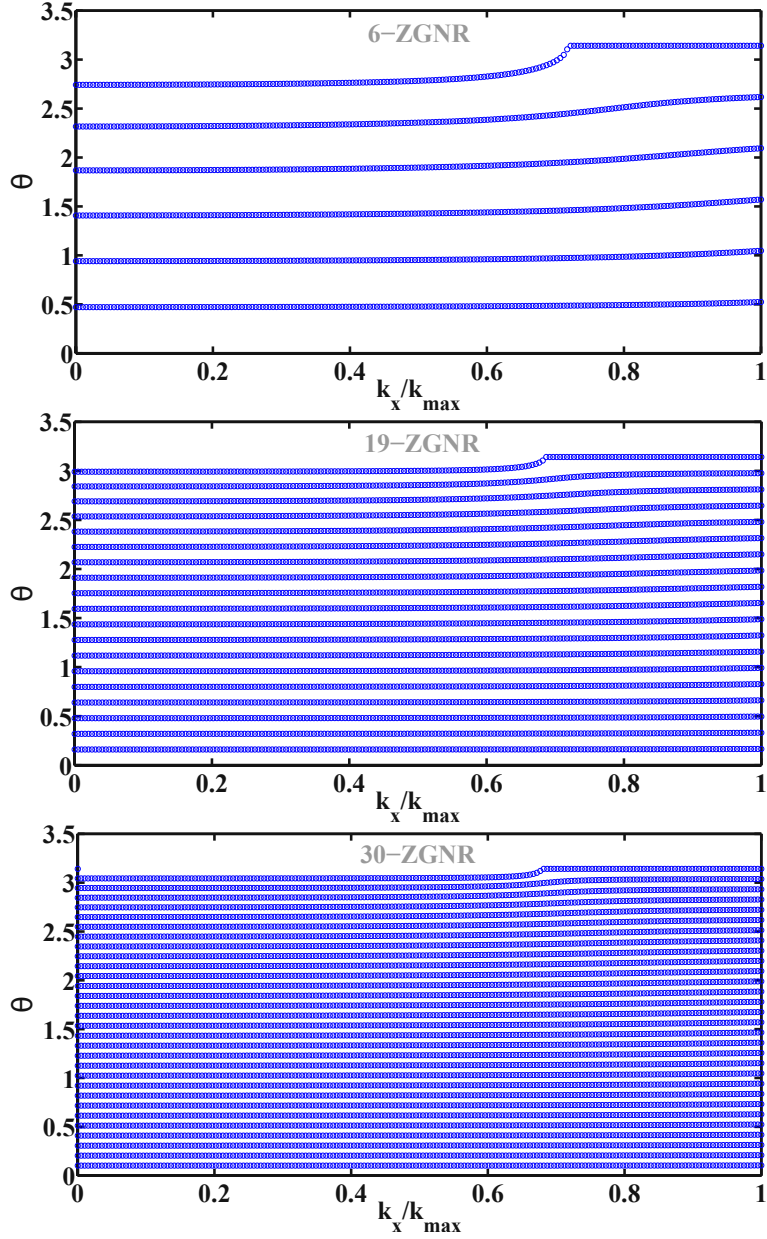
Figure 3.2.: Numerically evaluated the wavenumber θ as a function of k_x for 6-ZGNR, 19-ZGNR, and 30-ZGNR.

and we obtain the quantization condition,

$$\frac{\sin{(N\theta)}}{\sin{((N+1)\,\theta)}} = -2\cos\left(\frac{\sqrt{3}}{2}k_x a_{cc}\right). \tag{3.22}$$

From Eq. 3.22, θ can be extracted and used in the analytical derivation of the wave functions and energy dispersion relation of ZGNRs. Figure 3.2 shows the variation of

37
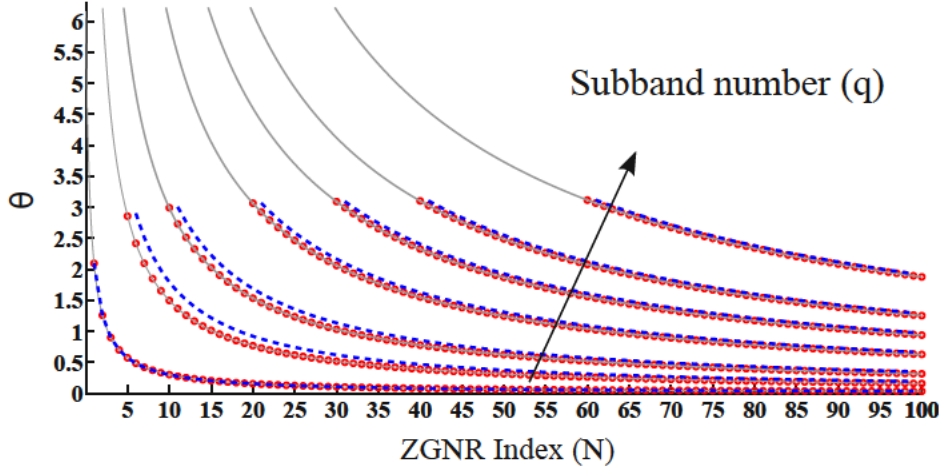
Figure 3.3.: The wavenumber θ as a function of the ribbon index, N, for different subband numbers, q. Dashed lines show the first approximation (Eq. 3.25) and circles show the second approximation (Eq. 3.28).

θ as a function of k_x for different subbands.

As can be seen, a weak dependency exists between θ and k_x. However, we assume a constant θ with respect to k_x, so the right hand side of Eq. 3.22 becomes a constant. At this point, two approaches exist to simplify Eq. 3.22 based on choosing k_x. In general, using all k_x in the range of $[0, \pi/\sqrt{3}a_{cc}]$ except $k_x = 2\pi/3\sqrt{3}a_{cc}$ results in non analytical solution and curve fitting is required to extract θ. This approach is first discussed. For $k_x = 0$, Eq. 3.22 can be written as

$$\frac{\sin(N\theta)}{\sin((N+1)\theta)} = -2. \tag{3.23}$$

Using curve fitting one finds

$$\theta = \frac{Q}{N+P} = \begin{cases} Q = p_1 v + p_2 \\ P = p_1' v + p_2', \end{cases} \tag{3.24}$$

where v is related to the subband number q ($q = 2v$) and N is the index of ZGNR. p_1, p_2, p_1' and p_2' are fitting factors. Performing a fit for the range of $N \in [6, 100]$,

$$\theta = \frac{3.31v - 0.5208}{N + 0.07003v + 0.5216}. \tag{3.25}$$

Figure 3.3 compares θ obtained from Eq. 3.25 with exact numerical results.

Another approach for approximating θ is selecting $k_x = 2\pi/3\sqrt{3}a_{cc}$ which makes the
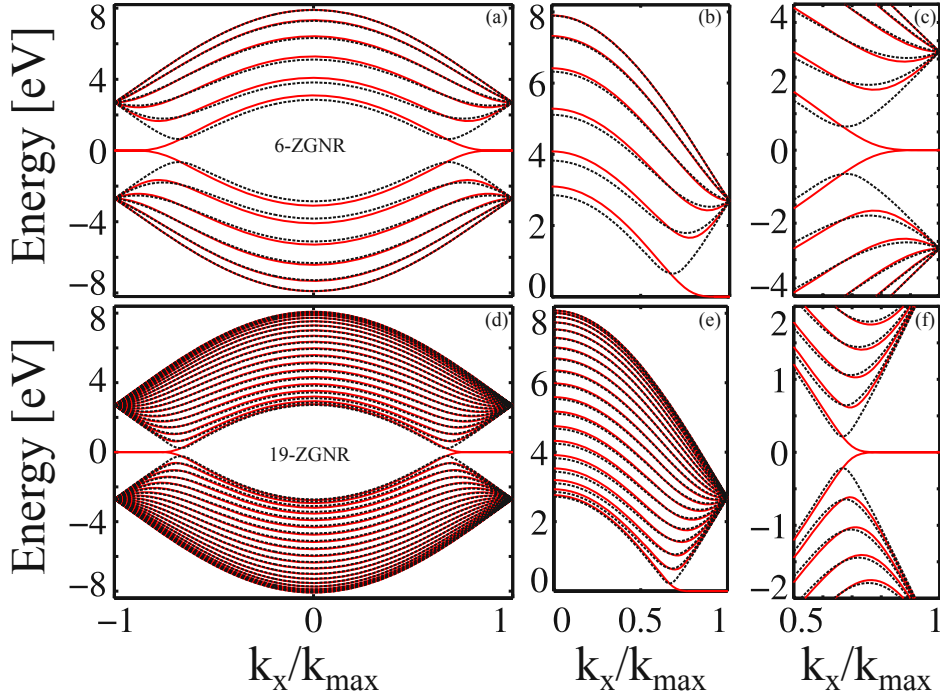
Figure 3.4.: The electronic band structure of 6-ZGNR ((a), (b), and (c)) and 19-ZGNR ((d), (e), and (f)). The analytical model (black dashed lines) is compared against the numerical results (red solid lines).

right side of Eq. 3.22 equal to -1

$$\begin{aligned} \sin(N\theta) + \sin((N+1)\theta) &= 0, \\ 2\sin((2N+1)\,\theta/2)\cos(\theta/2) &= 0, \end{aligned} \tag{3.26}$$

and has the following solution

$$\theta = \frac{\upsilon\pi}{N + 1/2}. \tag{3.27}$$

By representing υ in terms of subband index q, θ is obtained as a function of q and N,

$$\theta = \frac{q\pi}{2N + 1}. \tag{3.28}$$

Figure 3.3 compares the discussed approximations with exact numerical results. The value of θ for Eq. 3.28 shows a good agreement with that obtained from numerical calculations. The approximation is valid for a wide range of ZGNR indices. Using the analytical expression for θ, analytical wave functions and energy dispersion are evaluated from Eq. 3.12 and Eq. 3.18. The results for a 6-ZGNR and a 19-ZGNR are shown in Fig. 3.4 and Fig. 3.5, respectively.

3.3. Optical Matrix Elements

Optical transition rules can be obtained from the optical matrix elements. The interband optical matrix element determines the probability for a transition from a state $|m\rangle$ to a final state $|n\rangle$ and is given by $(q/m_0)\langle n|\boldsymbol{A}\cdot\boldsymbol{p}|m\rangle$, [150] where q is the elementary charge, m_0 is the electron mass, $\boldsymbol{A} = A\boldsymbol{a}$ is the vector potential, $\boldsymbol{a}$ is a unit vector parallel to $\boldsymbol{A}$, and $\boldsymbol{p}$ is the linear momentum operator. The vector potential can be separated from the expectation value assuming the wave vector of the electromagnetic field is negligible compared to the electronic wave vector (dipole approximation). We have already used this approximation to derive the electron-photon interaction Hamiltonian (Eq. 2.10). As a result, optical matrix elements can be achieved by evaluating momentum matrix elements $p_{n,m} = \langle n|p_x|m\rangle$. In this work the electromagnetic field is assumed to be polarized along the x direction.

Knowing the wave function of atomic orbitals, [173] the matrix elements of the momentum operator can be calculated from Eq. 2.13. However, in most of the tight-binding models the atomic orbitals are unknown, a difficulty which is usually circumvented by the gradient approximation [162], see Sec. 2.1.3. In this approximation intra-atomic transitions are ignored. However, as we employ a single orbital model to describe the electronic band-structure of ZGNRs, intra-atomic transitions are intrinsically neglected.

With the wave functions derived in the previous section, evaluation of transition rules from Eq. 2.13 is possible. Using the wave functions from Eq. 3.12 in Eq. 2.13, and considering only nearest neighbors, one can obtain (see Appendix B.3)

$$P_{\theta,\theta'} = \frac{2\sqrt{3}m_0 a_{cc}t}{\hbar(2N+1)}\sin\left(\frac{\sqrt{3}}{2}ka_{cc}\right)$$
$$\sum_{n=1}^{2N}\left[\sin(n\theta')\sin((2N-n+1)\theta) - \sin(n\theta)\sin((2N-n+1)\theta')\right].$$

(3.29)

The upper limit of summation $2N$ is due to degenerate points of valance and conduction bands at $k_x = \pm 2\pi/3\sqrt{3}a_{cc}$. The subband indices are included in θ and θ', see Eq. 3.28. The summation over sine functions in Eq. 3.29 determines the transition
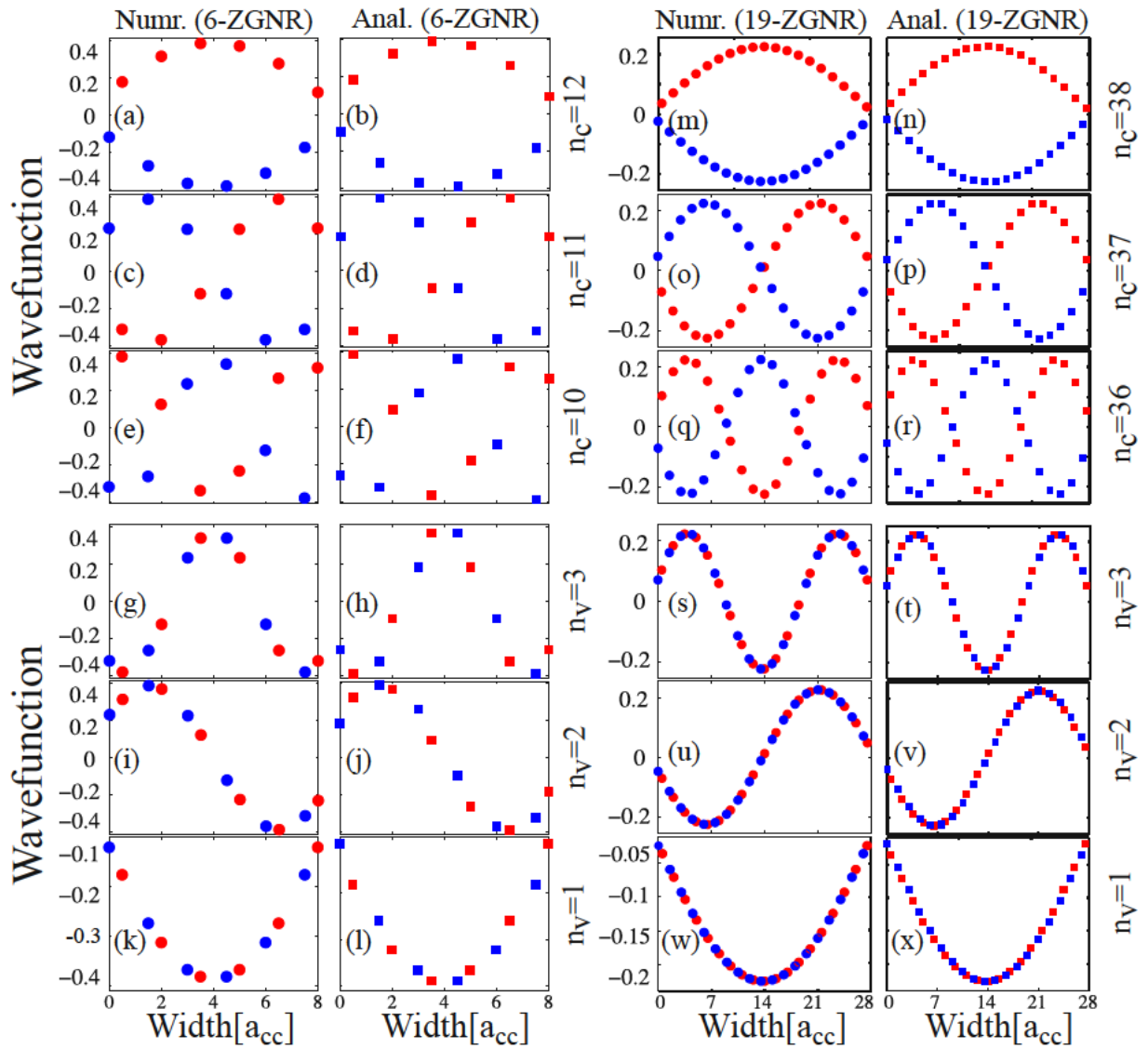
Figure 3.5.: The wave functions of 6-ZGNR and 19-ZGNR. Red(Blue) symbols denote the wave functions in sublattice $B(A)$. The analytical model (squares) are compared against the numerical results (circles).

rules. By some trigonometric identities one can rewrite this summation as follows

$$
P_{\theta,\theta'} = \frac{-2\sqrt{3}m_0 a_{cc} t}{\hbar(2N+1)} \sin\left(\frac{\sqrt{3}}{2}ka_{cc}\right)
$$
$$
\left[\frac{\cos\left((2N+1)(\theta+\theta')/2\right)\sin\left(2N(\theta-\theta')/2\right)}{\sin\left((\theta-\theta')/2\right)}\right.
$$
$$
\left. - \frac{\cos\left((2N+1)(\theta-\theta')/2\right)\sin\left(2N(\theta+\theta')/2\right)}{\sin\left((\theta+\theta')/2\right)}\right].
\tag{3.30}
$$

Using the analytical approximation of θ in Eq. 3.28 for the cosine terms in Eq. 3.30 gives

$$\cos\left((2N+1)(\theta \pm \theta')/2\right) = \cos\left((q \pm q')\frac{\pi}{2}\right). \tag{3.31}$$

If $q = 2r + 1$ and $q' = 2r'$ or $q = 2r$ and $q' = 2r' + 1$, where r and r' are non-zero integers, $q \pm q' = 2r'' + 1$, both terms in the bracket of Eq. 3.30 will be zero. In the case of $q = 2r$ and $q' = 2r'$ or $q = 2r + 1$ and $q' = 2r' + 1$, the terms in the bracket will be non zero. Therefore, the transitions between valence and conduction subbands only with the same parity (odd to odd and even to even) are allowed,

$$P_{\theta,\theta'} = P_{q,q'} = \begin{cases} 0, & \text{if } q = \text{odd (even) and } q' = \text{even (odd)}, \\ \neq 0, & \text{if } q = \text{odd (even) and } q' = \text{odd (even)}. \end{cases} \tag{3.32}$$

3.4. Results and Discussion

In this section, the energy dispersion relation and the wave functions for the approximated discrete wavenumbers θ are evaluated and compared against exact numerical calculations. Eq. 3.28 is employed to give the wave functions and energy dispersions from Eq. 3.12 and Eq. 3.18, respectively. Based on the structure depicted in Fig. 3.1, the width of a zigzag nanoribbon is given by

$$W = \left(\frac{3N}{2} + 1\right)a_{cc}, \tag{3.33}$$

where $a_{cc} = 1.42$ Å is the carbon-carbon bond length in graphene. For ZGNRs with a width below 50nm, indices in the range 6 to 235 have to be considered. In this range of indices the wave functions and the energy dispersion have been evaluated. It should be noted that structures wider than 50nm are also evaluated and the results show excellent agreement with those obtained from numerical simulation. Fig. 3.6 shows several wave functions for 125-ZGNR evaluated from two approximations proposed. As can be seen, the wave functions obtained by Eq. 3.28 are matched very well with the numerical calculations. The dispersion relation of some subbands for 125-ZGNR are shown in Fig. 3.7. Similar to the wave functions, the dispersion relations obtained by θ from Eq. 3.28, show well agreement with the numerical results.

An important conclusion that one can draw from these results is that the analytical approximation of θ presented in Eq. 3.28 is more accurate than the solution obtained by using a curve fitted θ, see Fig. 3.6 and Fig. 3.7. Also, the accuracy of the analytical method increases as the ZGNR index increases (see the energy dispersions for 6-ZGNR and 19-ZGNR in Fig. 3.4 and 125-ZGNR in Fig. 3.7). As can be see in Fig. 3.2, this
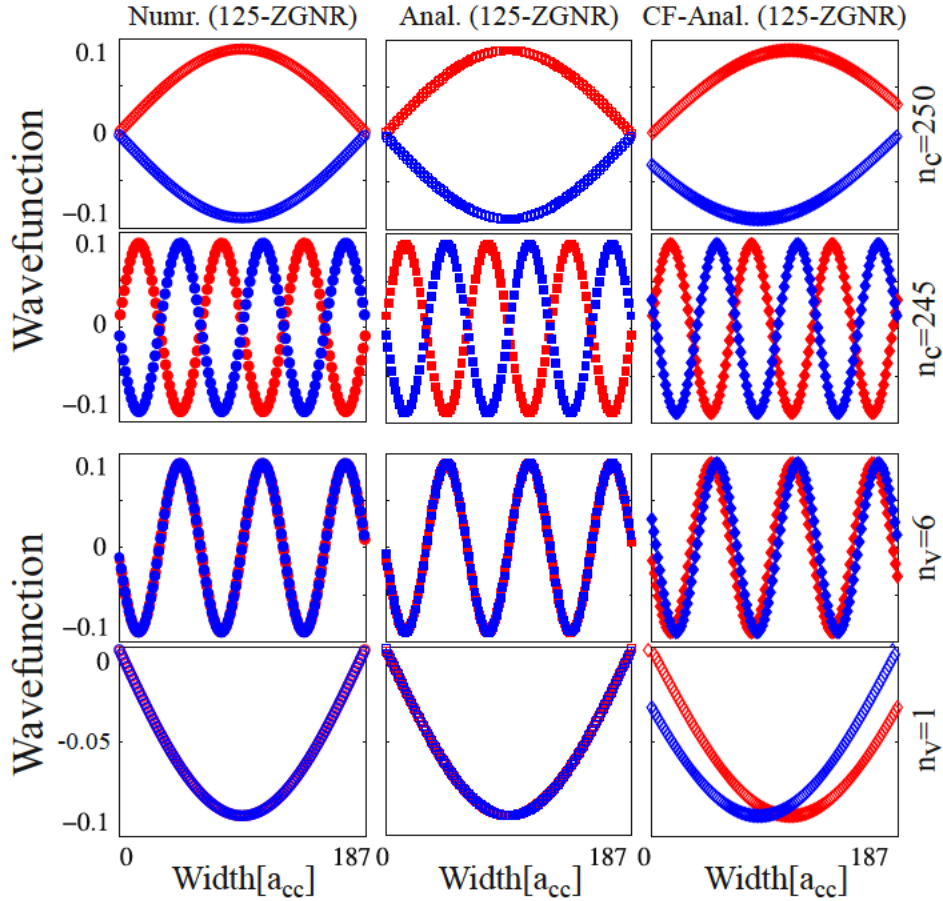
Figure 3.6.: The wave functions of 125-ZGNR. Red(Blue) symbols denote the wave functions at the sublattice $B(A)$. The analytical model (squares) and curve fitted model (diamonds), are compared against the numerical results (circles) for different subbands.

increase in accuracy is due to the fact that θ is relatively independent of changes in the wave-vector (k_x) for large values of N.

In order to investigate the applicability of the proposed models, the optical matrix elements are derived analytically based on our models in 3.3. To evaluate the transition rules, we can also investigate the symmetry of the transition matrix element in Eq. 2.23. If the symmetry of this element spans the totally symmetric representation of the point group to which the unit cell belongs, then its value is not zero and the transition is allowed. Otherwise, the transition is forbidden. Assuming a uniform potential profile across the ribbon's width, the subbands' wave functions are either symmetric or antisymmetric along the y direction.

Considering the wave functions for 6-ZGNR and 19-ZGNR (Fig. 3.5), subbands corresponding to odd indices are symmetric, while those corresponding to even indices
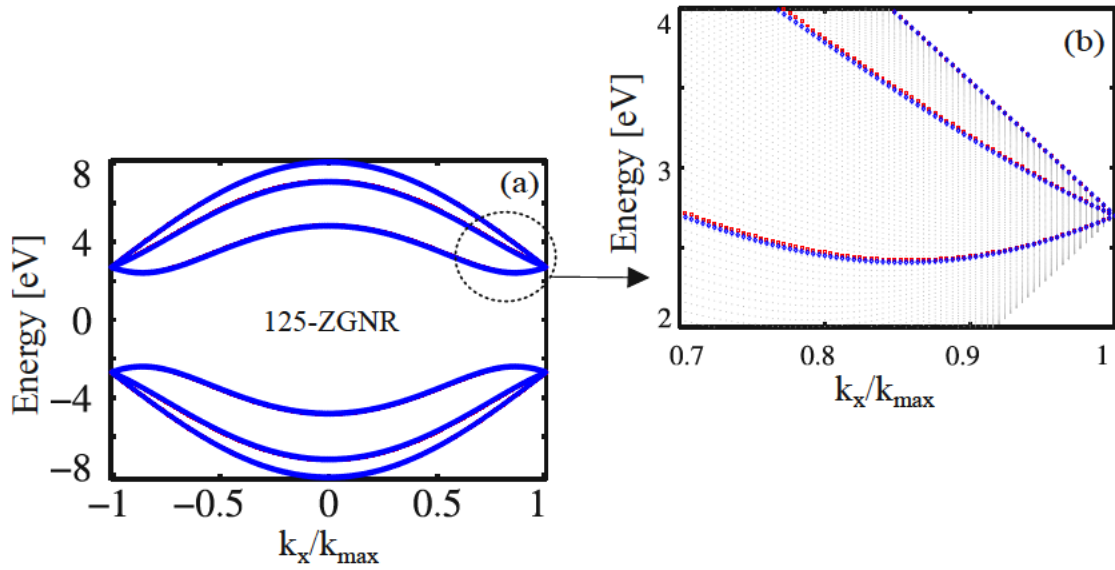
Figure 3.7.: The electronic band structure of 125-ZGNR. The analytical model (red symbols) and the curve fitted (blue symbols) are compared with the numerical results (black symbols).

are antisymmetric. Therefore, the momentum matrix elements are non zero for transitions from the symmetric (antisymmetric) to the symmetric (antisymmetric) wave functions. This transition rule results in transitions from subbands with odd (even) to odd (even) indices in ZGNRs, [151] which confirms the result obtained from our analytical derivation of the wave functions and momentum matrix elements.

To demonstrate the applicability of our models the imaginary part of the dielectric function ε_i (Eq. 2.4) is calculated numerically for 6-ZGNR and 19-ZGNR (see Fig. 3.8(a) and Fig. 3.8(b)). Peaks in $\varepsilon_i(\omega)$ indicate absorptions of photons with energy $\hbar\omega$. From the electronic band-structure in Fig. 3.8(c) it can be found that the peaks in $\varepsilon_i(\omega)$ are related to transitions from $n = 6$ to $n = 8$ (A), and $n = 6$ to $n = 10$ (C). The minimum designated as (B) is related to the transition from $n = 6$ to $n = 9$ which is forbidden according to the obtained transition rules. The same analysis exists for 19-ZGNR, see Fig. 3.8(b) and Fig. 3.8(d). Therefore, the allowed transitions are from odd to odd and even to even subband numbers, which is in agreement with our analytical derivation.

3.5. Conclusions

We presented two methods for analytical approximation of the discrete energies in ZGNRs. Relations for the wave functions and the energy dispersion show good agreement with those obtained from numerical calculations. Our simple approximation is applicable for a wide range of ZGNR indices from N=6 to N=500. While the results
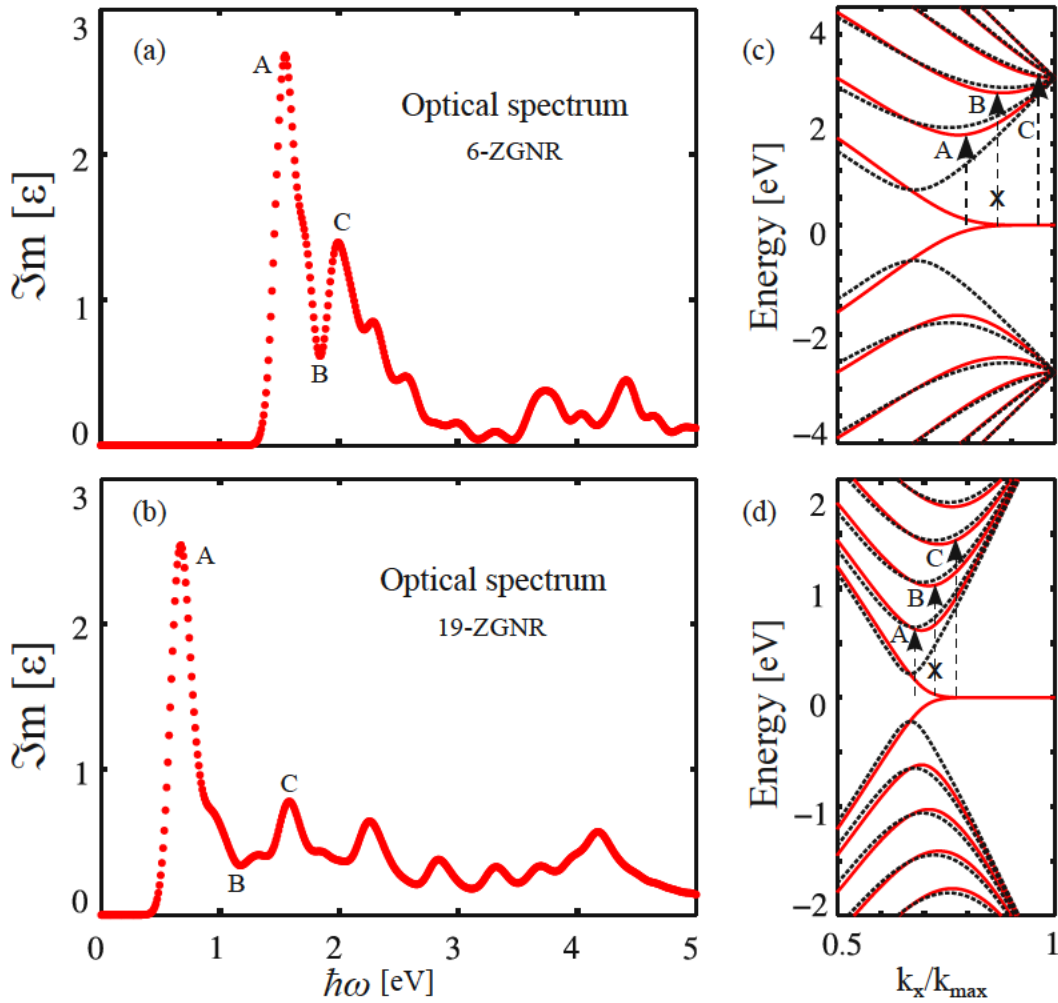
Figure 3.8.: Dielectric function of (a) 6-ZGNR and (b) 19-ZGNR. The peaks are related to electronic band structure of (c) 6-ZGNR and (d) 19-ZGNR.

show good agreement for small N-ZGNRs, the accuracy increases for wider ZGNRs. The analytical approach presented here is used to drive transition rules. Our model shows that transitions from odd to odd and even to even subband numbers are allowed and that other transitions are forbidden in ZGNRs. The model is applicable for the evaluation of optical properties of ZGNRs such as dielectric response, absorption coefficient, and energy loss spectrum.

45

4. Graphene Superlattice-Based Photodetectors

Superlattices and various quantum structures obtained thereof have drawn much attention in past decades [46]. Commensurate or pseudomorphic junctions of two different semiconductors have been grown layer by layer to form a periodically repeating superlattice structure with sharp lattice-matched interface [96,174,175]. Owing to the band discontinuities at the interface, they behave as a multiple quantum well structure according to the effective mass theory. Electrons confined in these quantum wells exhibit two-dimensional electron-gas behavior with interesting quantum effects [46]. Two-dimensional conduction-band electrons (valence-band holes) confined to the wells have displayed a number of electronic and optical properties [96, 174–177].

In this chapter, the optical properties of hydrogen-passivated armchair graphene nanoribbons superlattices (HSLs) and boron-nitride-passivated armchair graphene nanoribbons superlattices (BNSLs) are studied.

The results indicate high responsivity and quantum efficiency as well as long wavelength operation which render these devices as potential candidates for future photodetection applications.

Figure 4.1 shows the structure of the studied superlattices. In the structure shown in Fig. 4.1(a) the dangling bonds of edge carbon atoms are saturated by hydrogen atoms, whereas in the structure shown in Fig. 4.1(b) the semiconducting region (formed by carbon atoms) is surrounded by BN. Throughout this study, the structures in Fig. 4.1(a) and (b) are used as main structures which are referred to as HSL(11) and BNSL(11), respectively. The numbers inside the parentheses represent the number of carbon atoms along the width of the wider part of the superlattice (n_w).

Lengths of $8a_{cc}$ and $7a_{cc}$ are considered for the well and barrier regions, respectively, where $a_{cc} = 1.42$ Å is the carbon-carbon bonding distance. To investigate the optical properties of these superlattice structures, the non-equilibrium Green's function (NEGF) formalism introduced in Sec. 2.1.3 along with a tight-binding (TB) model for the electronic bandstructure (Sec. 2.1.2) are employed. The TB parameters are modified to match the results with first principle calculations. For first principle calculations we employed the SIESTA package [152]. The parameters used for the DFT calculation are given in Sec.2.1.1.
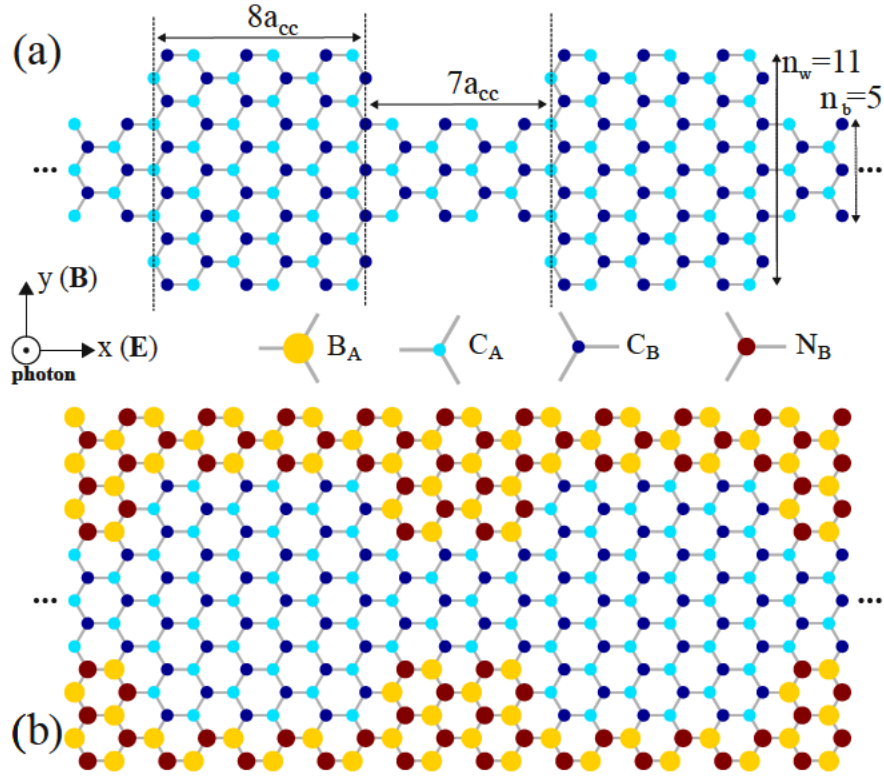
Figure 4.1.: The structure of (a) a hydrogen-passivated superlattice, and (b) a boron nitride-confined superlattice. Both superlattices have the same index for the graphene nanoribbon part. $C_{A/B}$ represents a carbon, $N_{A/B}$ a nitrogen, and $B_{A/B}$ a boron atom at the sublattice A or B. n_w and n_b denote the well and barrier indices respectively.

4.1. Graphene Superlattice Properties

Figure 4.2 compares the bandstructures for HSL(11) and BNSL(11) based on the TB model and first principles calculations. Carbon-carbon interactions up to three nearest neighbors are considered in the TB calculations for HSLs. In the case of BNSLs, a more careful choice of the TB parameters is required due to the ionicities of the boron and nitrogen atoms at the edges of the superlattice. The tight-binding parameters proposed in Table 4.1 result in electronic disperse relations that are in excellent agreement with first-principle simulations. In this table, t_{XY} and $t_{XY,2}$ denote the hopping parameter between the first and second nearest neighbor X and Y atoms, where X and Y represent carbon C, boron B, or nitrogen N atoms. Δ_{XX} denotes the on-site potential of atom X. As shown in Fig. 4.2(a), larger energy gaps are achieved for BNSLs in comparison with HSLs, which is attributed to the large ionic potential difference between boron and nitrogen atoms in BNSLs [135].

The bandgap as a function of the width of superlattice is depicted in Fig. 4.2(d). Zigzag edges in a graphene layer induce an opposite spin orientation across the ribbon
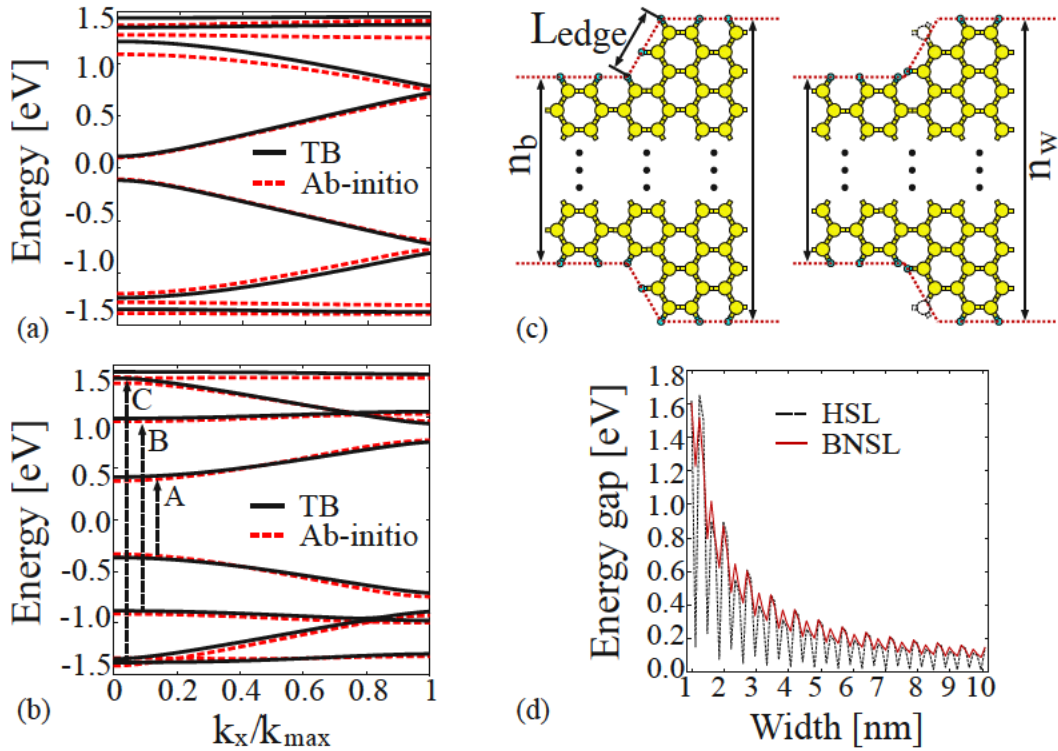
Figure 4.2.: The electronic bandstructure for (a) a HSL(11), and (b) a BNSL(11) based on the TB model and first principles calculations. (c) The geometrical parameters of the structure. (d) Energy gap as a function of n_w for a HSL and a BNSL.

between ferromagnetically ordered edge state [178]. In such cases, additional spin analysis is necessary which is beyond the scope of this work. To avoid zigzag edges, we assumed that n_w and n_b are scaled such that L_{edge} is kept constant, where n_w and n_b are defined as the number of dimer lines in the well and barrier of the superlattice, respectively, see Fig. 4.2(c). Figure 4.2(d) shows that HSLs, unlike BNSLs, have relatively small bandgap for specific values of $n_w = 3p + 2$, where p is a positive integer. In addition, the scaling of the energy gap with the width in BNSLs shows a more uniform behavior compared to that of HSLs. An important point to notice is

t_{CC}	t_{BB}	t_{NN}	t_{BC}	t_{NC}	t_{BN}
2.35	0	0.45	2.1	2.4	2.8
$t_{CC,2}$	$t_{BC,2}$	$t_{NC,2}$	$\triangle_{CC}$	$\triangle_{BB}$	$\triangle_{NN}$
0	0.1	0.3	0.015	2.05	-2.05

Table 4.1.: The proposed TB model parameters for the superlattice. All parameters are expressed in electron volt.

48
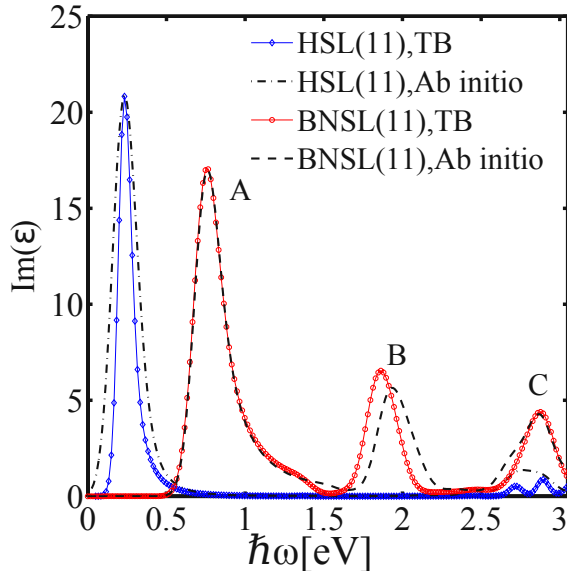
Figure 4.3.: The dielectric response of a HSL(11) and a BNSL(11) based on the TB (solid lines) and first principles calculations (dashed lines). The optical power density is $100 \, \mathrm{kW/cm^2}$ and the photon flux is assumed to be normal to the HSL/BNSL plane.

the instability of the superlattice shown in the right side of Fig. 4.2(c) as a result of the dangling bonds, which will quickly relax to form another geometry. In fact, all superlattices with even values of n_w are unphysical, and thus the studies are restricted to odd values of n_w.

The optical response of the superlattices presented in Fig. 4.1 is studied in terms of the interband dielectric response function (Eq.2.4). The details of dielectric response function is presented in Sec. 2.1.1.

Figure 4.3 compares the imaginary parts of the dielectric functions for a HSL(11) and a BNSL(11). The absorption spectrum exhibits its first peak at $\hbar\omega = 0.33$eV which corresponds to a transition from the highest valence band to the lowest conduction band. The optical absorption spectrum of BNSL(11) exhibits additional peaks in the photon energy range $0 < \hbar\omega < 3.5$eV. The absorption peaks occur at the photon energies of 0.91eV, 1.965eV, and 3.156eV which are related to transitions represented by A, B, and C in Fig. 4.2(b), respectively. The comparison of the dielectric functions in Fig. 4.3 with the bandstructures shown in Figs. 4.2(a) and (b) suggests that for this specific structure only transitions from valence bands to conduction bands with the same index are allowed. This, however, is not a general transition rule for BNSLs and does not hold at various geometrical parameters.

In order to get a deeper understanding on the operation of such structures the local density of states (LDOS) and photocurrent need to be carefully considered. Figures 4.4(a) and 4.4(b) show the LDOS for the superlattices under study. These LDOS plots indicate the presence of localized states in both structures. The normalized LDOS for the unit cell of an ultrathin HSL is shown in Fig. 4.4(c). It is predictable that the first peak in the optical spectrum occurs at $\hbar\omega = 1.5$eV which is related to an optical transition between the two confined states at energies 0.74eV and 0.69eV (See Fig. 4.4(c)). Since the presence of these two states is forbidden in the barrier
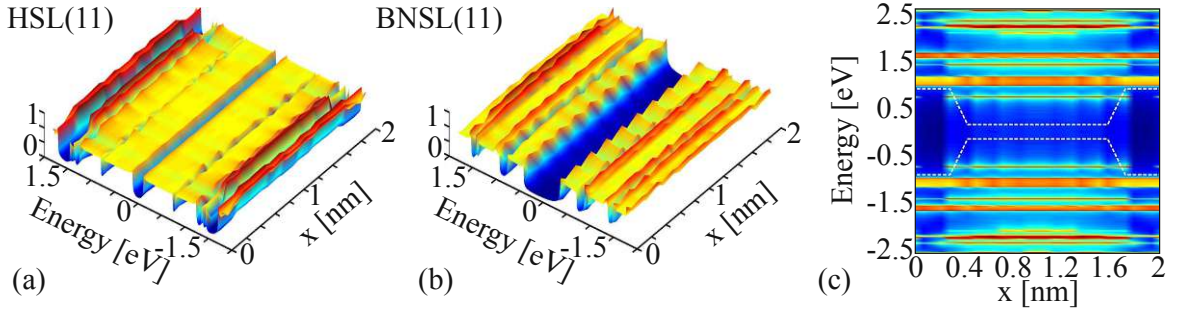
Figure 4.4.: The local density of states for (a) an HSL(11) and (b) a BNSL(11). (c) normalized LDOS for a unit cell of an ultrathin HSL. The optical power density of 10^2 kW/cm^2 and the photon flux normal to the HSL/BNSL plane are assumed.

regions of the superlattice, the photocurrent at $\hbar\omega = 1.5$eV is completely of quantum mechanical nature. At higher energies some continuous minibands are formed which give rise to the photocurrent observed at approximately $\hbar\omega = 2$eV.

In order to assess the performance of superlatice structures for photodetection applications, the quantum efficiency and the photoresponsivity of the presented structures are evaluated. The quantum efficiency is defined as $\alpha = (I_{\mathrm{ph}}/q)\,/\,(P_{\mathrm{op}}/\hbar\omega)$, where I_{ph} and P_{op} are the photocurrent and the incident optical power, respectively. Figure 4.5(a) and (b) shows the calculated photocurrent and quantum efficiency as a function of the incident photon energy, respectively, for HSL(11) and BNSL(11). The quantum efficiency peaks if the photon energy corresponds to an allowed intersubband optical transition. The quantum efficiency of the HSL reaches the values of about 20%, which is significantly larger than that of H-AGNRs [171]. For the case of BNSL(11), there are more peaks in the specified energy range due to the different subband spacings in comparison with that of HSL(11). Quantum efficiencies of 13% and larger than 20% are obtained for the first and second peaks in the optical spectrum, respectively. The photoresponsivities- defined as $I_{\mathrm{ph}}/P_{\mathrm{op}}$- of HSL and BNSL reach 0.866A/W and 0.303A/W, respectively, where the optical power is assumed to be 100 kW/cm^2.

In this study, a small voltage bias in the range of 0.05-0.1V is applied to drive the generated electrons and holes towards the contacts. The restriction for the applied voltage bias is the band to band tunneling which increases the dark current and is detrimental for photodetectors. The tunneling current has an exponential dependence on the electric field. Due to the relatively small length of proposed superlattice photodetectors, applying even a small voltage bias may cause a huge electric field. For example a voltage bias of 0.1V leads to an electric field of 4.7×10^5V/cm.

The structural parameters effects on superlattice photodetector characteristics are examined. Figures 4.6(a) and 4.6(b) indicate that more peaks appear in the quantum efficiencies of HSL/BNSL(13) and HSL/BNSL(17) compared to the main structure (Fig.4.5(b)). If the width of the superlattice increases, energy gaps decrease which
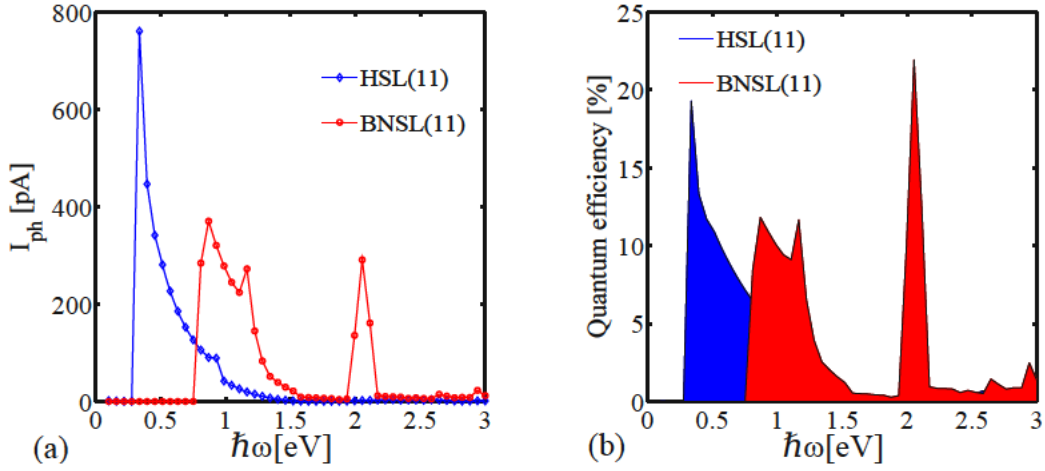
Figure 4.5.: (a) Photocurrent and (b) quantum efficiency for a HSL(11) and a BNSL(11). The optical power density is 100 kW/cm² and the photon flux is assumed to be normal to the HSL/BNSL plane.

allow more optical transitions. This behavior is similar to that of GNRs [179], however, in superlattice photodetectors, the quantum efficiencies at higher energies are larger in comparison with that of lower energies. This is due to the presence of barriers that block transport of photo-generated carriers which is more pronounced by increasing the barrier/well lengths, see Fig. 4.6(c) and Fig. 4.6(d). It should be noted that the confinement due to the presence of barriers only weakly affects devices with relatively long wells and the characteristics of such structures become similar to conventional GNR-photodetectors.

4.2. Line-edge Roughness Effects

Line-edge roughness plays an important role on the characteristics of narrow GNRs. Experimental data show that line-edge roughness is the dominant scattering mechanism for GNRs narrower than 60nm [180]. Line-edge roughness causes fluctuations in the edge potential and leads to the modulation of the energy gaps which affects optical transitions and photon absorption energies. Therefore, a careful investigation of this effect on the optical properties of GNR superlattices is essential. Line-edge roughness is a statistical phenomenon that can be well described by means of an exponential autocorrelation function [179]:

$$R(x) = \Delta W^2 \exp\left(-\frac{|x|}{\Delta L}\right),$$
(4.1)

where ΔL is the roughness correlation length which is a measure of smoothness and ΔW is the root mean square of the fluctuation amplitude. To create line-edge rough-
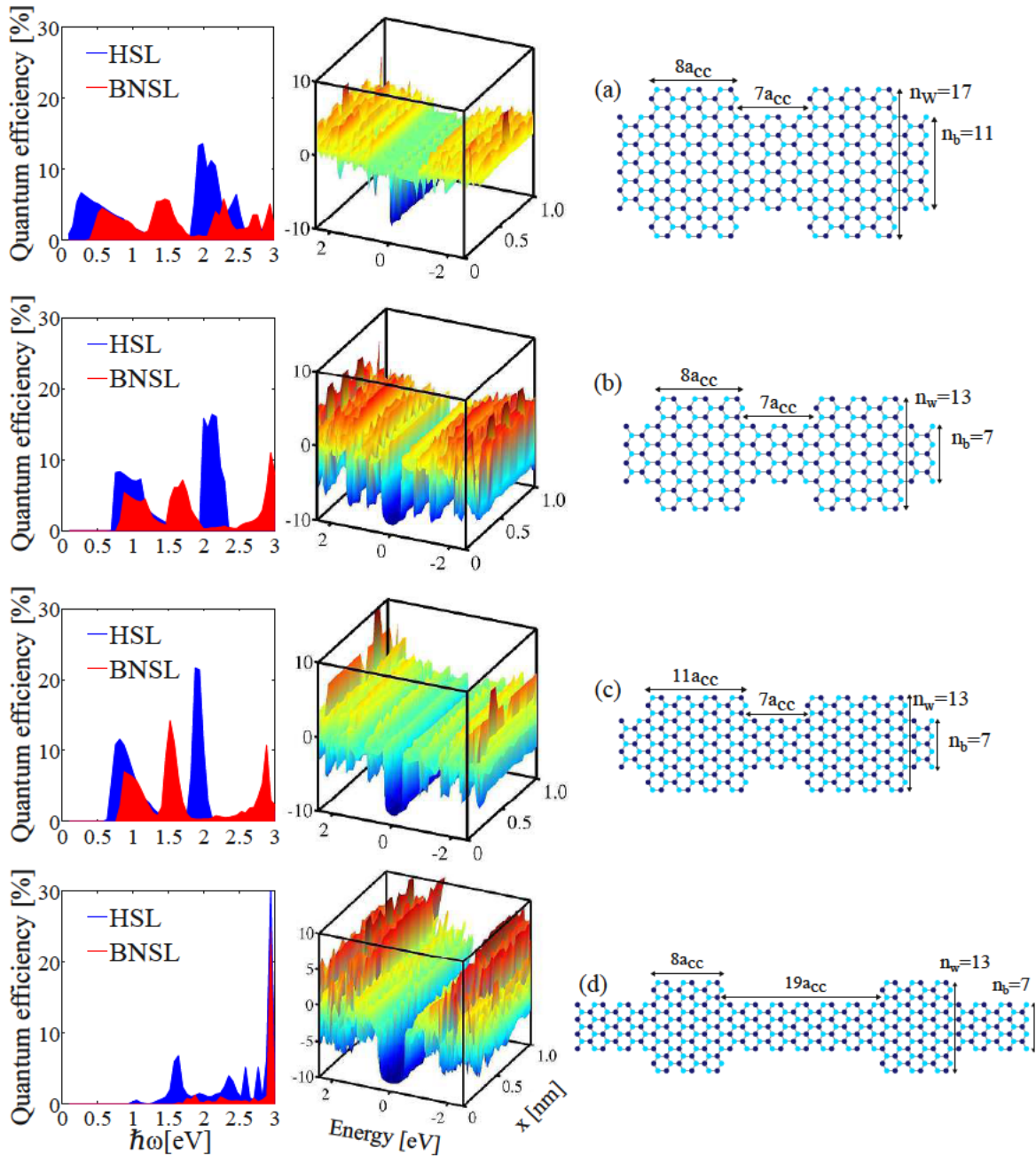
Figure 4.6.: The structure of (a) HSL(13) and (b) HSL(17). (c,d) Superlattices with different well/barrier lengths. The quantum efficiency and local density of states of each structure are depicted.

ness in real space, a random phase is added to the Fourier transform of the auto-correlation function (power spectrum) followed by an inverse Fourier transform [181]. Using the obtained roughness profiles various devices are generated. The optical characteristics of each device is evaluated separately, followed by an ensemble average.
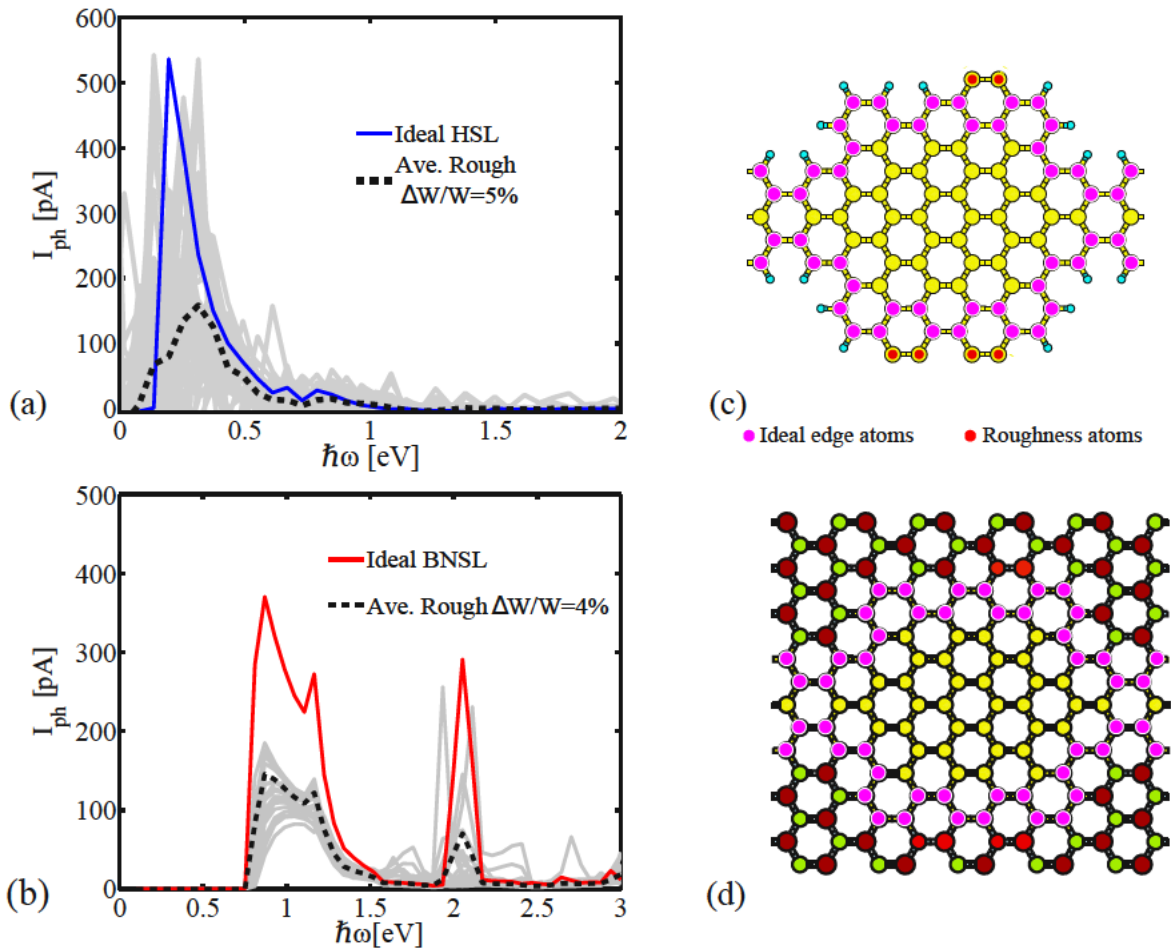
Figure 4.7.: (Dashed-black line) The average photocurrent spectrum over different samples and (gray lines) the photocurrent spectrum of each sample as a function of the incident photon energy.(a,c) HSL and (b,d) BNSL.

The effect of line-edge roughness on the electronic properties of GNRs has been investigated in several analytical [179, 182] and numerical studies [183, 184]. Here, we investigate the role of roughness on the spectrum of photocurrent in GNR-based superlattices.

We add/remove an integer number of atoms from the edges based on their relative position with respect to the generated rough edge. However, this may result in an unstable edge-structures with monomers instead of dimers at the edges. In these cases, the edges are reconstructed to be physically stable. For the given geometrical and roughness parameters many samples are statistically generated. The characteristics of each device is evaluated followed by an ensemble average over all samples, see Fig. 4.7. More details about our approach can be found in [181].

Due to backscattering of carriers, the photocurrent and quantum efficiencies of both supper lattices decrease in the presence of line-edge roughness. Figure 4.7 shows that
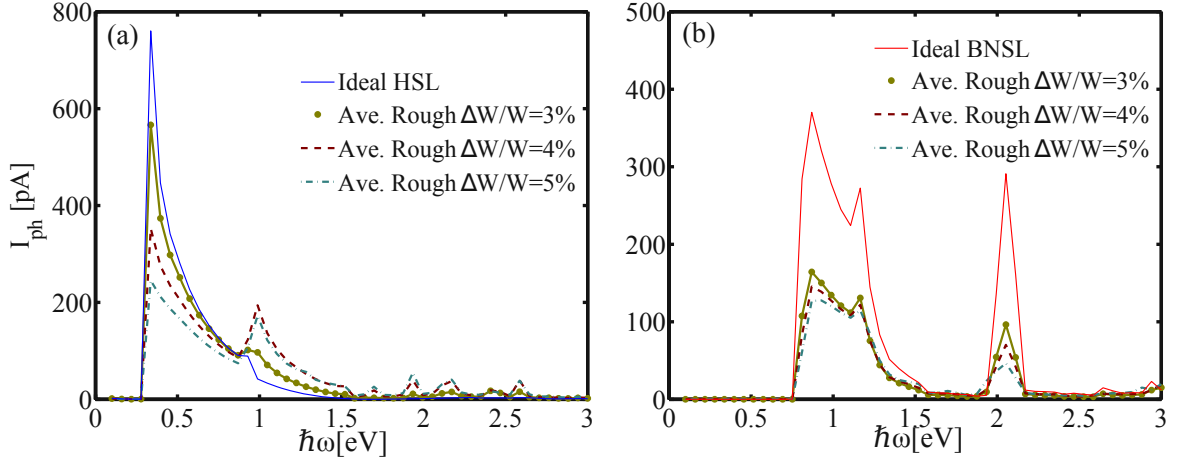
Figure 4.8.: The ideal and average photocurrent spectra for (a) HSL(11) and (b) BNSL(11) at various roughness amplitudes.

due to effective width variation, the photoabsorption peaks appear at energies larger or smaller than the peaks of the structure without disorder. The average width of edge-defected devices, however, is equal to that of a device with perfect edges. Therefore, line-edge roughness does not affect the location of the average photocurrent peak.

Figure 4.8 exhibits the results for HSL(11) and BNSL(11) with edge disorders. Roughness is expressed in terms of n_w because the well has a more significant effect on the optical transitions. The absolute roughness amplitude is the same all over the device. In the case of BNSL(11), the roughness is applied at the C-BN interfaces. As it is shown in Fig. 4.1, a BN passivation with 2/3 dimers is considered in BNSLs. For the roughness amplitudes of 3%, 4%, and 5%, the structures are still passivated with BN. However, for larger roughness amplitudes the roughness may cross the boundaries without any BN passivation. In these cases, the structures are reconstructed by additional BN dimmers at the boundaries.

HSL(11) exhibits photoresponsivity and quantum efficiency reductions of 23%, 55%, and 70% for the relative roughness amplitudes of 3%, 4%, and 5%, respectively, whereas a smoother behavior is observed for BNSL(11) (compare Fig. 4.8(a) and (b)). This behavior is attributed to the stable configuration of edge-carbon atoms in BNSL in comparison with HSL in the presence of line-edge roughness. The average photocurrent of edge-defected HSLs peaks at photon energies around $\hbar\omega = 1\text{eV}$. This peak is related to line-edge roughness induced states, see Fig. 4.9. Due to the formation of dangling bonds in the presence of line-edge roughness, these states are formed. As the relative roughness amplitude increases more states are induced and more photocurrent is generated by transitions from these states. However, dangling bonds are absent in edge-defected BNSLs and such states do not appear in such structures.
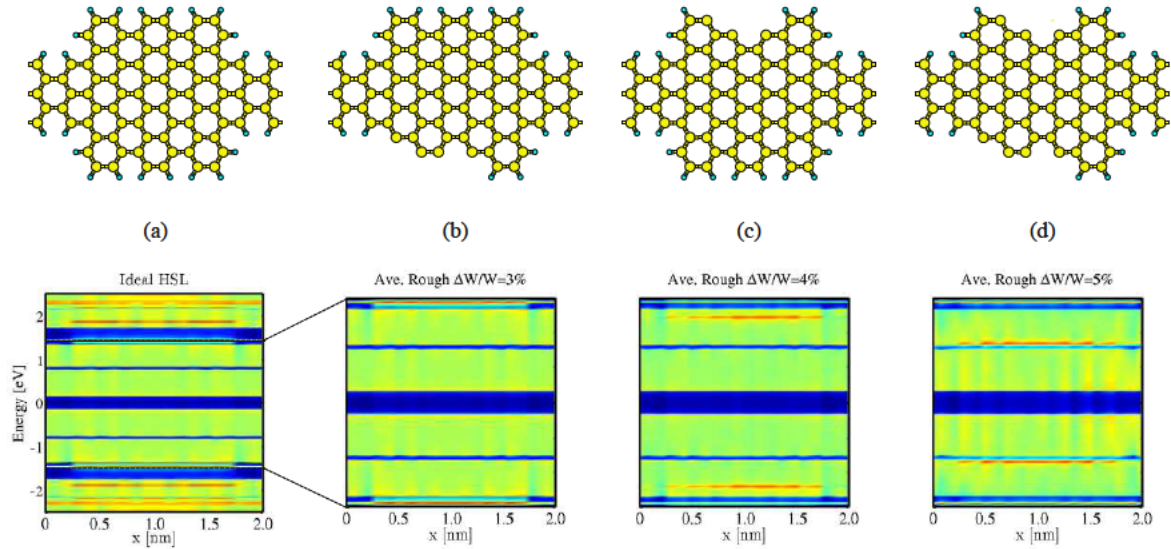
Figure 4.9.: Local density of states for (a) an ideal and (b,c,d) rough HSL(11) at various roughness amplitudes. The optical power density is 100 kW/cm^2 and the photon flux is assumed to be normal to the HSL/BNSL plane.

4.3. Conclusions

The optical properties of graphene nanoribbon superlattices embedded in boron nitride sheets and the possibility of using such structures as photodetectors are studied. We propose a set of tight-binding parameters for the investigated structures which shows excellent agreement with first-principles results. The results indicate that the optical spectrum of a BN-confined AGNR superlattice contains more absorption peaks and show more optical intersubband transitions compared to a hydrogen passivated superlattice with the same geometry. Employing the non-equilibrium Green's function method, the photocurrents and quantum efficiencies are evaluated and compared for both devices at various incident photon energies.

Using an statistical approach the role of line-edge roughness on the optical properties of GNR-based superlattices is investigated. The results indicate that the quantum efficiency and photoresponsivity decrease in the presence of line-edge roughness. For HSL, induced states appear and increase with the roughness amplitude which result in the appearance of an additional peak in photocurrent spectrum. In comparison with HSLs, BNSL photodetectors exhibit more robust optical properties in the presence of line- edge roughness due to stable edge atom configuration.

5. Quantum Cascade Lasers

Quantum cascade lasers (QCLs) are the most prominent and compact coherent light sources in the wavelength range from 3.5 to 20 μm. Remarkable design degrees of freedom make QCLs a unique candidate to serve as a semiconductor source of ultra-short pulses in the mid-infrared (MIR) and terahertz (THz) regions [123, 185, 186]. Ultrashort pulses which are generated in QCL media have been employed for various applications, such as non-linear frequency conversion [187, 188], high-speed free space communication [189], and trace gas detection [190].

A common technique for generation of ultrashort pulses is mode locking which is realized either by an internal mechanism (passive mode locking) or an external one (active mode locking) [191]. Active modelocking does not lead to ultrashort pulses, because the frequency of modulation cannot be raised arbitrarily while a passive saturable absorber is much more effective in ultrashort pulse generation [128]. In lasers with a relatively long gain recovery time compared to the cavity round-trip time, the instability caused by a saturable absorber (SA) can often lead to passive mode locking [128]. Because of ultra-fast tunneling and inter-subband transitions, QCLs, unlike conventional semiconductor lasers, have a gain recovery (in the order of picoseconds) faster than the cavity round trip time. Therefore, SA dominated self-mode locking seems impossible in typical QCLs. However, as reported in Ref. [125], under these conditions the elusive Risken-Nummedal-Graham-Haken (RNGH)-like instability can be observed in QCLs. It is demonstrated that fast gain recovery of QCLs exhibits two kinds of instabilities in the multi-mode regime: the RNGH-like instability and one associated with spatial hole burning (SHB) [126].

The active mode locking in QCLs is strongly limited by SHB which leads to a proliferation of modes with random phases and destroys coherence [191].

In this chapter we investigate performance optimization and passive mode locking caused by a saturable absorber in a ring cavity QCL in which the SHB instability does not occur because of the absence of standing waves. Performance optimization of QCLs has achieved significant progress in recent years [104, 192, 193]. The performance of QCLs can be improved by optimizing the epitaxial growth, fabrication process, and active region design [194–196]. The latter is important in order to insure efficient carrier injection in the upper lasing state and carrier extraction out of the lower lasing state [104].

So far, optimization techniques proposed to design QCL structures are based on genetic algorithms [104, 192, 197, 198]. A multi-variable multi-objective optimization algorithm

for terahertz QCLs is presented in [193]. In [104, 192], a technique to design quantum cascade structures in the mid-infrared is proposed. Particle swarm optimization (PSO) [199] is as an alternative to traditional evolutionary algorithms. It attempts to mimic the goal-seeking behavior of biological swarms. In PSO, a possible solution of the optimization problem is represented as a particle, and the algorithm operates in an iterative manner. Unlike traditional evolutionary algorithms, particles in PSO do not perform the operation of genetic recombination between particles, but they work individually with social behavior in swarms. PSO has some attractive characteristics. In particular, it has memories, so that knowledge of good solutions can be retained by all particles (solutions). This method has been successfully used to solve many discontinuous and complex problems with good results [200, 201].

We perform an optimization study of ring cavity QCLs considering the laser instability condition. Laser design parameters, including the barrier and well thicknesses and applied electric field, are modified for maximizing laser gain under a desired instability condition. Passive mode locking with saturable absorber is investigated for the optimized QCLs. The effects of saturable absorber and pumping strength on the instability characteristics are studied. A large optical gain below the instability threshold is achieved for optimized QCL designs. A numerical calculation based on the Maxwell-Bloch equations is performed to analyze the optimized structure.

5.1. Models

Because of the large number of involved design parameters, performance improvement of QCLs requires a systematic multi-objective optimizer in conjunction with a simulation tool which has a good balance between computational speed and physical accuracy.

Various approaches such as rate equations [202, 203], Monte-Carlo simulations [204], density matrix methods [205], and the non-equilibrium Green's function formalism (NEGF) [206, 207] have been developed for the simulation of QCLs.

The simplest models, based entirely on scattering and neglecting coherence effects, require a fewer number of material parameters and are generally able to predict the threshold current density but not the light-current or current-voltage characteristics [208]. Pure quantum mechanical models based on NEGF or the density matrix have been used as rigorous approaches to capture the QCL physics. The NEGF theory takes into account incoherent scattering with phonons, impurities, and rough interfaces as well as electron-electron scattering in the Hartree approximation [206]. Unfortunately, the inherently high computational costs of the full quantum mechanical models render them unfeasible for optimization purposes [206].

To study electronic transport in QCL, we employ the Pauli-master equation solved by the Monte-Carlo method [209]. In this semi-classical approach, the transport is modeled via scattering between energy states, including acoustic and optical deformation potential and polar optical electron-phonon scattering as well as alloy, inter-valley, and interface roughness scattering. Accurate results along with a relatively low computational cost render this approach as a good candidate for optimization studies.

5.1.1. Pauli-Master Equation

Although quantum cascade structures (QCSs) have a long history, many aspects of the carrier transport and interaction with light field are still unclear. Very important question concerning physics of the QCSs is whether transport is coherent or incoherent. There were many discussions about the problem, and several attempts to estimate the kind of transport were successful, especially [210, 211]. The answer on this question depends on conditions of QCSs operation. For example, the coherent electron transport is of interest in the non-equilibrium regime at femtosecond and picosecond time intervals. The incoherent transport is prevalent at the high excitation level in the stationary quasi-equilibrium regime. In both cases, the electronic transport influences the optical properties of the device. In this connection, the development of the theory for coherent and incoherent electron transport regimes, included many-body effects and light-matter interactions in QCS, is of actual interest. We employed the Pauli master equation [212] to model current transport through the QCL semiconductor heterostructure. Based on the experiences of a MATLAB prototype presented in [204], an optimized Monte Carlo (MC) simulator has been implemented in C++ within the Vienna-Schrödinger-Poisson (VSP) simulation framework [213, 214].

In many practical cases the steady state transport in QCLs is incoherent such that a semiclassical description can be employed [210, 215]. Following this approach, a transport simulator for quantum cascade lasers based on the Pauli master equation [204] has been developed. The transport is described via scattering transitions among quasistationary basis states which are determined by numerically solving the Schrödinger equation. The Hamiltonian includes the band edge formed by the heterostructure. In this way, tunneling is accounted for through the delocalized eigenstates. The transport equations are derived from the Liouville von Neumann equation in the Markov limit in combination with the diagonal approximation. This means that the off-diagonal elements of the density matrix are neglected and one arrives at the Boltzmann-like Pauli master equation [216]

$$\frac{\mathrm{d}f_{k,n}(t)}{\mathrm{d}t} = \sum_{k',m}\{S_m^n(\mathbf{k}',\mathbf{k})f_{k,n}(t) - S_n^m(\mathbf{k},\mathbf{k}')f_{k,n}(t)\}. \tag{5.1}$$

Here, m and n denote the subband indices, and $\mathbf{k}$ and $\mathbf{k}'$ the in-plane wave vectors. The transition rate from state $|\mathbf{k}',m\rangle$ to state $|\mathbf{k},n\rangle$ for an interaction H_{int} follows

from Fermi's golden rule

$$S_n^m(\mathbf{k}, \mathbf{k}') = \frac{2\pi}{\hbar}|\langle \mathbf{k}', m|H_{\text{int}}|\mathbf{k}, n\rangle|^2 \delta(\varepsilon(\mathbf{k}') - \varepsilon(\mathbf{k}) \mp \hbar\omega) \tag{5.2}$$

The simulator makes use of the translational invariance of the QCL structure and simulate the electron transport over a single stage only [217]. The wave function overlap between the central stage and spatially remote stages is small. It is therefore assumed that interstage scattering is limited only to the nearest neighbor stages and that interactions between basis states of remote stages can be safely neglected. The states of the whole QCL device structure are assumed to be a periodic repetition of the states of a central stage. This approach ensures charge conservation and allows imposing periodic boundary conditions on the Pauli master equation. Since transport is simulated over a central stage only, every time a carrier undergoes an interstage scattering process the electron is reinjected into the central stage with an energy changed by the voltage drop over a single period. The total current is determined by the net number of interstage transitions. The transport equations is solved using a Monte Carlo approach. Several new numerical methods are employed to reduce the computational cost of the simulation [209].

5.1.2. Particle Swarm Optimization

The PSO is an iterative method which initializes a number of vectors (called particles) randomly within the search space of the objective function. The set of particles is known as the swarm. Each particle represents a potential solution to the problem expressed by the objective function. During each time step the objective function is evaluated to establish the fitness of each particle using its position as input. Fitness values are used to determine which positions in the search space are better than others. Particles are then made to *fly* through the search space being attracted to both their personal best position as well as the best position found by the swarm so far [218]. The particles are *flown* through the search space by updating the position of the ith particle at time step k according to the following equation [218]:

$$\mathbf{x}_i^{k+1} = \mathbf{x}_i^k + \mathbf{v}_i^k, \tag{5.3}$$

where $\mathbf{x}_i^k$ and $\mathbf{v}_i^k$ are vectors representing the current position and velocity, respectively. Assuming vectors of dimension, the updates of the jth velocity component is governed by the following equation [219]

$$\begin{aligned} v_{i,j}^{k+1} = \omega v_{i,j}^k + \\ c_1 r_{1,j}(y_{i,j} - x_{i,j}^k) + c_2 r_{2,j}(\hat{y}_j - x_{i,j}^k), j = 1, 2, ..., n \end{aligned} \tag{5.4}$$

where $0 < \omega < 1$ is an inertia weight determining how much of the particle's previous velocity is preserved, c_1 and c_2 are two positive acceleration constants, $r_{1,j}$ and $r_{2,j}$ are two uniform random sequences sampled from $U(0, l)$, y_i is the personal best position found by the ith particle and $\hat{y}$ is the best position found by the entire swarm so far. The following relation should hold in order for the PSO to converge [218]:

$$\frac{c_1 + c_2}{2} - 1 < \omega. \tag{5.5}$$

However, the standard PSO is not guaranteed to converge on a local extremum, but most of the recent PSO algorithms converge to the global optimum.

Employing a Pauli master equation-based description of electronic transport in QCLs along with the multi-objective PSO strategy, a framework is developed for maximizing laser gain with simultaneous desirable instability operation. In this framework one starts from a reference design. In the next iterations the well and barrier thicknesses and the applied electric field are modified until maximum gain and laser operation below the instability threshold are achieved. The analytical linear stability model introduced in Ref. [126] is employed to analyze the instability threshold of the studied QCL. In this model, the criteria for the RNGH instability is expressed in terms of the parametric gain $g(\Omega)$ as a function of the resonance frequency Ω

$$\begin{aligned} g(\Omega) = -\frac{c}{2n}\text{Re}\Bigg[&l_0 \frac{(\Omega T_1 + i)\Omega T_2 - 2(p_f - 1)}{(\Omega T_1 + i)(\Omega T_2 + i) - (p_f - 1)} + \\ &\frac{\gamma \hbar^2 (p_f - 1)}{\mu^2 T_1 T_2} \frac{(\Omega T_1 + i)(3\Omega T_2 + 2i) - 4(p_f - 1)}{(\Omega T_1 + i)(\Omega T_2 + i) - (p_f - 1)} \Bigg], \end{aligned} \tag{5.6}$$

where p_f is the pumping factor, T_1 is the gain recovery time, T_2 is the dephasing time, l_0 is the linear cavity loss, μ is the matrix element of the lasing transition, and γ is the SA coefficient. The derivation of Eq.5.6 is presented in detail in Appendix C. Based on this analysis, each mode which is identified by the resonance frequency Ω, is stable if the parametric gain is negative, otherwise it is unstable. At each iteration of the optimization loop, for a set of geometrical parameters and the applied electric field, the parameters T_1 and μ are extracted and the parametric gain (Eq. 5.6) is evaluated. The parameter T_2, dephasing time, can be approximated by $T_1/10$ as mentioned in [220]. If the stability condition is not satisfied, a new set of parameters is selected for the next iteration. The flow chart of the developed framework is described in Fig. 5.1.

5.2. Performance Optimization

We consider the laser gain as a figure of merit and define the instability criterion to satisfy stability conditions. Using the scattering times and calculating the dipole
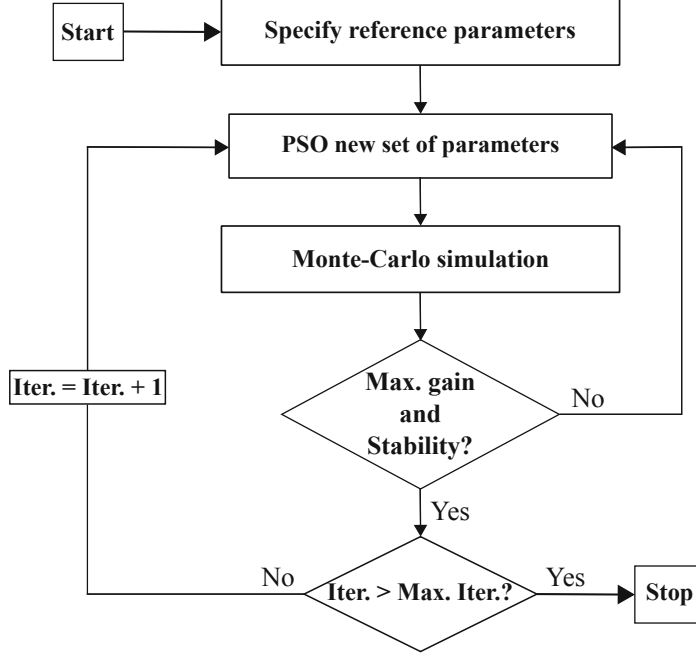
Figure 5.1.: The algorithm of the developed optimization framework.

matrix elements, the gain coefficient g can be estimated for each structure as [108]:

$$g = \tau_3 \left(1 - \frac{\tau_2}{\tau_{32}}\right) \frac{4\pi \ e \ \mu^2}{\lambda_0 \epsilon_0 n_{\text{eff}} L_{\text{p}}} \frac{1}{2\gamma_{32}},$$

(5.7)

where λ_0 is the wavelength in vacuum, ϵ_0 the vacuum dielectric constant, e the elementary charge, n_{eff} the effective refractive index of the mode, L_{p} the length of one period including active region and injector, and $2\gamma_{32}$ is the full width at half maximum value of the luminescence spectrum.

5.2.1. Optimization of a Three-Well Vertical Design

In fact, the optimization framework changes the geometrical parameters which affect the lifetimes and matrix elements. Simulation results indicate that the two key parameters to be optimized are the matrix element μ and the upper laser level lifetime τ_3 ($\approx T_1$ in Eq. 5.6). The gain coefficient increases with these two parameters (see Eq. 5.7). The reference design has a 3QW vertical active-region. The parameters of the reference design are mentioned in [221]. The layer sequence of the $\text{In}_{0.52}\text{Al}_{0.48}\text{As}/\text{In}_{0.53}\text{Ga}_{0.47}\text{As}$ heterostructure for the optimized design, starting with the injection barrier is: **3.74**/2.36/**1.50**/7.45/**1.63**/5.63/**2.15**/4.43/**3.86**/**3.85**/ 3.15/**3.18**/4.40/**2.79**/2.67/**2.46** nm, where the barrier layers are in bold and underlined layers are n-doped with Si at $2 \times 10^{17}\text{cm}^{-3}$.
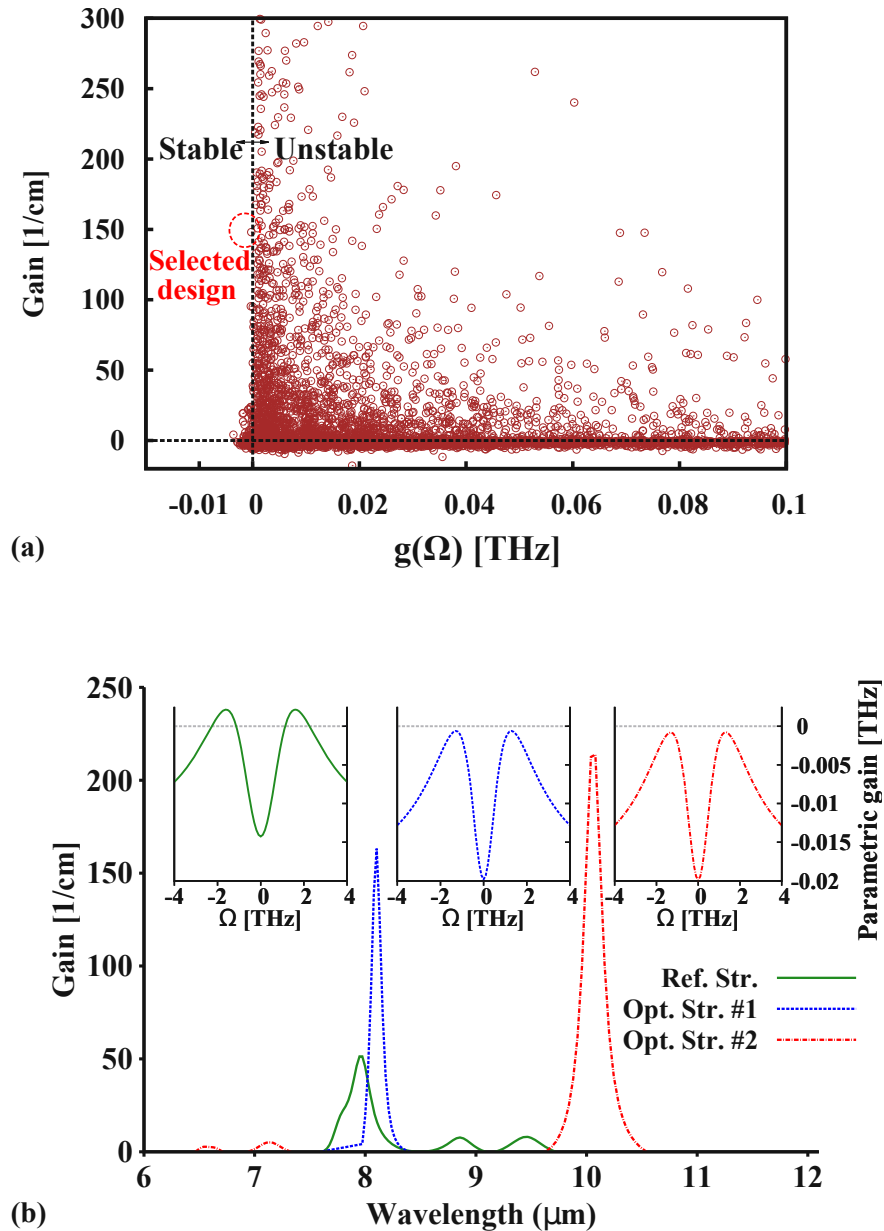
Figure 5.2.: (a) The PSO results for different particles in the search space and (b) gain spectra and instability thresholds for the reference and optimized structures.

Figure 5.2(a) shows the PSO results for different particles in the search space. Most of the points (samples) are located at the right-side of the vertical dashed-line which represents unstable laser operation. The samples at the left-side of the vertical dashed-line and above the horizontal dashed-line are the ones we are looking for.

The instability threshold behavior and gain spectrum for the reference design and two obtained optimized designs are exhibited in Fig. 5.2(b). The first structure is optimized
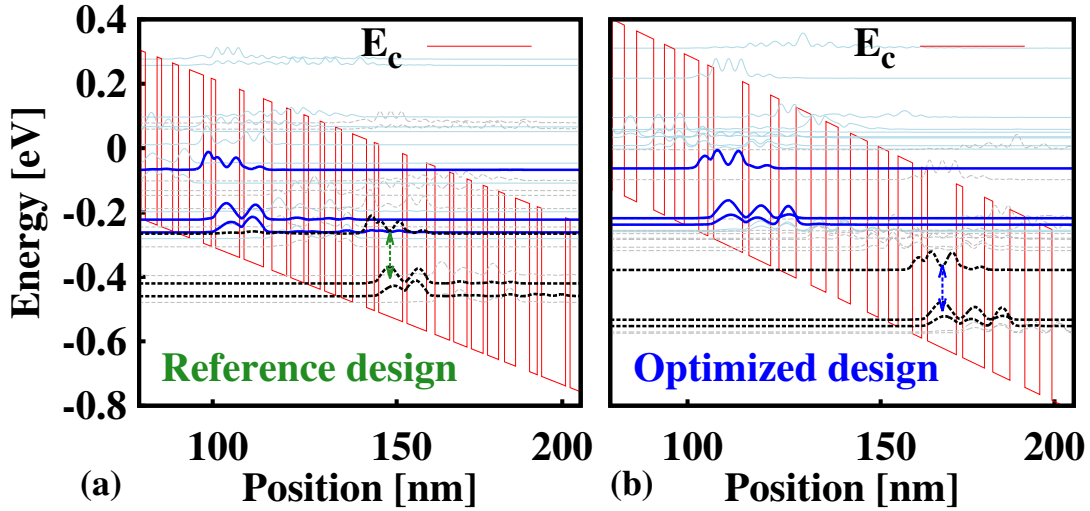
Figure 5.3.: The conduction band diagram and the wavefunctions of (a) the reference design and (b) the optimized structure. The lasing subbands are indicated with bold solid/bold dashed lines.

at the same wavelength as the reference design and the second one is optimized at a higher wavelength but with a larger gain. Our developed framework has the advantage of optimizing the reference structure for a specific wavelength. We focus on the first optimized structure which has the same wavelength as the reference structure.

The conduction band diagram and the associated wave-functions of the reference design and optimized structure are shown in Fig. 5.3. The active region of the optimized structure is a three-well (3QW) vertical-transition design which provides high optical gain and concomitant robustness for laser action, see Fig. 5.3(b). The upper laser level for the optimized structure is delocalized which results in an increase of the upper laser level lifetime τ_3 and consequently the laser gain, see Eq. 5.7. The parameters extracted for the instability analysis of the optimized structure are shown in Table 5.1. Fig. 5.4(a) indicates that the instability threshold decreases uniformly with the SA coefficient, for example $\gamma \geq 3$ m/V^2 triggers the instability for the optimized structure at a relatively low pumping strength ($p_f = 2$). As reported in [126], a saturable

T_1	Gain recovery time	0.46ps
T_2	Dephasing time	0.06 ps
μ	Matrix element of lasing transition	2.44×10^{-9} m
n	Refractive index	3.25
l_0	Linear cavity loss	500 m^{-1}
L	Cavity length	6×10^{-3} m
γ	Saturable absorber coefficient	10^{-11}m/V^2

Table 5.1.: The parameters used for the instability analysis of the optimized structure.

Figure 5.4.: The parametric gain $g(\Omega)$ as a function of the resonance frequency Ω at various (a) SA coefficients and (b) pumping strengths.

absorber always favours a multimode regime to a single mode one, which explains why the instability threshold decreases with γ in the optimized design. As discussed later, this instability results in Rabi sidebands around the cw lasing frequency.

The parametric gain of the optimized structure at various pumping strengths is shown in Fig. 5.4(b). A larger pumping strength broadens the instability characteristics and decreases the instability threshold. The results are consistent with previous works [126].

5.2.2. Optimization of a Superlattice Design

Next, we present the optimization results for a reference QCL with a superlattice (SL) active-region [105]. The layer sequence of the SL structure, starting with the injection barrier, is as follows: **4.0**/1.9/**0.7**/5.8/**0.9**/ 5.7/**0.9**/5/**2.2**/3.4/**1.4**/3.3/ **1.3**/3.2/**1.5**/ 3.1/ **1.9**/3.0/ **2.3**/2.9/**2.5**/2.9 nm. The In$_{0.52}$Al$_{0.48}$As barrier layers are in bold and In$_{0.53}$Ga$_{0.47}$As well layers are in roman. The underlined layers are n-doped with Si at 4×10^{17}cm^{-3}.

The instability characteristics for the 3QW and SL active-regions are compared in Fig. 5.5(a). Because of the larger matrix element (μ) and longer upper laser state lifetime (τ_3), which is approximately equal to the gain recovery time (T_1), the SL active-region QCL indicates more stable operation and higher instability threshold, see Fig. 5.5(a). However, as we mentioned earlier, the matrix element and lifetimes of the lasing transition, which are the key parameters in linear stability analysis, are proportional to optical gain (see Eq. 5.7). As indicated in the inset of Fig. 5.5(b), the 3QW QCL exhibits larger optical gain at nearly the same wavelength. The optical gain
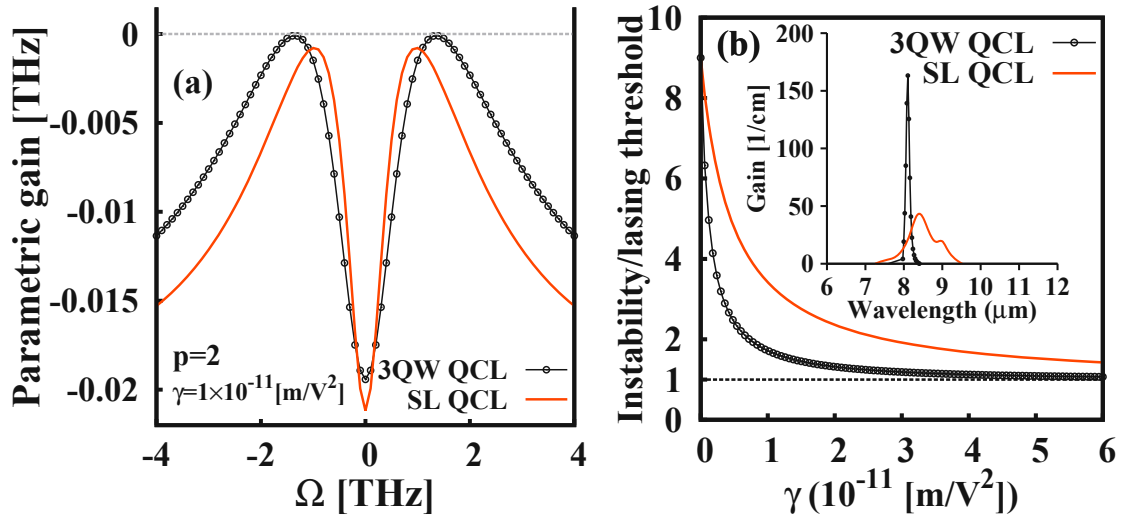
Figure 5.5.: (a) The parametric gain $g(\Omega)$ as a function of the resonance frequency Ω. (b) The pumping ratio p_f at which the RNGH instability sets in as a function of the SA coefficient. Inset: Optical gain spectra obtained for two optimized active-region QCLs.

of the 3QW structure is maximized by delocalizing the lasing states which increases the lifetimes τ_3 and τ_2. Because of the bound states in the SL active-region, there is no significant lifetime variation, however, due to the larger matrix element, a better instability condition is achieved.

5.2.3. Optimization of a THz Design

Terahertz frequencies (1-10 THz, 30-300 μm) are among the least developed electromagnetic spectra even though they have wide ranging applications in spectroscopy, imaging, and remote sensing [222]. Since the report of quantum cascade lasers (QCLs) operating in the terahertz spectral region by Köhler et al. [99] there has been significant progress concerning the available frequencies, the temperature performance, and the understanding of the dynamics [223].

Emitting radiation due to intersubband optical transitions in QCLs makes this possibility to generate terahertz radiation in these lasers. The terahertz radiation in QCLs could be engineered by electronic bandstructure. We select the designs that utilize strong electron-phonon interaction in the semiconductor as a means to establish population inversion for optical gain [2]. Based on the algorithm introduced in Sec. 5.1.2, we study the SA and pumping factor effects on instability characteristics of terahertz QCLs.

Here, a reference QCL operating at 3.44 THz, corresponding to $\lambda = 87.2$ μm, is employed [4]. The layer sequence of the reference structure, starting with the injection
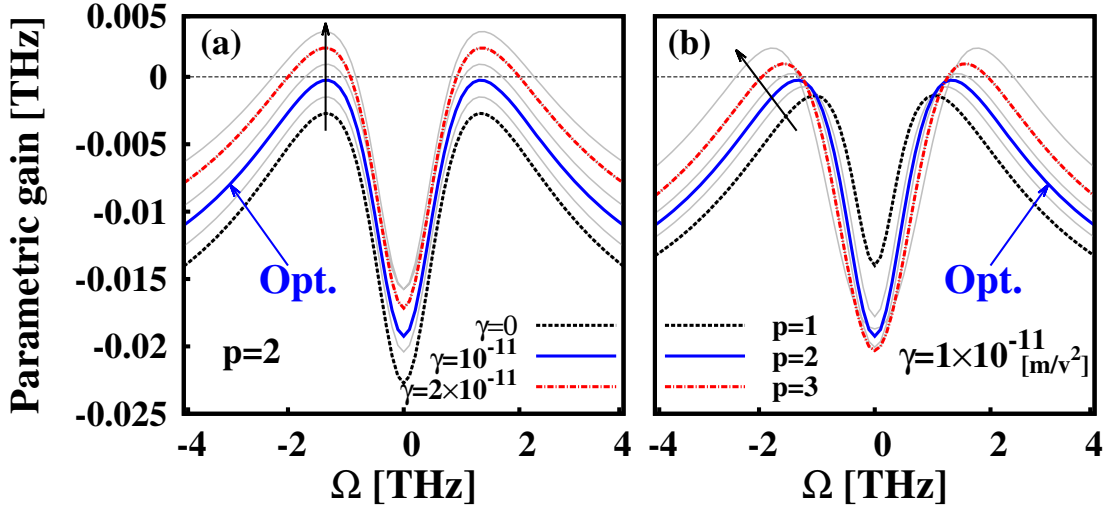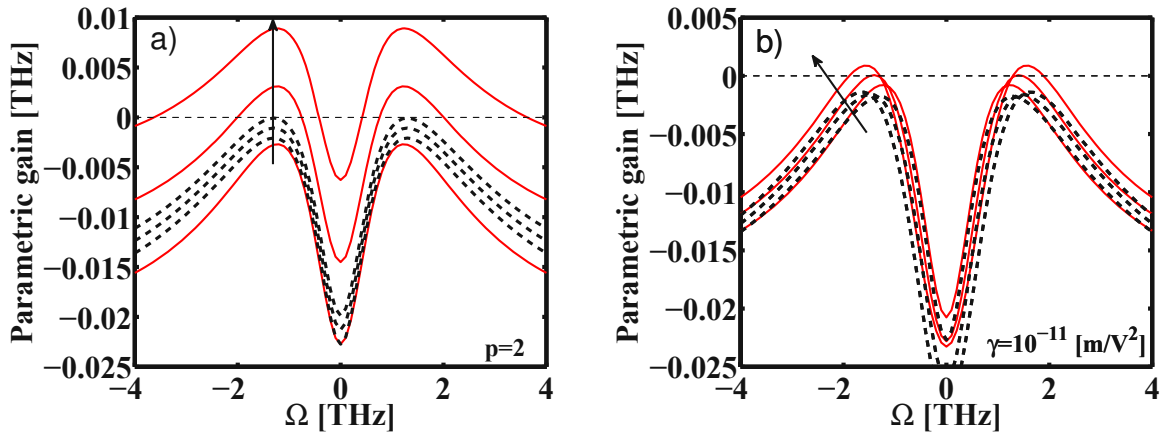
Figure 5.6.: The parametric gain $g(\Omega)$ as a function of the resonance frequency Ω at various (a) SA coefficients (γ =0,3, and 6 m/V^2) and (b) pumping strengths $(2, 2.4, 2.8)$ for a mid infrared QCL (solid red line) and a terahertz QCL (dashed black line).

barrier, is as follows: 5.4/7.8/2.4/6.43.8/14.8/2.4/9.4 nm. The 14.8 nm well is doped at 1.9×10^{16}cm^{-3}. The operating temperature for reference design is 5 K up to 65 K, however, higher operating temperatures are achieved for optimized THz QCLs.

Figure 5.6 exhibits instability characteristics for two QCLs operating in infrared and terahertz spectral region. Figure 5.6(a) indicates that the instability threshold decreases faster with SA coefficient for mid infrared QCL sample while the terahertz QCL sample still operates below the instability threshold. SA can bring $g(\Omega)$ above zero, thereby triggering an instability which is more effective for mid infrared QCL. The parametric gain of the optimized structure at various pumping strengths is shown in Fig. 5.6(b). A larger pumping strength broadens the instability characteristics and decreases the instability threshold which is significant for mid infrared QCL. The results indicate more stability for QCLs operating in the terahertz spectral region.

5.3. Dynamics of QCLs

The linear stability analysis, however, predicts only the instability threshold and does not describe the dynamics of the laser. To investigate the dynamics of QCLs above the instability threshold, the Maxwell-Bloch equations are solved numerically. The effect of the SA is modeled as the intensity-modulated optical field amplitude in the
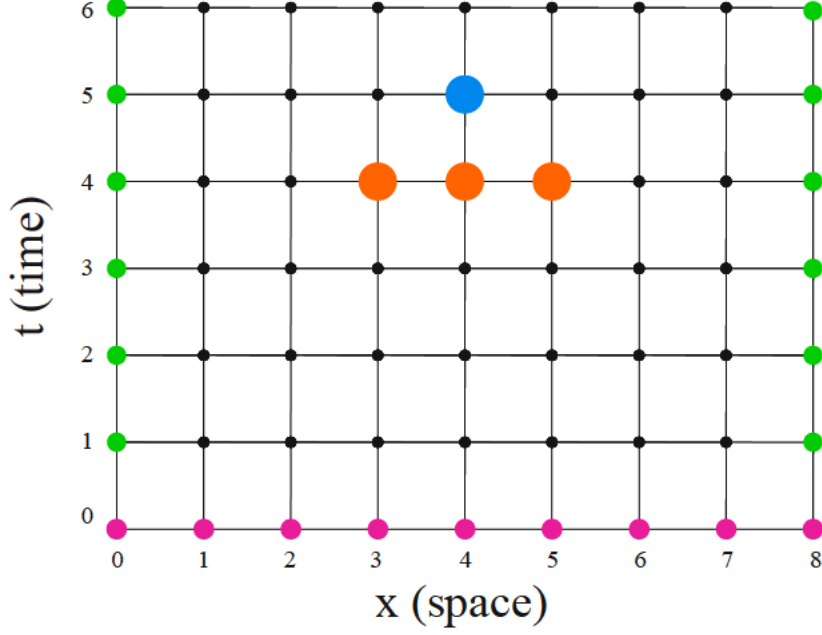
Figure 5.7.: The $m \times n$ mesh points for the finite difference approximation. Here $m = 8$ and $n = 6$. The boundary conditions are shown by green dots and initial condition by pink dots. $E(m, n+1)$, a sample step in time domain, is shown with blue dot and its value is dependent on the previous steps, the orange dots.

standard Maxwell-Bloch equations [128]:

$$\partial_t E = -\frac{c}{n}\partial_z E - \frac{c}{n}\frac{i\mu P}{\hbar l_0 D_{\text{th}}} - \frac{c}{2n}(l_0 - \bar{\gamma}|E|^2)E,$$

$$\partial_t P = \frac{i\mu}{2\hbar}DE - \frac{P}{T_2}, \tag{5.8}$$

$$\partial_t D = \frac{D_{\text{p}} - D}{T_1} + \frac{i\mu}{\hbar}(E^*P - c.c.).$$

E and P are the envelopes of the normalized electric field and polarization, respectively, D represents the normalized average population inversion, D_{p} is the normalized steady-state population inversion, D_{th} is the lasing threshold value of D_{p} for $\gamma = 0$, proportional to the pumping factor p_f ($p_f \geq 1$), l_0 is the linear cavity loss, and $\bar{\gamma} = \hbar^2\gamma/\mu^2$.

We employ a finite-difference discretization scheme to find the evolution of electric field, polarization, and population inversion in the spatial and time domain. A periodic boundary condition is applied to model a ring cavity. The equations are discretized to calculate the state of the system in each step from the state in the previous step. This procedure is shown in Fig. 5.7.

The number of mesh points play an important role in preventing unreasonable results

67

and achieving consistency. The number should be large enough to make sure there is not any un-inspected variation. The $x - t$ plane is divided into a $m \times n$ mesh points as shown in Fig. 5.7. The number of mesh points are $m = 500$ and $n = 10^5$ which correspond to the grid sizes of $\Delta x = L/m = 12 \ \mu$m and $\Delta t = \Delta x/c = 120$ fs. The periodic boundary conditions for the dynamical variables of the QCL (electric field E, polarization P, and population inversion D) are $E(0, n) = E(L, n)$, $P(0, n) = P(L, n)$, and $D(0, n) = D(L, n)$.

The derivatives of variables in time and space are achieved by Taylor expansion about the grid point (m, n).

$$\partial_t E(m, n) = -\frac{E(m, n + 1) - E(m, n)}{\Delta t} - \frac{1}{2}\Delta t \frac{\partial^2 E(m, n)}{\partial t^2} \tag{5.9}$$

$$\partial_z E(m, n) = -\frac{E(m, n) - E(m, n - 1)}{\Delta z} + \frac{1}{2}\Delta x \frac{\partial^2 E(m, n)}{\partial z^2} \tag{5.10}$$

Similar expressions are written for $\partial_t P$ and $\partial_t D$. Starting with the left hand-side of Eq. 5.9 and 5.10 for the electric field, we have

$$
\begin{aligned}
\dot{E} + c\frac{\partial E}{\partial z} = &-\frac{E(m, n + 1) - E(m, n)}{\Delta t} - \frac{1}{2}\Delta t \frac{\partial^2 E(m, n)}{\partial t^2} \\
&- \frac{E(m, n) - E(m, n - 1)}{\Delta z} + \frac{1}{2}c^2\Delta t^2 \frac{\partial^2 E(m, n)}{\partial z^2} = \\
&\frac{E(m, n + 1) - E(m - 1, n)}{\Delta t} + \frac{1}{2}\Delta t \left[c^2 \frac{\partial E(m, n)}{\partial z^2} - \frac{\partial E(m, n)}{\partial t^2} \right] \\
&= k(P - E).
\end{aligned} \tag{5.11}
$$

The expression $\dot{E}$ denotes $\partial_t E$. Selecting the second equality helps to eliminate the terms with first derivative

$$k(P - E) = \frac{E(m, n + 1) - E(m - 1, n)}{\Delta t} + \frac{1}{2}\Delta t \left[c^2 \frac{\partial^2 E(m, n)}{\partial x^2} - \frac{\partial^2 E(m, n)}{\partial t^2} \right] \tag{5.12}$$

Solving Eq.5.12 for $E(m, n + 1)$ gives

$$
\begin{aligned}
E(m, n + 1) = &k\Delta t(P - E) \\
&+ \frac{1}{2}\Delta t^2 \left[\frac{\partial^2 E(m, n)}{\partial t^2} - c^2 \frac{\partial^2 E(m, n)}{\partial x^2} \right] + E(m - 1, n)
\end{aligned} \tag{5.13}
$$

In this way, we have approximated the derivatives up to the order Δt^2.

From Eq. 5.3 we have

$$\frac{\partial^2 E(m,n)}{\partial t^2} = \ddot{E} = k(\dot{P} - \dot{E}) - c\frac{\partial^2 E}{\partial t \partial z} \tag{5.14}$$

$$\frac{\partial^2 E(m,n)}{\partial x^2} = \frac{k}{c}\left(\frac{\partial P}{\partial z} - \frac{\partial E}{\partial z}\right) - \frac{1}{c}\frac{\partial^2 E}{\partial z \partial t} \tag{5.15}$$

If we multiply Eq. 5.15 by c^2 and then subtract it from Eq. 5.14

$$\frac{\partial^2 E(m,n)}{\partial t^2} - c^2\frac{\partial^2 E(m,n)}{\partial x^2} = k(\dot{P} - \dot{E}) - ck\left(\frac{\partial P}{\partial z} - \frac{\partial E}{\partial z}\right). \tag{5.16}$$

As

$$\dot{P} = (1/T_2)(DE - P),$$

and

$$\dot{E} = k(P - E) - c\frac{\partial E}{\partial x},$$

the right side of the Eq. 5.16 can be simplified to

$$\frac{\partial^2 E(m,n)}{\partial t^2} - c^2\frac{\partial^2 E(m,n)}{\partial x^2} =$$

$$k\left[(1/T_2)(DE - P) - k(P - E) + c\frac{\partial E}{\partial x}\right] + ck\left(\frac{\partial E}{\partial x} - \frac{\partial P}{\partial x}\right) =$$

$$k\left[(1/T_2)(DE - P) - k(P - E)\right] + 2ck\frac{\partial E}{\partial x} - ck\frac{\partial P}{\partial x} =$$

$$k\left[(1/T_2)(DE - P) - k(P - E)\right] + 2k\frac{E(m,n) - E(m-1,n)}{\Delta t}$$

$$- k\frac{P(m,n) - P(m-1,n)}{\Delta t} =$$

$$k\left[(1/T_2)(DE - P) - (1/T_2 + k)P + kE\right] + 2k\frac{E(m,n) - E(m-1,n)}{\Delta t}$$

$$- k\frac{P(m,n) - P(m-1,n)}{\Delta t} \tag{5.17}$$

where we used the following relationship for the speed of wave propagation in vacuum

$$c = \frac{\Delta x}{\Delta t},$$

69

Therefore, evolution of electric field in time and space is given by

$$E(m, n+1) = E(m-1, n) + k\Delta t(P-E) \tag{5.18}$$
$$+ \frac{1}{2}\Delta t^2 k \left[(1/T_2)DE - (1/T_2)P - kP + kE\right]$$
$$+ k\Delta t[E(m,n) - E(m-1,n)]$$
$$- \frac{1}{2}k\Delta t[P(m,n) - P(m-1,n)],$$

rearranging the equation results in:

$$E(m, n+1) = \left(1 - k\Delta t\right)E(m-1, n) \tag{5.19}$$
$$+ \left(\frac{1}{2}k\Delta t - \frac{1}{2}k\Delta t^2(1/T_2 + k)\right)P(m,n)$$
$$+ \left(\frac{1}{2}(k\Delta t)^2 E(m,n) + \frac{1}{2}k(1/T_2)\Delta t^2\right)D(m,n)E(m,n)$$
$$+ \left(\frac{1}{2}k\Delta t\right)P(m-1, n).$$

Following a similar procedure, the equations for P and D are obtained. The details and the full derivations of this method can be found in [224].

Because we have neglected noise in our treatment, the solutions would remain $|E| = |P| = 0$ for all times. In order to get the laser started, one must therefore assume a small initial disturbance of the electric field, e.g., a Gaussian [224]

$$E(z, 0) = 0.1 e^{-100(\frac{z}{L} - \frac{1}{2})^2}. \tag{5.20}$$

The initial inversion D is set to the threshold pumping p_f which is the minimum injection current needed to start the lasing action.

$$P(z, 0) = 0, \ D(z, 0) = p_f. \tag{5.21}$$

Figure 5.8 indicates the transient buildup of the intensity for a ring cavity without the saturable absorber effect. After a few round trips, E, P, and D reach the approximate periodic steady state. To investigate the saturable absorber effect, we recalculate the variables including the saturable absorber term in the Maxwell-Bloch equations, see Eq. 5.8.

For the parameters corresponding to the optimized 3QW QCL including the SA, the lasing instability appears as the rise of the side modes with the increase of the SA coefficient. The energy in the Rabi sidebands can change either discontinuously or continuously at the RNGH instability threshold [126]. In lasers with slow gain recovery time, the transition in the Rabi sidebands is discontinuous [225], however, because of
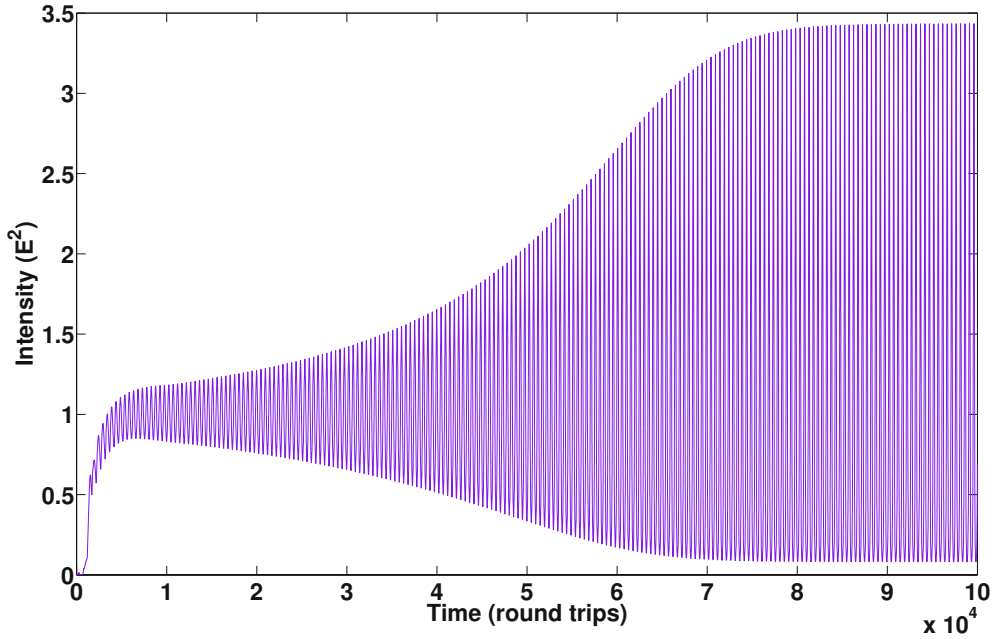
Figure 5.8.: Intensity as a function of time. In this graph, $p_f = 16$, $L = 6 \times 10^{-3} m$, $k = 1/(10T_2)$, and $T_1 = 2T_2$. After a few round trips, the variables saturate to the approximate continuous wave solution in which the intensity is transformed from the initial Gaussian to a the stable operation mode.

the fast gain recovery time in QCLs, Rabi sidebands continuously grow around the central cw mode, see Fig. 5.9. Furthermore, more Rabi side modes appear with the increase of the pumping strength.

5.4. Quantum Cascade Detectors

Intersubband (ISB) photodetectors, demonstrated in 1987 in the form of photoconductive quantum-well infrared photodetectors [226], has attracted much scientific attention in recent years. Particularly at the energetic extremes of infrared radiation, namely in the low energy THz and in the high-energy near-infrared ranges, there are still challenges in finding suitable materials and designs for ISB photodetectors [227].

In the NIR, fast intraband semiconductor photodetectors are only available for wavelengths up to about 1.6 μm. For the other end of optical spectrum, namely for detection of THz radiation, bolometers are widely used; however, they are not well suited for high-speed applications. ISB photodetectors can be designed for a wide range of wavelengths in a single material system just by choosing adequate semiconductor layer thicknesses [227]. This advantage of ISB photodetectors make them very
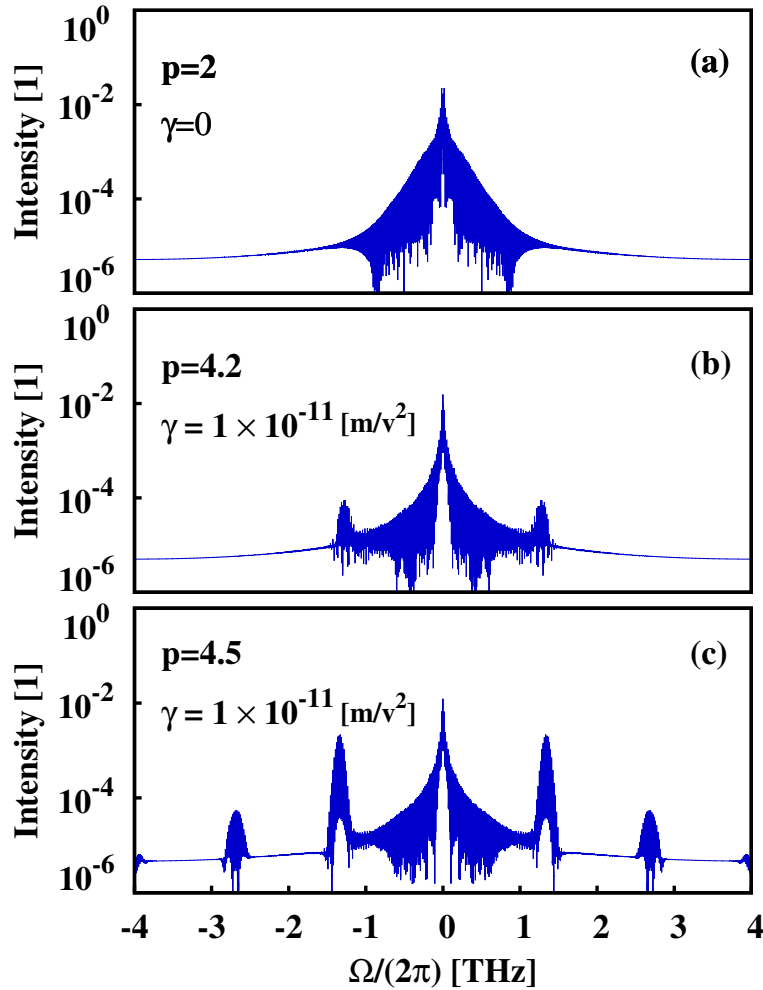
Figure 5.9.: The spectra of the optical intensity in logarithmic scale for (a) no SA coefficient (b) SA coefficient at the instability threshold, and (c) SA coefficient at the instability threshold and a larger pumping factor.

promising candidates for THz radiation. Compared with photoconductive ISB photodetectors, the research on zero-bias photovoltaic ISB photodetectors has seen less progress. Schneider et al. [228, 229] observed pronounced photovoltaic effects in an asymmetric multi-QW structure. According to Schneider [230], an optimized photovoltaic photodetector has superior noise properties, the capability to operate at higher photon fluxes, and an improved dynamical range.

Hofstetter et al. [231] used a QCL structure as photovoltaic detector which is employed as a prototype device in this section. In analogy to the functioning of a QCL, a similar but optimized ISB detector presented by Gendron et al. [232] was named quantum cascade detector (QCD). QCDs offer more design freedom for a given material composition.

The operating principle of a QCD is outlined in Fig. 5.10. A ground level electron is
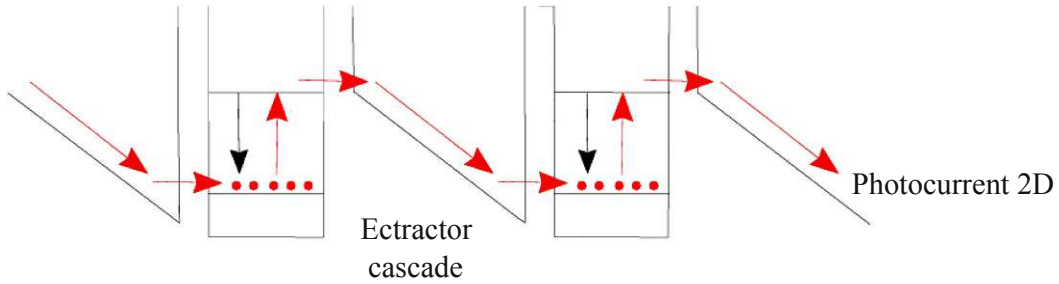
Figure 5.10.: Schematic conduction-band diagram of a QCD. Ground-level electrons are excited to the active QW's upper level by absorbing a photon. Due to the asymmetric band profile between two active QWs, the cascade excited electrons relax mostly in one direction (in this case to the right), resulting in a net photocurrent. Adapted from [227].

excited to a higher state by absorbing a photon. Due to the asymmetric design, the electron relaxes in a preferred direction into the quantum well of the next cascade. This concept reduces dark current and dark current noise.

We have developed the QCL optimization algorithm to maximize the performance of QCDs. The QCD device $N1022$ reported in [227] is selected as the reference design. The layer sequence of the $In_{0.53}Al_{0.47}As/In_{0.53}Ga_{0.47}As$ QCD structure, starting with the well, is as follows: $\underline{5.1}$/7.5/1.25/6.5/1.45/6.4/1.7/7.9/2.0/7.7/2.4/7.5/2.9/7.1/3.5/6.8 nm. The underlined layer is n-doped with Si at $4 \times 10^{17} cm^{-3}$.

The responsivity at the room temperature is selected as the figure of merit. The wavelength operation of the optimized structures are set to be the same as the wavelength of the reference design. The optimization results for the responsivity is presented in Fig. 5.11. Larger responsivities are achieved for optimized QCD structures. However, for larger responsivities the bandwidths of optimized QCDs are increased. The results indicate the excellent performance of our developed optimizer for QCDs.
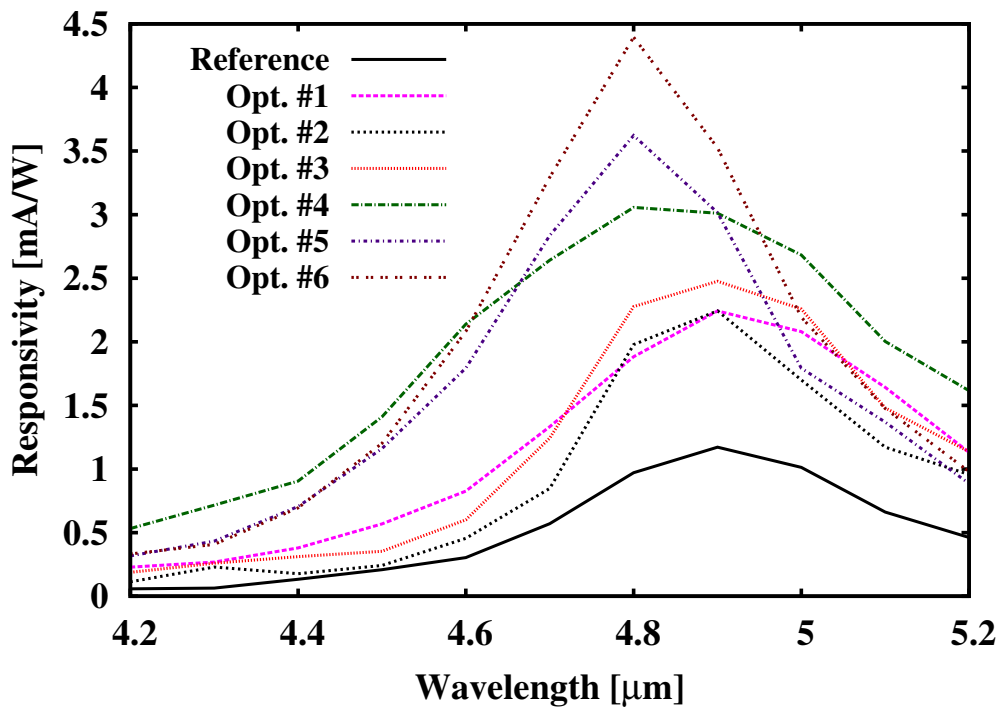
Figure 5.11.: Responsivity of the ISB transition at room temperature. The responsivity values of 3.07, 2.39, 2.12, 2.71, 3.51, and 4.45 mA/W are obtained for the optimized QCDs from number 1 to 6, respectively.

6. Summary and Conclusions

Despite the identification of various possible applications, the terahertz region (1-10 THz) has remained one of the least developed spectral regions. Photonic approaches to direct terahertz generation are limited due to the lack of appropriate materials with sufficiently flexible small bandgaps. In this thesis, we investigate the applications of semiconductor nanostructures as MIR/THz sources and detectors. The optical properties of graphene-based materials as well as quantum cascade structures are studied.

We theoretically studied the optical properties of AGNRs/BN, employing tight-binding (TB) calculations. We demonstrate that in AGNRs/BN only optical transitions from subbands with odd (even) indices to subbands with odd (even) indices are allowed. This transition rule is more restricted for AGNRs and completely different from that of ZGNRs. Our TB results are in agreement with first principle calculations which verify the accuracy of our model. The applicability of AGNR/BN as photodetectors is investigated. Our results indicate that due to more allowed transitions compared to conventional GNRs a larger photo current in AGNR/BN structures can be achieved. Two analytical approximations of the discrete energies in ZGNRs are presented. Relations for the wave functions and the energy dispersion show good agreement with those obtained from numerical calculations. Our simple approximation is applicable for a wide range of ZGNR indices from $N = 6$ to $N = 500$. While the results show good agreement for narrow N-ZGNRs, the accuracy increases for wider ZGNRs. The analytical model developed is used to derive optical transition rules. Our model shows that transitions from odd to odd and even to even subband numbers are allowed and that other transitions are forbidden in ZGNRs. The model is applicable for the evaluation of optical properties of ZGNRs, such as dielectric response, absorption coefficient, and energy loss spectrum.

Furthermore, the optical properties of graphene nanoribbon superlattices embedded in boron nitride sheets and the possibility of using such structures as photodetectors are studied. We propose a set of TB parameters for the investigated structures, which yields an excellent agreement with first-principles results. The results indicate that the optical spectrum of a BN-confined AGNR superlattice contains more absorption peaks and allow more optical intersubband transitions compared with a hydrogen passivated superlattice of the same geometry. Employing the NEGF method, the photocurrents and quantum efficiencies are evaluated and compared for both devices at various incident photon energies. Using statistical approach, the role of line-edge roughness on

the optical properties of GNR-based superlattices is investigated. The results indicate that the quantum efficiency and photoresponsivity decrease in the presence of line-edge roughness. For hydrogen-passivated superlattices (HSL), induced states appear and increase with the roughness amplitude, which result in the appearance of an additional peak in photocurrent spectrum. In comparison with HSLs, BN superlattice (BNSL) photodetectors exhibit more robust optical properties in the presence of line-edge roughness due to the stable edge atom configuration.

As intersubband transition structures provide small energy gaps suitable for THz, we comprehensively investigated the bandgap-engineering in quantum cascade lasers (QCLs) and detectors (QCDs). A framework has been developed to optimize and engineer the band structure by modifying the structural parameters, including the barrier and well thicknesses, from the perspective of predefined figure of merits. For QCLs, we maximize the optical gain with regard to the instability threshold for MIR/THz short pulse applications. This instability, caused by saturable absorber (SA), leads to passive mode-locking and short pulses in ring cavity QCLs. Optimized structures exhibit a larger optical gain and operate below the instability threshold in comparison with the reference design. The results indicate the instability threshold decreases faster with SA coefficient for mid infrared QCL sample while the terahertz QCL sample still operates below the instability threshold.

Two different active-region designs are investigated. The first one is the original design based on a three quantum well (3QW) active-region separated from the injection/relaxation region by a tunneling barrier, whereas the second one consists of a superlattice (SL) active-region. The SL active-region QCL indicates more stable operation and higher instability threshold. However, the matrix element and lifetimes of the lasing transition, which are the key parameters in linear stability analysis, are proportional to optical gain. The 3QW QCL exhibits larger optical gain at nearly the same wavelength. The optical gain of 3QW structure is maximized by delocalizing the lasing states, while in the SL active-region QCL, there is no significant lifetime variation because of the bound states. However, due to the larger matrix element, better instability condition is achieved for the SL active-region QCL. The dynamics of all the optimized designs above the threshold instability is numerically analyzed by solving the Maxwell-Bloch equations. The results indicate that the lasing instability, which appears as side modes in the optical spectrum, occurs with the increase of the SA coefficient even at low pumping strength. The increase of the SA coefficient and pumping strength reduce the instability threshold, whereas the instability characteristics is broadened by the pumping strength. We applied the developed optimizer to QCDs with responsivity and the bandwidth as figure of merits. Larger responsivities are achieved for optimized QCD structures. However, for larger responsivities the bandwidths of optimized QCDs are increased. The results indicate the excellent performance of our developed optimizer for QCDs.

Appendix A.

AGNR Optical Matrix Elements

To obtain the transition rules in Sec. 2.2, the gradient approximation Eq.2.12 and the wavefunction Eq. 2.22 are used. The momentum matrix elements Eq. 2.23 are obtained as

$$
p_{n,m}(k_x) = \frac{1}{(N+1)} \frac{im_0}{\hbar} \sum_{p=1}^{N} \sum_{q=1}^{N} \Bigg[
$$

$$
+ (x_q^B - x_p^A) e^{ik_x(x_q^B - x_p^A)} \sin(n\theta p) \sin(m\theta q) \langle A_p|H|B_q \rangle e^{-i\varphi_m(k_x)} \qquad \text{(A.1)}
$$

$$
- (x_q^A - x_p^B) e^{ik_x(x_q^A - x_p^B)} \sin(n\theta p) \sin(m\theta q) \langle B_p|H|A_q \rangle e^{+i\varphi_n(k_x)} \Bigg] ,
$$

where $\langle A_p|H|B_q \rangle = \langle B_p|H|A_q \rangle = t$ for $p = q$ and $p = q \pm 1$, otherwise the matrix elements are zero. Therefore, Eq. A.1 can be written as

$$
p_{n,m}(k_x) = \frac{1}{(N+1)} \frac{im_0}{\hbar} t a_{\text{cc}} \sum_{p=1}^{N} \sin(n\theta p) \Bigg[
$$

$$
+ e^{-i\varphi_m(k_x)} \left(+ e^{+ik_x a_{\text{cc}}} \sin(m\theta p) - \frac{1}{2} e^{-ik_x a_{\text{cc}}/2} \left[\sin(m\theta(p-1)) + \sin(m\theta(p+1)) \right] \right)
$$

$$
- e^{+i\varphi_n(k_x)} \left(- e^{-ik_x a_{\text{cc}}} \sin(m\theta p) + \frac{1}{2} e^{+ik_x a_{\text{cc}}/2} \left[\sin(m\theta(p-1)) + \sin(m\theta(p+1)) \right] \right) \Bigg] .
$$

$$
= \frac{1}{(N+1)} \frac{im_0}{\hbar} t a_{\text{cc}} \left[\sum_{p=1}^{N} \sin(n\theta p) \sin(m\theta p) \right] \times
$$

$$
\left(+ e^{-i\varphi_m(k_x)} \left(e^{+ik_x a_{\text{cc}}} - e^{-ik_x a_{\text{cc}}/2} \cos(m\theta) \right) + e^{+i\varphi_n(k_x)} \left(e^{-ik_x a_{\text{cc}}} - e^{+ik_x a_{\text{cc}}/2} \cos(m\theta) \right) \right) .
$$

$$
\text{(A.2)}
$$

Here the relation $\sin(x) + \sin(y) = 2\sin((x+y)/2)\cos((x-y)/2)$ is employed. Using Eq. 2.21, Eq. A.2 can be written as

$$p_{n,m}(k_x) = \frac{1}{(N+1)} \frac{im_0}{\hbar} ta_{cc} \left[\sum_{p=1}^{N} \sin(n\theta p) \sin(m\theta p) \right] \times$$

$$\left(+ \frac{1}{|f_m(k_x)|} \left(1 - 2\cos^2(m\theta) + 2e^{+i3k_x a_{cc}/2} \cos(m\theta) - e^{-i3k_x a_{cc}/2} \cos(m\theta) \right) \right.$$

$$\left. + \frac{1}{|f_n(k_x)|} \underbrace{\left(1 - 2\cos(m\theta)\sin(n\theta) + 2e^{-i3k_x a_{cc}/2} \cos(n\theta) - e^{+i3k_x a_{cc}/2} \cos(m\theta) \right)}_{F_{n,m}(kx)} \right) .$$

$$= \frac{1}{(N+1)} \frac{im_0}{\hbar} ta_{cc} \left[\sum_{p=1}^{N} \sin(n\theta p) \sin(m\theta p) \right] F_{n,m}(k_x) .$$

$$(A.3)$$

The summation over the sine functions in Eq. A.3 determines the transition rules. Using some trigonometric identities one can write this summation as

$$\sum_{p=1}^{N} \sin(n\theta p)\sin(m\theta p) = \frac{1}{2} \left[+ \cos\frac{(n-m)\pi}{2} \sin\frac{(n-m)\pi N}{2(N+1)} \left(\sin\frac{(n-m)\pi}{2(N+1)} \right)^{-1} \right.$$

$$\left. - \cos\frac{(n+m)\pi}{2} \sin\frac{(n+m)\pi N}{2(N+1)} \left(\sin\frac{(n+m)\pi}{2(N+1)} \right)^{-1} \right] .$$

$$(A.4)$$

If $n \pm m = 2k+1$, where k is a non-zero integer, both terms in the bracket of Eq. A.4 will be zero. In the case of $n \pm m = 2k$, both terms in the bracket will be equal to -1, therefore, the summation will be again zero. However, if $n = m$, the fist term in will be equal to N and the second term will be equal to -1. Therefore, only transitions between valence and conduction subbands with the same band-index are allowed

$$\sum_{p=1}^{N} \sin(n\theta p)\sin(m\theta p) = \begin{cases} \dfrac{N+1}{2} & , \quad n = m \\ 0 & , \quad n \neq m \end{cases} \qquad (A.5)$$

78

Appendix B.

ZGNR Optical Matrix Elements

B.1. Bloch Wave Functions Prefactors

To obtain C_A and C_B in Eq. 2.18, one can substitute Eq. 2.6 and Eq. 2.19 into the Shrödinger equation $H|\psi\rangle = E|\psi\rangle$. Considering an A-type carbon atom at some atomic site n, and its three nearest neighbors, the Hamiltonian can be written as:

$$H = t|B_{N-n+1}\rangle\langle A_n| + t|B'_{N-n+1}\rangle\langle A_n| + t|B_{N-n}\rangle\langle A_n|. \tag{B.1}$$

Using Eq. B.1 along with the wave functions obtained in Eq. 3.12, one obtains:

$$EC_A e^{ik_x x_n^A} \sin(n\theta) = tC_B e^{ik_x x_{N-n+1}^B} \sin((N-n+1)\theta)$$
$$+ tC_B e^{ik_x x_{N-n+1}^{B'}} \sin((N-n+1)\theta) \tag{B.2}$$
$$+ tC_B e^{ik_x x_{N-n}^B} \sin((N-n)\theta).$$

Therefore, the relation between C_A and C_B can be written as:

$$EC_A \sin(n\theta) = tC_B \left[\left(e^{ik_x\left(x_{N-n+1}^B - x_n^A\right)} + e^{ik_x\left(x_{N-n+1}^{B'} - x_n^A\right)} \right) \right.$$
$$\left. \sin\left((N-n+1)\theta\right) + e^{ik_x\left(x_{N-n}^B - x_n^A\right)} \sin\left((N-n)\theta\right) \right] \tag{B.3}$$
$$= tC_B \left[2\cos\left(\frac{\sqrt{3}}{2}k_x a_{cc}\right) \sin((N-n+1)\theta) + \sin((N-n)\theta) \right].$$

By employing the relation $\sin(x)\sin(y) = (1/2)[\cos(x-y) - \cos(x+y)]$ and using Eq. 3.22,

$$EC_A = -tC_B \frac{\sin(\theta)}{\sin((N+1)\theta)}. \tag{B.4}$$

Analogously, for the $N - n + 1$th B-type carbon atom one can obtain the following relation:

$$EC_B \sin\left((N - n + 1)\,\theta\right) = tC_A \left[2\cos\left(\frac{\sqrt{3}}{2}k_x a_{cc}\right)\sin(n\theta) + \sin((n-1)\theta)\right] \quad \text{(B.5)}$$

which gives

$$EC_B = -tC_A \frac{\sin(\theta)}{\sin((N+1)\theta)}. \quad \text{(B.6)}$$

From Eq. B.4 and Eq. B.6, one can find that $C_A = \pm C_B$.

Also, the dispersion relation can be found by multiplying Eq. B.3 by Eq. B.5,

$$E^2 C_A C_B \sin(n\theta)\sin((N - n + 1)\theta)$$

$$= t^2 C_A C_B \left[4\cos^2\left(\frac{\sqrt{3}}{2}k_x a_{cc}\right)\sin((N - n + 1)\theta)\sin(n\theta)\right.$$

$$+ 2\cos\left(\frac{\sqrt{3}}{2}k_x a_{cc}\right)\sin((N - n + 1)\theta)\sin((n - 1)\theta)$$

$$+ 2\cos\left(\frac{\sqrt{3}}{2}k_x a_{cc}\right)\sin((N - n)\theta)\sin(n\theta)$$

$$\left. + \sin((N - n)\theta)\sin((n - 1)\theta)\right]. \quad \text{(B.7)}$$

With the help of trigonometric identities and Eq. 3.22, this expression can be reformatted as

$$E = \pm t \left[1 + 4\cos^2\left(\frac{\sqrt{3}}{2}k_x a_{cc}\right) + 4\cos\left(\frac{\sqrt{3}}{2}k_x a_{cc}\right)\cos(\theta)\right]^{1/2}. \quad \text{(B.8)}$$

B.2. Transverse Wave Functions Amplitude

To solve the recursive formula,

$$\phi_{n+1} - C\phi_n + \phi_{n-1} = 0, \quad \text{(B.9)}$$

one can consider the ansatz $\phi_n = t^n$ and follow similar equation,

$$t^2 - Ct + 1 = 0. \quad \text{(B.10)}$$

This equation is the generating polynomial of the recursive formula B.9.
The roots of B.10 are

$$t_{1,2} = \frac{\left(C \pm \sqrt{C^2 - 4}\right)}{2}. \tag{B.11}$$

The general solution of the difference equation is

$$\phi_n = \alpha t_1^n + \beta t_2^n, \tag{B.12}$$

since t_1 is a root of the equation, the other root t_2 can be written as: $t_2 = t_1^{-1}$.
By substituting those two roots in B.12 one obtains

$$\phi_n = \alpha t_1^n + \beta t_1^{-n}. \tag{B.13}$$

Imposing the initial condition $\phi_0 = 0$ results in

$$\alpha + \beta = 0, \quad \alpha = -\beta, \tag{B.14}$$

and from the B.13,

$$\phi_n = \alpha(t_1^n - t_1^{-n}). \tag{B.15}$$

We obtain

$$\alpha = \frac{\phi_1}{\sqrt{C^2 - 4}}, \quad \beta = -\frac{\phi_1}{\sqrt{C^2 - 4}}. \tag{B.16}$$

By substituting B.11 and B.16 in B.15, one obtains

$$\phi_n = \frac{\phi_1}{\sqrt{C^2 - 4}} \left(\frac{C + \sqrt{C^2 - 4}}{2}\right)^n - \frac{\phi_1}{\sqrt{C^2 - 4}} \left(\frac{C - \sqrt{C^2 - 4}}{2}\right)^n. \tag{B.17}$$

B.17 can be rewritten as

$$\phi_n = \frac{\left(\frac{C + \sqrt{C^2 - 4}}{2}\right)^n - \left(\frac{C - \sqrt{C^2 - 4}}{2}\right)^n}{\sqrt{C^2 - 4}} \phi_1. \tag{B.18}$$

B.3. Optical Matrix Elements

Using Eq. 3.12 and Eq. 2.13 the matrix elements $p_{\theta,\theta'}(k_x) \equiv \langle +, \theta, k_x | p_x | -, \theta', k_x \rangle$ for an interband transition from a valence band state $|-, \theta, k_x\rangle$ to a conduction band state $|+, \theta', k_x\rangle$ are obtained as

$$P_{\theta,\theta'} = (x_{\theta'} - x_\theta) \frac{i m_0}{\hbar} \langle \theta | H | \theta' \rangle \tag{B.19}$$

$$P_{\theta,\theta'} = \frac{im_0}{\hbar\Omega} \sum_{n=1}^{N} \sum_{m=1}^{N} \left[e^{ik(x_m^B - x_n^A)} \sin(n\theta)\sin(m\theta')\langle A_n|H|B_m\rangle(x_m^B - x_n^A) \right.$$

$$\left. - e^{ik(x_m^A - x_n^B)} \sin(n\theta')\sin(m\theta)\langle B_n|H|A_m\rangle(x_m^A - x_n^B) \right]. \tag{B.20}$$

Considering only the nearest neighbors, each atom with some index n has two neighbors with index $N-n+1$ and one neighbor with index $N-n$, see Fig. 3.1. Therefore, the index m has only three values with $\langle A_n|H|B_m\rangle = t$. So we have

$$P_{\theta,\theta'} = \left(\frac{im_0}{\hbar\Omega}\right)\left(\frac{i\sqrt{3}a_{cc}t}{2}\right)\sum_{n=1}^{N}\left[\left(e^{i\sqrt{3}k_x a/2} - e^{-i\sqrt{3}k_x a/2}\right)\sin(n\theta)\sin((N-n+1)\theta')\right.$$

$$\left. - \left(e^{-i\sqrt{3}k_x a/2} - e^{i\sqrt{3}k_x a/2}\right)\sin(n\theta')\sin((N-n+1)\theta)\right], \tag{B.21}$$

after some algebra and replacing Ω from Eq. 3.16, the optical matrix elements are

$$P_{\theta,\theta'} = \frac{-2\sqrt{3}m_0 a_{cc}t}{\hbar(2N+1)}\sin\left(\frac{\sqrt{3}}{2}ka_{cc}\right)\sum_{n=1}^{N}\left[\sin(n\theta)\sin((N-n+1)\theta')-\right.$$

$$\left.\sin(n\theta')\sin((N-n+1)\theta)\right]. \tag{B.22}$$

Appendix C.

QCL Linear Stability Analysis

The standard Maxwell-Bloch equations with a SA added can be rewritten as [128]:

$$\partial_t E = -\frac{c}{n}\partial_z E - \frac{c}{n}\frac{i\mu P}{\hbar l_0 D_{\text{th}}} - \frac{c}{2n}(l_0 - \bar{\gamma}|E|^2)E, \tag{C.1}$$

$$\partial_t P = \frac{i\mu}{2\hbar}DE - \frac{P}{T_2}, \tag{C.2}$$

$$\partial_t D = \frac{D_{\text{p}} - D}{T_1} + \frac{i\mu}{\hbar}(E^*P - c.c.). \tag{C.3}$$

The dynamics of a two-level QCL gain medium with ring cavity can be described using the Maxwell-Bloch equations. After transformation of the variables, the Maxwell-Bloch equations can be simplified to:

$$\partial_t E = -\frac{c}{n}\partial_z E - \frac{c}{n}iP - \frac{c}{2n}\left(l_0 - \bar{\gamma}|E|^2\right)E, \tag{C.4}$$

$$\partial_t P = -\frac{i}{2}DE - \frac{P}{T_2}, \tag{C.5}$$

$$\partial_t D = \frac{p_f l_0}{T_1 T_2} - \frac{D}{T_1} + i\left(E^*P - c.c.\right). \tag{C.6}$$

To proceed with the linear stability analysis, we express each of the variables as the sum of the steady-state value and the small perturbations $\delta E, \delta P$, and δD.

The steady state solution can be found by setting the left-hand sides of the Eqs. (C.4)-(C.6) to zero. The steady state solutions has the form $E = \bar{E}$, $P = \bar{P}$, and $D = \bar{D}$

are constants in time and space satisfying:

$$\bar{D} = \frac{l_0}{T_2} - \frac{\bar{\gamma}\bar{E}^2}{T_2}, \tag{C.7}$$

$$\bar{P} = \frac{i}{2}\left(l_0 - \bar{\gamma}\bar{E}^2\right)\bar{E}, \tag{C.8}$$

$$p_f + 1 = \left(1 - \frac{\bar{\gamma}\bar{E}^2}{l_0}\right)\left(1 + \bar{E}^2 T_1 T_2\right). \tag{C.9}$$

The resulting equations regarding the fluctuations are

$$\partial_t \delta P_I = \frac{1}{2}\left(\bar{D}\delta E_R + \delta D\bar{E}\right] - \frac{\delta P_I}{T_2}, \tag{C.10}$$

$$\partial_t \delta D = -T_2 \bar{D}\bar{E}\partial E_R - 2\bar{E}\delta P_I - \frac{\delta D}{T_1}, \tag{C.11}$$

$$\partial_t \delta E_R = \frac{c}{n}\left[-\partial_z \delta E_R + \delta P_I - \left(l_0 - 3\gamma\bar{E}^2\right)\frac{\delta E_R}{2}\right], \tag{C.12}$$

$$\partial_t \delta P_R = -\frac{1}{2}\bar{D}\delta E_I - \frac{\delta P_R}{T_2}, \tag{C.13}$$

$$\partial_t \delta E_I = \frac{c}{n}\left[-\partial_z \delta E_I - \delta P_R - \left(l_0 - \gamma\bar{E}^2\right)\frac{\delta E_I}{2}\right]. \tag{C.14}$$

The two sets of equations, (C.10)-(C.12) and (C.13)-(C.14), are decoupled, and translationally invariant. Thus their eigenfunctions are plane waves [126]. It holds $\delta P_I(z,t) = \delta P_I(t)e^{ikz}$, and similar for relations δD and δE_R. The stability of the cw solution is determined by the eigenvalues of the matrix

$$
M = \begin{pmatrix} -T_2^{-1} & \dfrac{1}{2T_2}\left(l_0 - \bar{\gamma}\bar{E}^2\right) & \dfrac{1}{2}\bar{E} \\[2ex] \dfrac{c}{n} & \dfrac{c}{n}\left(-\dfrac{1}{2}l_0 + \dfrac{3}{2}\bar{\gamma}\bar{E}^2 - ik\right) & 0 \\[2ex] -2\bar{E} & \bar{\gamma}\bar{E}^3 - l_0\bar{E} & -T_2^{-1} \end{pmatrix}.
\tag{C.15}
$$

If all eigenvalues have a negative real part, the cw solution is stable.

For $l_0 = 0$ and $\bar{\gamma} = 0$, the eigenvalue with the greatest real part is $\lambda_0(K) = -ick/n$. Putting $\lambda(K) = \lambda_0(K) + \lambda_1(K)$ into the characteristic polynomial of M and equating the parts which are first order in $l_0, \bar{\gamma}$, and $\lambda_1(K)$, one arrives at

$$
\begin{aligned}
\lambda_{max} = & -i\Omega - \frac{l_0 c}{2n}\frac{(\Omega T_1 + i)\Omega T_2 - 2(p_f - 1)}{(\Omega T_1 + i)(\Omega T_2 + i) - (p_f - 1)} \\
& + \frac{\gamma\hbar^2(p_f - 1)}{\mu^2 T_1 T_2}\frac{(\Omega T_1 + i)(3\Omega T_2 + 2i) - 4(p_f - 1)}{(\Omega T_1 + i)(\Omega T_2 + i) - (p_f - 1)},
\end{aligned}
\tag{C.16}
$$

where $p_f = D_p/D_{th}$ and $\Omega = kc/n$. Taking the real part of Eq. C.16 one obtains Eq. 5.6.

Bibliography

[1] D. Bimberg, Ed., *Semiconductor Nanostructures.* Berlin: Springer, 2008.

[2] S. Kumar, C. W. I. Chan, Q. Hu, and J. L. Reno, "A 1.8-THz Quantum Cascade Laser Operating Significantly Above the Temperature of ω/k_B," *Nature Physics*, vol. 7, no. 2, pp. 166–171, 2011.

[3] B. Williams, S. Kumar, Q. Hu, and J. Reno, "Operation of Terahertz Quantum-Cascade Lasers at 164 K in Pulsed Mode and at 117 K in Continuous-Wave Mode," *Opt. Express*, vol. 13, no. 9, pp. 3331–3339, 2005.

[4] B. S. Williams, H. Callebaut, S. Kumar, Q. Hu, and J. L. Reno, "3.4-THz Quantum Cascade Laser Based on Longitudinal-Optical-Phonon Scattering for Depopulation," *Appl. Phys. Lett.*, vol. 82, no. 7, pp. 1015–1017, 2003.

[5] M. Tacke, "New Developments and Applications of Tunable IR Lead Salt Lasers," *Infrared Physics & Technology*, vol. 36, no. 1, pp. 447–463, 1995.

[6] S. E. Rosenbaum, B. K. Kormanyos, L. M. Jelloian, M. M. A. S. Brown, L. E. Larson, L. D. Nguyen, M. A. Thompson, L. P. Katehi, and G. M. Rebeiz, "155- and 213-GHz AlInAs/GaInAs/InP HEMT MMIC Oscillators," *IEEE Trans. Microwave Theory Tech.*, vol. 43, no. 4, pp. 927–932, 1995.

[7] X. Cai, A. B. Sushkov, R. J. S. M. M. Jadidi, G. S. Jenkins, L. O. Nyakiti, R. L. Myers-Ward, S. Li, J. Yan, D. K. Gaskill, T. E. Murphy, H. D. Drew, and M. Fuhrer, "Sensitive Room-Temperature Terahertz Detection via the Photothermoelectric Effect in Graphene," *Nature Nanotech.*, vol. 9, no. 10, pp. 814–819, 2014.

[8] Y. Bahk, G. Ramakrishnan, J. Choi, H. Song, G. Choi, Y. H. Kim, K. J. Ahn, D. Kim, and P. C. M. Planken, "Plasmon Enhanced Terahertz Emission from Single Layer Graphene," *Nano Lett.*, vol. 8, no. 9, pp. 9089–9096, 2014.

[9] L. Vicarelli, M. S. Vitiello, D. Coquillat, A. Lombardo, A. C. Ferrari, W. Knap, M. Polini, V. Pellegrini, and A. Tredicucci, "Graphene Field-Effect Transistors as Room-Temperature Terahertz Detectors," *Nature Mater.*, vol. 11, no. 10, pp. 865–871, 2012.

[10] A. V. Muraviev, S. L. Rumyantsev, G. Liu, A. A. Balandin, W. Knap, and M. S. Shur, "Plasmonic and Bolometric Terahertz Detection by Graphene Field-Effect Transistor," *Appl. Phys. Lett.*, vol. 103, no. 18, p. 181114 (4pp), 2013.

[11] D. Spirito1, D. Coquillat, S. L. D. Bonis, A. Lombardo, M. Bruna, A. C. Ferrari, V. Pellegrini, A. Tredicucci, W. Knap, and M. S. Vitiello, "High Performance Bilayer-Graphene Terahertz Detectors," *Appl. Phys. Lett.*, vol. 104, no. 6, p. 061111 (5pp), 2014.

[12] R. Musah, S. Y. Mensah, and S. S. Abukari, "Terahertz Generation and Amplification in Graphene Nanoribbons in Multi-Frequency Electric Fields," *Physica E*, vol. 61, pp. 90–94, 2014.

[13] C. C. Sirtori, S. Barbieri, and R. Colombelli, "Wave Engineering with THz Quantum Cascade Lasers," *Nature Photo.*, vol. 7, no. 9, pp. 691–701, 2013.

[14] M. Ravaro, P. Gellie, G. Santarelli, C. Manquest, P. Filloux, C. Sirtori, J. Lampin, G. Ferrari, S. P. Khanna, E. H. Linfield, H. E. Beere, D. A. Ritchie, and S. Barbieri, "Stabilization and Mode Locking of Terahertz Quantum Cascade Lasers," *IEEE J. Select. Topics Quantum Electron.*, vol. 19, no. 1, p. 8501011 (11pp), 2013.

[15] S. Barbieri AND M. Ravaro P. Gellie AND G. Santarelli C. Manquest AND C. Sirtori AND S. P. Khanna AND E. H. Linfield A. G. Davies, "Coherent Sampling of Active Mode-Locked Terahertz Quantum Cascade Lasers and Frequency Synthesis," *Nature Photo.*, vol. 5, no. 5, pp. 306–313, 2011.

[16] A. W. M. Lee, S. B. Williams, S. Kumar, Q. Hu, and J. L. Reno, "Tunable Terahertz Quantum Cascade Lasers with External Gratings," *Opt. Express*, vol. 35, no. 7, pp. 910–912, 2010.

[17] A. Benz, M. Krall, S. Schwarz, D. Dietze, H. Detz, A. M. Andrews, W. Schrenk, G. Strasser, and K. Unterrainer, "Resonant Metamaterial Detectors Based on THz Quantum-Cascade Structures," *Sci. Rep.*, vol. 4, no. 1, pp. 1–10, 2014.

[18] A. Wade, G. Fedorov, D. Smirnov, S. Kumar, B. S. Williams, Q. Hu, and J. L. Reno, "Magnetic-Field-Assisted Terahertz Quantum Cascade Laser Operating up to 225 K," *Nature Photo.*, vol. 3, no. 1, pp. 41–45, 2009.

[19] M. T. Amanti, M. Fischer, G. S. M. Beck, and J. Faist, "Low-Divergence Single-Mode Terahertz Quantum Cascade Laser," *Nature Photo.*, vol. 3, no. 10, pp. 586–590, 2009.

[20] E. Mujagić, C. Deutsch, H. Detz, P. Klang, M. Nobile, A. M. Andrews, W. Schrenk, K. Unterrainer, and G. Strasser, "Vertically Emitting Terahertz Quantum Cascade Ring Lasers," *Appl. Phys. Lett.*, vol. 95, no. 1, p. 011120 (3pp), 2009.

[21] N. Jukam, S. S. Dhillon, D. Oustinov, J. Madeo, C. Manquest, S. Barbieri, C. Sirtori, S. P. Khanna, E. H. L. A. G. Davies, and J. Tignon, "Terahertz Amplifier Based on Gain Switching in a Quantum Cascade Laser," *Nature Photo.*, vol. 3, no. 12, pp. 715–719, 2009.

[22] B. S. Williams, "Terahertz Quantum-Cascade Lasers," *Nature Photo.*, vol. 1, no. 9, pp. 517–525, 2007.

[23] M. Moradinasab, M. Pourfath, and H. Kosina, "Performance Optimization and Instability Study in Ring Cavity Quantum Cascade Lasers," *IEEE J. Quantum Electron.*, vol. 51, no. 1, pp. 1–7, 2015.

[24] K. Novoselov, A. Geim, S. Morozov, D. Jiang, Y. Zhang, S. Dubonos, I. Grigorieva, and A. Firsov, "Electric Field Effect in Atomically Thin Carbon Films," *Science*, vol. 306, no. 5696, pp. 666–669, 2004.

[25] K. Novoselov, A. Geim, S. Morozov, D. Jiang, M. Katsnelson, I. Grigorieva, S. Dubonos, and A. Firsov, "Two-Dimensional Gas of Massless Dirac Fermions in Graphene," *Nature (London)*, vol. 438, no. 7065, pp. 197–200, 2005.

[26] G. Seol and J. Guo, "Assessment of Graphene Nanomesh and Nanoroad Transistors by Chemical Modification," in *IEEE International Electron Devices Meeting (IEDM)*, 2011, pp. 2.3.1–2.3.4.

[27] Z. Wang, Q. Li, Q. Shi, X. Wang, J. Yang, J. Hou, and J. Chen, "Chiral Selective Tunneling Induced Negative Differential Resistance in Zigzag Graphene Nanoribbon: A Theoretical Study," *Appl. Phys. Lett.*, vol. 92, no. 13, p. 133114 (3pp), 2008.

[28] H. C. Cheng, R. J. Shiue, C. C. Tsai, W. H. Wang, and Y. T. Chen, "High-Quality Graphene pn Junctions via Resist-Free Fabrication and Solution-Based Noncovalent Functionalization," *ACS Nano*, vol. 5, no. 3, pp. 2051–2059, 2011.

[29] M. J. Allen, V. C. Tung, and R. B. Kaner, "Honeycomb Carbon: A Review of Graphene," *Chemical Reviews*, vol. 110, no. 1, pp. 132–145, 2010.

[30] X. Du, I. Skachko, A. Barker, and E. Andrei, "Approaching Ballistic Transport in Suspended Graphene," *Nature Nanotech.*, vol. 3, no. 8, pp. 491–495, 2008.

[31] K. Bolotin, K. Sikesb, Z. Jianga, M. Klimac, G. Fudenberga, J. Honec, P. Kima, and H. Stormera, "Ultrahigh Electron Mobility in Suspended Graphene," *Solid-State Commun.*, vol. 146, no. 9-10, pp. 351–355, 2008.

[32] J.-H. Chen, C. Jang, S. Xiao, M. Ishighami, and M. Fuhrer, "Intrinsic and Extrinsic Performance Limits of Graphene Devices on SiO_2," *Nature Nanotech.*, vol. 3, no. 4, pp. 206–209, 2008.

[33] F. Schwierz, "Graphene Transistors," *Nature Nanotech.*, vol. 5, no. 7, pp. 487–496, 2010.

[34] Semiconductor Industry Association, "International Technology Roadmap for Semiconductors - 2013 Edition," 2013.

[35] P. Tassin, T. Koschny, and C. M. Soukoulis, "Graphene for Terahertz Applications," *Science*, vol. 341, pp. 620–621, 2013.

[36] N. Tombros, C. Jozsa, M. Popinciuc, H. Jonkman, and B. van Wees, "Electronic Spin Transport and Spin Precession in Single Graphene Layers at Room Temperature," *Nature (London)*, vol. 448, no. 7153, pp. 571–574, 2007.

[37] S. Cho, Y.-F. Chen, and M. Fuhrer, "Gate-Tunable Graphene Spin Valve," *Appl. Phys. Lett.*, vol. 91, no. 12, p. 123105 (3pp), 2007.

[38] M. Freitag, "Graphene: Nanoelectronics Goes Flat Out," *Nature Nanotech.*, vol. 3, no. 8, pp. 455–457, 2008.

[39] X. Li, L. Zhang, S. Lee, and H. Dai, "Chemically Derived, Ultrasmooth Graphene Nanoribbon Semiconductors," *Science*, vol. 319, no. 5867, pp. 1229–1232, 2008.

[40] M. Fujita, K. Wakabayashi, K. Nakada, and K. Kusakabe, "Pecular Localized States at Zigzag Graphite Edge," *J. Phys. Soc. Jap.*, vol. 65, no. 7, pp. 1920–1923, 1996.

[41] K. Nakada, M. Fujita, G. Dresselhaus, and M. S. Dresselhaus, "Edge State in Graphene Ribbons: Nanometer Size Effect and Edge Shape Dependence," *Phys. Rev. B*, vol. 54, no. 24, pp. 17 954–17 961, 1996.

[42] M. Moradinasab, H. Nematian, M. Pourfath, M. Fathipour, and H. Kosina, "Analytical Models of Approximations for Wave Functions and Energy Dispersion in Zigzag Graphene Nanoribbons," *J. Appl. Phys.*, vol. 111, no. 7, p. 318 (9pp), 2012.

[43] S. C. Jeon, Y. S. Kim, and D. K. Lee, "Fabrication of a Graphene Nanoribbon with Electron Beam Lithography Using a XR-1541/PMMA Lift-Off Process," *Trans. Electr. and Elec. Materials*, vol. 11, no. 4, pp. 190–193, 2010.

[44] L. P. Biró and P. Lambin, "Nanopatterning of Graphene with Crystallographic Orientation Control," *Carbon*, vol. 48, no. 10, pp. 2677–2689, 2010.

[45] N. Gorjizadeh and Y. Kawazoe, "Chemical Functionalization of Graphene Nanoribbons," *Nanomaterials*, vol. 2010, p. 513501 (7pp), 2010.

[46] H. Sevincli, M. Topsakal, and S. Ciraci, "Superlattice Structures of Graphene-based Armchair Nanoribbons," *Phys. Rev. B*, vol. 78, no. 24, p. 245402 (8pp), 2008.

[47] H. Teong, K.-T. Lam, S. B. Khalid, and G. Liang, "Shape Effects in Graphene Nanoribbon Resonant Tunneling Diodes: A Computational Study," *J. Appl. Phys.*, vol. 105, no. 8, p. 084317 (6pp), 2009.

[48] T. Mueller, F. Xia, and P. Avouris, "Graphene Photodetectors for High-Speed Optical Communications," *Nature Photonics*, vol. 4, no. 5, pp. 297–301, 2010.

[49] M. Moradinasab, M. Pourfath, M. Fathipour, and H. Kosina, "Numerical Study of Graphene Superlattice-Based Photodetectors," vol. PP, no. 99, pp. 1–1, 2015.

89

[50] S. Rakheja and A. Naeemi, "Graphene Nanoribbon Spin Interconnects for Non-local Spin-Torque Circuits: Comparison of Performance and Energy per Bit with cmos Interconnects," *IEEE Trans. Electron Devices*, vol. 59, no. 1, pp. 51–59, 2012.

[51] S. Reich, J. Maultzsch, C. Thomsen, and P. Ordejón, "Tight-Binding Description of Graphene," *Phys. Rev. B*, vol. 66, no. 3, p. 035412 (5pp), 2002.

[52] R. S. Deacon, K. C. Chuang, R. J. Nicholas, K. S. Novoselov, and A. K. Geim, "Cyclotron Resonance Study of the Electron and Hole Velocity in Graphene Monolayers," *Phys. Rev. B*, vol. 76, no. 8, p. 081406 (4pp), 2007.

[53] J. C. Slater and G. F. Koster, "Simplified lcao method for the periodic potential problem," *Phys. Rev.*, vol. 94, no. 6, pp. 1498–1524, 1954.

[54] A. H. C. Neto, F. Guinea, N. M. R. Peres, K. S. Novoselov, and A. K. Geim, "The Electronic Properties of Graphene," *Rev. Mod. Phys.*, vol. 81, no. 1, pp. 109–162, 2009.

[55] A. Roberts, D. Cormode, C. Reynolds, T. Newhouse-Illige, B. J. Leroy, and A. S. Sandhu, "Response of Graphene to Femtosecond High-Intensity Laser Irradiation," *Appl. Phys. Lett.*, vol. 99, no. 5, p. 051912 (3pp), 2011.

[56] X. Wang, Z. Shen, J. Lu, and X. Ni, "Laser-Induced Damage Threshold of Silicon in Millisecond, Nanosecond, and Picosecond Regimes," *J. Appl. Phys.*, vol. 108, no. 3, p. 033103 (7pp), 2010.

[57] A. Garg, K. Avinashi, and K. N. Tripathi, "Laser-Induced Damage Studies in GaAs," *Optics & Laser Technology*, vol. 35, no. 1, pp. 21–24, 2003.

[58] E. Hendry, P. J. Hale, J. Moger, A. K. Savchenko, and S. A. Mikhailov, "Coherent Nonlinear Optical Response of Graphene," *Phys. Rev. Lett.*, vol. 105, no. 9, p. 097401 (4pp), 2010.

[59] H. Zhang, S. Virally, Q. Bao, L. K. Ping, S. Massar, N. Godbout, and P. Kockaert, "Z-Scan Measurement of the Nonlinear Refractive Index of Graphene," *Opt. Lett.*, vol. 37, no. 11, pp. 1856–1858, 2012.

[60] R. R. Nair, P. Blake, A. N. Grigorenko, K. S. Novoselov, T. J. Booth, T. Stauber, N. M. R. Peres, and A. K. Geim, "Fine Structure Constant Defines Visual Transparency of Graphene," *Science*, vol. 320, no. 5881, p. 1308 (1pp), 2008.

[61] T. Ando, Y. Zheng, and H. Suzuura, "Dynamical Conductivity and Zero-Mode Anomaly in Honeycomb Lattices," *Journal of the Physical Society of Japan*, vol. 71, no. 5, pp. 1318–1324, 2002.

[62] V. P. Gusynin, S. G. Sharapov, and J. P. Carbotte, "Unusual Microwave Response of Dirac Quasiparticles in Graphene," *Phys. Rev. Lett.*, vol. 96, no. 25, p. 256802(4pp), 2006.

[63] A. K. Geim and K. S. Novoselov, "The Rise of Graphene," *Nature Mater.*, vol. 6, no. 3, pp. 183–191, 2007.

[64] A. B. Kuzmenko, E. van Heumen, F. Carbone, and D. van der Marel, "Universal Optical Conductance of Graphite," *Phys. Rev. Lett.*, vol. 100, no. 11, p. 117401 (4pp), 2008.

[65] Q. Bao and K. P. Loh, "Graphene Photonics, Plasmonics, and Broadband Optoelectronic Devices," *ACS Nano*, vol. 6, no. 5, pp. 3677–3694, 2012.

[66] F. Wang, Y. Zhang, C. Tian, C. Girit, A. Zettl, M. Crommie, and Y. R. Shen, "Gate-Variable Optical Transitions in Graphene," *Science*, vol. 320, no. 5873, pp. 206–209, 2008.

[67] L. G. D. Arco, Y. Zhang, C. W. Schlenker, K. Ryu, M. E. Thompson, and C. Zhou, "Continuous, Highly Flexible, and Transparent Graphene Films by Chemical Vapor Deposition for Organic Photovoltaics," *ACS Nano*, vol. 4, no. 5, pp. 2865–2873, 2010.

[68] Y. Wang, X. Chen, Y. Zhong, F. Zhu, and K. P. Loh, "Large Area, Continuous, Few-Layered Graphene as Anodes in Organic Photovoltaic Devices," *Appl. Phys. Lett.*, vol. 95, no. 6, p. 063302 (3pp), 2009.

[69] Y. Wang, S. W. Tong, X. F. Xu, B. Özyilmaz, and K. P. Loh, "Graphene: Interface Engineering of Layer-by-Layer Stacked Graphene Anodes for High-Performance Organic Solar Cells," *Advanced Materials*, vol. 23, no. 13, pp. 1475–1475, 2011.

[70] F. Bonaccorso, Z. Sun, T. Hasan, and A. Ferrari, "Graphene Photonics and Optoelectronics," *Nature Photo.*, vol. 4, no. 9, pp. 611–622, 2010.

[71] D. S. Hecht, L. Hu, and G. Irvin, "Emerging Transparent Electrodes Based on Thin Films of Carbon Nanotubes, Graphene, and Metallic Nanostructures," *Advanced Materials*, vol. 23, no. 13, pp. 1482–1513, 2011.

[72] S. Bae, H. Kim, Y. Lee, X. Xu, J. Park, Y. Zheng, J. Balakrishnan, T. Lei, H. R. Kim, Y. I. Song, Y. J. Kim, K. S. Kim, B. Ozyilmaz, J. H. Ahn, B. H. Hong, and S. Iijima, "Roll-to-Roll Production of 30-inch Graphene Films for Transparent Electrodes," *Nature Nanotech.*, vol. 5, no. 8, pp. 574–578, 2010.

[73] P. Avouris, "Graphene: Electronic and Photonic Properties and Devices," *Nano Lett.*, vol. 10, no. 11, pp. 4285–4294, 2010.

[74] C. H. Liu, Y. C. Chang, T. B. Norris, and Z. Zhong, "Graphene Photodetectors with Ultra-Broadband and High Responsivity at Room Temperature," *Nature Nanotech.*, vol. 9, no. 4, pp. 273–278, 2014.

[75] B. E. A. Saleh and M. C. Teich, *Fundamentals of Photonics.* Wiley, 2009, ch. Semiconductor Photon Detectors, pp. 784–803.

[76] Z. Sun, T. Hasan, F. Torrisi, D. Popa, G. Privitera, F. Wang, F. Bonaccorso, D. M. Basko, and A. C. Ferrari, "Graphene Mode-Locked Ultrafast Laser," *ACS Nano*, vol. 4, no. 2, pp. 803–810, 2010.

[77] J. M. Dawlaty, S. Shivaraman, J. Strait, P. George, M. Chandrashekhar, F. Rana, M. G. Spencer, D.Veksler, and Y. Chen, "Measurement of the Optical Absorption Spectra of Epitaxial Graphene from Terahertz to Visible," *Appl. Phys. Lett.*, vol. 93, no. 13, p. 131905 (3pp), 2008.

[78] A. R. Wright, J. C. Cao, and C. Zhang, "Enhanced Optical Conductivity of Bilayer Graphene Nanoribbons in the Terahertz Regime," *Phys. Rev. Lett.*, vol. 103, no. 20, p. 207401 (4pp), 2009.

[79] F. T. Vasko and V. Ryzhii, "Photoconductivity of Intrinsic Graphene," *Phys. Rev. B*, vol. 77, no. 19, p. 195433 (8pp), 2008.

[80] J. Park, Y. H. Ahn, and C. Ruiz-Vargas, "Imaging of Photocurrent Generation and Collection in Single-Layer Graphene," *Nano Lett.*, vol. 9, no. 5, pp. 1742–1746, 2009.

[81] F. Xia, T. Mueller, R. G.-M. M. F. Y. Lin, J. Tsang, V. Perebeinos, and P. Avouris, "Photocurrent Imaging and Efficient Photon Detection in a Graphene Transistor," *Nano Lett.*, vol. 9, no. 3, pp. 1039–1044, 2009.

[82] F. Xia, T. Mueller, Y. Lin, A. Valdes-Garcia, and P. Avouris, "Ultrafast Graphene Photodetector," *Nature Nanotech.*, vol. 4, no. 12, pp. 839–843, 2009.

[83] Y. Kang, H. Liu, M. Morse, M. J. Paniccia, M. Zadka, S. Litski, G. Sarid, A. Pauchard, Y. Kuo, H. Chen, W. S. Zaoui, J. E. Bowers, A. Beling, D. C. McIntosh, X. Zheng, and J. C. Campbell, "Monolithic Germanium/Silicon Avalanche Photodiodes with 340 GHz Gain-Bandwidth Product," *Nature Photo.*, vol. 3, no. 1, pp. 59–63, 2009.

[84] E. J. H. Lee, K. Balasubramanian, R. T. Weitz, M. Burghard, and K. Kern, "Contact and Edge Effects in Graphene Devices," *Nature Nanotech.*, vol. 3, no. 8, pp. 486–490, 2008.

[85] A. Pospischil, M. Humer, M. M. Furchi, D. Bachmann, R. Guider, T. Fromherz, and T. Mueller, "CMOS-Compatible Graphene Photodetector Covering All Optical Communication Bands," *Nature Photo.*, vol. 7, no. 11, pp. 892–896, 2013.

[86] X. Xu, N. M. Gabor, J. S. Alden, A. M. van der Zande, and P. L. McEuen, "Photo-Thermoelectric Effect at a Graphene Interface Junction," *Nano Lett.*, vol. 10, no. 2, pp. 562–566, 2010.

[87] M. C. Lemme, F. H. L. Koppens, A. L. Falk, M. S. Rudner, H. Park, L. S. Levitov, and C. Marcus, "Gate-Activated Photoresponse in a Graphene pn Junction," *Nano Lett.*, vol. 11, no. 10, pp. 4134–4137, 2010.

[88] G. Konstantatos, M. Badioli, L. Gaudreau, J. Osmond, M. Bernechea, F. P. G. de Arquer, F. Gatti, and F. H. L. Koppens, "Hybrid Graphene-Quantum Dot Phototransistors with Ultrahigh Gain," *Nature Nanotech.*, vol. 7, no. 6, pp. 363–368, 2012.

[89] J. Yan, M.-H. Kim, J. A. Elle, A. B. Sushkov, G. S. Jenkins, H. M. Milchberg, M. S. Fuhrer, and H. D. Drew, "Dual-Gated Bilayer Graphene Hot-Electron Bolometer," *Nature Nanotech.*, vol. 7, no. 7, pp. 472–478, 2012.

[90] B. Lax, *Proceedings of the International Symposium on Quantum Electronics.* Columbia University Press, 1960, p. 428.

[91] R. Paiella, *Intersubband Transitions In Quantum Structures.* McGraw-Hill, 2006.

[92] R. N. Hall, G. E. Fenner, J. D. Kingsley, T. J. Soltys, and R. O. Carlson, "Coherent Light Emission From GaAs Junctions," *Phys. Rev. Lett.*, vol. 9, no. 9, pp. 366–368, 1962.

[93] Z. I. Alferov, V. M. Andreev, E. L. Portnoi, and M. K. Trukan, "AlAs-GaAs Heterojunction Injection Lasers with a Low Room-Temperature Threshold," *Fiz. Tekh. Poluprovodn*, vol. 3, pp. 1328–1332, 1969.

[94] I. Hayashi, M. B. Panish, P. W. Foy, and S. Sumski, "Junction Lasers Which Operate Continuously at Room Temperature," *Appl. Phys. Lett.*, vol. 17, no. 3, pp. 109–111, 1970.

[95] A. Cho, *Molecular Beam Epitaxy.* New York: AIP Press, Woodbury, 1994.

[96] L. Esaki and R. Tsu, "Superlattice and Negative Differential Conductivity in Semiconductors," *IBM Journal of Research and Development*, vol. 14, no. 1, pp. 61–65, 1970.

[97] R. F. Kazarinov and R. A. Suris, "Possibility of Amplification of Electromagnetic Waves in a Semiconductor with a Superlattice," *Fizika i Tekhnika Poluprovodnikov*, vol. 5, no. 4, pp. 797–800, 1971.

[98] R. Colombelli, F. Capasso, C. Gmachl, A. L. Hutchinson, D. L. Sivco, A. Tredicucci, M. C. Wanke, A. M. Sergent, and A. Y. Cho, "Far-Infrared Surface-Plasmon Quantum-Cascade Lasers at 21.5 μm and 24 μm Wavelengths," *Appl. Phys. Lett.*, vol. 78, no. 18, pp. 2620–2622, 2001.

[99] R. Köhler, A. Tredicucci, F. Beltram, H. E. Beere, E. Linfield, A. G. Davies, D. A. Ritchie, R. C. Iotti, and F. Rossi, "Terahertz Semiconductor-Heterostructure Laser," *Nature*, vol. 417, no. 6885, pp. 156–159, 2002, cited By (since 1996)1583.

[100] J. Faist, F. Capasso, D. L. Sivco, A. L. Hutchinson, S. G. Chu, and A. Y. Cho, "Short Wavelength ($\lambda \sim 3.4\mu m$) Quantum Cascade Laser Based on Strained Compensated InGaAs/AlInAs," *Appl. Phys. Lett.*, vol. 72, no. 6, pp. 680–682, 1998.

[101] S. Kumar, B. S. Williams, S. Kohen, Q. Hu, and J. L. Reno, "1.9 THz Quantum-Cascade Lasers with One-Well Injector," *Appl. Phys. Lett.*, vol. 88, no. 12, p. 121123 (3pp), 2006.

[102] C. Gmachl, F. Capasso, A. Tredicucci, D. L. Sivco, A. L. Hutchinson, S. N. Chu, and A. Y. Cho, "Noncascaded Intersubband Injection Lasers at $\lambda \approx 7.7\mu m$," *Appl. Phys. Lett.*, vol. 73, no. 26, pp. 3830–3832, 1998.

[103] F. Capasso, C. Gmachl, R. Paiella, A. Tredicucci, A. L. Hutchinson, D. L. Sivco, J. N. Baillargeon, A. Y. Cho, and H. C. Liu, "New Frontiers in Quantum Cascade Lasers and Applications," *IEEE J. Select. Topics Quantum Electron.*, vol. 6, no. 6, pp. 931–947, 2000.

[104] A. Bismuto, R. Terazzi, B. Hinkov, M. Beck, and J. Faist, "Fully Automatized Quantum Cascade Laser Design by Genetic Optimization," *Appl. Phys. Lett.*, vol. 101, no. 2, p. 021103, 2012.

[105] J. Faist, D. Hofstetter, M. Beck, T. Aellen, M. Rochat, and S. Blaser, "Bound-to-Continuum and Two-Phonon Resonance, Quantum-Cascade Lasers for High Duty Cycle, High-Temperature Operation," *IEEE J. Quantum Electron.*, vol. 38, no. 6, pp. 533–546, 2002.

[106] Q. J. Wang, C. Pflügl, L. Diehl, F. Capasso, T. Edamura, S. Furuta, M. Yamanishi, and H. Kan, "High Performance Quantum Cascade Lasers Based on Three-Phonon-Resonance Design," *Appl. Phys. Lett.*, vol. 94, no. 1, p. 011103 (3pp), 2009.

[107] Y. Bai, N. Bandyopadhyay, S. Tsao, E. Selcuk, S. Slivken, and M. Razeghi, "Highly Temperature Insensitive Quantum Cascade Lasers," *Appl. Phys. Lett.*, vol. 97, no. 25, p. 251104 (3pp), 2010.

[108] C. Gmachl, F. Capasso, D. L. Sivco, and A. Y. Cho, "Recent Progress in Quantum Cascade Lasers and Applications," *Rep. Prog. Phys.*, vol. 64, no. 11, pp. 1533–1601, 2001.

[109] J. Faist, F. Capasso, C. Sirtori, D. L. Sivco, J. N. Baillargeon, A. L. Hutchinson, S. G. Chu, and A. Y. Cho, "High Power MidInfrared ($\lambda \sim 5\mu m$) Quantum Cascade Lasers Operating Above Room Temperature," *Appl. Phys. Lett.*, vol. 68, no. 26, pp. 3680–3682, 1996.

[110] C. Gmachl, F. Capasso, A. Tredicucci, D. L. Sivco, R. Köhler, A. L. Hutchinson, and A. Y. Cho, "Dependence of the Device Performance on the Number of Stages in Quantum-Cascade Lasers," *IEEE J. Select. Topics Quantum Electron.*, vol. 5, no. 3, pp. 808–816, 1999.

[111] C. Sirtori, F. Capasso, J. Faist, A. L. Hutchinson, D. L. Sivco, and A. Cho, "Resonant Tunneling in Quantum Cascade Lasers," *IEEE J. Quantum Electron.*, vol. 34, no. 9, pp. 1722–1729, 1998.

[112] G. Scamarcio, F. Capasso, C. Sirtori, J. Faist, A. L. Hutchinson, D. L. Sivco, and A. Y. Cho, "High-Power Infrared (8-Micrometer Wavelength) Superlattice Lasers," *Science*, vol. 276, no. 5313, pp. 773–776, 1997.

[113] J. Faist, F. Capasso, C. Sirtori, D. L. Sivco, A. L. Hutchinson, M. S. Hybertsen, and A. Y. Cho, "Quantum Cascade Lasers without Intersubband Population Inversion," *Phys. Rev. Lett.*, vol. 76, no. 3, pp. 411–414, 1996.

[114] M. Helm, "Infrared Spectroscopy and Transport of Electrons in Semiconductor Superlattices," *Semiconductor Science and Technology*, vol. 10, no. 5, p. 557, 1995.

[115] J. Faist, F. Capasso, C. Sirtori, D. L. Sivco, A. L. Hutchinson, and A. Y. Cho, "Laser Action by Tuning the Oscillator Strength," *Nature*, vol. 387, no. 6635, pp. 777–782, 1997.

[116] C. Gmachl, A. Tredicucci, D. L. Sivco, A. L. Hutchinson, F. Capasso, and A. Y. Cho, "Bidirectional Semiconductor Laser," *Science*, vol. 286, no. 5440, pp. 749–752, 1999.

[117] R. Huber, F. Tauser, A. Brodschelm, M. Bichler, G. Abstreiter, and A. Leitenstorfer, "How Many-Particle Interactions Develop After Ultrafast Excitation of an Electron-Hole Plasma," *Nature*, vol. 414, no. 6861, pp. 286–289, 2001.

[118] R. Torre, P. Bartolini, and R. Righini, "Structural Relaxation in Supercooled Water by Time-Resolved Spectroscopy," *Nature*, vol. 428, no. 6980, pp. 296–299, 2004.

[119] P. Loza-Alvarez, C. T. A. Brown, D. T. Reid, W. Sibbett, and M. Missey, "High-Repetition-Rate Ultrashort-Pulse Optical Parametric Oscillator Continuously Tunable From 2.8 to 6.8 μm," *Opt. Lett.*, vol. 24, no. 21, pp. 1523–1525, 1999.

[120] W. S. Warren, H. Rabitz, and M. Dahleh, "Coherent Control of Quantum Dynamics: The Dream is Alive," *Science*, vol. 259, no. 5101, pp. 1581–1589, 1993.

[121] H. Okamoto and M. Tasumi, "Generation of Ultrashort Light Pulses in the Mid-Infrared (3000800 cm^{-1}) by four-wave mixing," *Optics Communications*, vol. 121, no. 1–3, pp. 63–68, 1995.

[122] T. Udem, R. Holzwarth, and T. W. Hansch, "Optical Frequency Metrology," *Nature*, vol. 416, no. 6877, pp. 233–237, 2002.

[123] C. Y. Wang, L. Kuznetsova, V. M. Gkortsas, L. Diehl, F. X. Kärtner, M. A. Belkin, A. Belyanin, X. Li, D. Ham, H. Schneider, P. Grant, C. Y. Song, S. Haffouz, Z. R. Wasilewski, H. C. Liu, and F. Capasso, "Mode-Locked Pulses

from Mid-Infrared Quantum Cascade Lasers," *Opt. Express*, vol. 17, no. 15, pp. 12 929–12 943, 2009.

[124] C. Gmachl, D. L. Sivco, R. Colombelli, and F. C. A. Y. Cho, "Ultra-Broadband Semiconductor Laser," *Nature*, vol. 415, no. 6874, pp. 883–887, 2002.

[125] C. Y. Wang, L. Diehl, A. Gordon, C. Jirauschek, F. X. Kärtner, A. Belyanin, D. Bour, S. Corzine, G. Höfler, M. Troccoli, J. Faist, and F. Capasso, "Coherent Instabilities in a Semiconductor Laser with Fast Gain Recovery," *Phys. Rev. A*, vol. 75, no. 3, p. 031802, 2007.

[126] A. Gordon, C. Y. Wang, L. Diehl, F. X. K. a, A. Belyanin, D. Bour, S. Corzine, G. Höfler, H. C. Liu, H. Schneider, T. Maier, M. Trocolli, J. Faist, and F. Capasso, "Multimode Regimes in Quantum Cascade Lasers: From Coherent Instabilities to Spatial Hole Burning," *Phys. Rev. A*, vol. 77, no. 5, p. 053804, 2008.

[127] H. Choi, T. B. Norris, T. Gresch, M. Giovannini, J. Faist, L. Diehl, and F. Capasso, "Femtosecond Dynamics of Resonant Tunneling and Superlattice Relaxation in Quantum Cascade Lasers," *Appl. Phys. Lett.*, vol. 92, no. 12, p. 122114 (3pp), 2008.

[128] H. A. Haus, "Mode-Locking of Lasers," *IEEE J. Select. Topics Quantum Electron.*, vol. 6, no. 6, pp. 1173–1185, 2000.

[129] A. Nagashima, N. Tejima, Y. Gamou, T. Kawai, and C. Oshima, "Electronic Structure of Monolayer Hexagonal Boron Nitride Physisorbed on Metal Surfaces," *Phys. Rev. Lett.*, vol. 75, no. 21, p. 3918 (4pp), 1995.

[130] T. Wehling, K. Novoselov, S. Morozov, E. Vdovin, M. Katsnelson, A. Geim, and A. Lichtenstein, "Molecular Doping of Graphene," *Nano Lett.*, vol. 8, no. 1, pp. 173–177, 2008.

[131] F. Zheng, K.-I. Sasaki, R. Saito, W. Duan, and B.-L. Gu, "Edge States of Zigzag Boron Nitride Nanoribbons," *J. Phys. Soc. Jpn.*, vol. 78, no. 7, pp. 074 713–1–074 713–6, 2009.

[132] Y. Ding, Y. Wang, and J. Ni, "Electronic Properties of Graphene Nanoribbons Embeded in Boron Nitride Sheets," *Appl. Phys. Lett.*, vol. 95, p. 123105 (3pp), 2009.

[133] X. Gao, Z. Zhou, Y. Zhao, S. Nagase, S. B. Zhang, and Z. Chen, "Comparative Study of Carbon and BN Nanographenes: Ground Electronic States and Energy Gap Engineering," *J. Phys. Chem. C*, vol. 112, no. 33, p. 12677 (6pp), 2008.

[134] L. Ci, L. Song, C. Jin, D. Jariwala, D. Wu, Y. Li, A. Srivastava, Z. F. Wang, K. Storr, L. Balicas, F. Liu, and P. M. Ajayan, "Atomic Layers of Hybridized Boron Nitride and Graphene Domains," *Nature Mater.*, vol. 9, no. 5, pp. 430–435, 2010.

[135] G. Seol and J. Guo, "Bandgap Opening in Boron Nitride Confined Armchair Graphene Nanoribbon," *Appl. Phys. Lett.*, vol. 98, no. 14, p. 143107 (3pp), 2011.

[136] H. Nematian, M. Moradinasab, M. Pourfath, M. Fathipour, and H. Kosina, "Optical Properties of Armchair Graphene Nanoribbons Embedded in Hexagonal Boron Nitride Lattices," *J. Appl. Phys.*, vol. 111, no. 9, p. 512 (6pp), 2012.

[137] T. van Mourik, M. Bühl, and M. P. Gaigeot, "Density Functional Theory Across Chemistry, Physics and Biology," *Philosophical transactions. Series A, Mathematical, physical, and engineering sciences*, vol. 372, pp. 1–5, 2011.

[138] F. N. Ajeel, A. M. Khudhair, and A. A. Mohammed, "Density Functional Theory Investigation of the Physical Properties of Dicyano Pyridazine Molecules," *International Journal of Science and Research (IJSR)*, vol. 4, no. 1, pp. 2334–2339, 2015.

[139] H. N. Najeeb, "Density Functional Theory and Semi-Empirical Investigations of Amino Tetrahydrofuran Molecules," *Physics and Materials Chemistry*, vol. 1, no. 2, pp. 21–26, 2013.

[140] H. Dorsett and A. White, *Overview of Molecular Modelling and Ab Initio Molecular Orbital Methods Suitable for Use with Energetic Materials.* Australia: DSTO Aeronautical and Maritime Research Laboratory, 2000.

[141] M. Orio, A. Dimitrios, D. A. Pantazis, and F. Neese, "Density Functional Theory," *Photosynthesis research*, vol. 102, no. 2-3, pp. 443–453, 2009.

[142] E. Engel and R. M. Dreizler, *Density Functional Theory.* Springer, 2011.

[143] J. B. Staunton, "The Electronic Structure of Magnetic Transition Metallic Materials," *Reports on Progress in Physics*, vol. 57, no. 12, p. 1289 (57pp), 1994.

[144] P. Elliott and K. Burke, "Non-Empirical Derivation of the Parameter in the B88 Exchange Functional," *Canadian Journal of Chemistry*, vol. 87, no. 10, pp. 1485–1491, 2009.

[145] J. P. Perdew, A. Ruzsinszky, J. Tao, V. N. Staroverov, G. E. Scuseria, and G. I.Csonka, "Prescription for the Design and Selection of Density Functional Approximations: More Constraint Satisfaction with Fewer Fits," *The Journal of Chemical Physics*, vol. 123, no. 6, p. 062201 (9pp), 2005.

[146] C. Fiolhais, F. Nogueira, and M. A. L. Marques, Eds., *A Primer in Density Functional Theory.* Springer Berlin Heidelberg, 2003.

[147] J. P. Perdew, J. A. Chevary, S. Vosko, K. A. Jackson, M. R. Pederson, D. J. Singh, and C. Fiolhais, "Atoms, Molecules, Solids, and Surfaces: Applications of the Generalized Gradient Approximation for Exchange and Correlation," *Phys. Rev. B*, vol. 46, no. 11, pp. 6671–6687, 1992.

[148] A. D. Becke, "Density-Functional Exchange-Energy Approximation with Correct Asymptotic Behavior," *Phys. Rev. A*, vol. 38, no. 6, pp. 3098–3100.

[149] D. C. Langreth and M. J. Mehl, "Beyond the Local-Density Approximation in Calculations of Ground-State Electronic Properties," *Phys. Rev. B*, vol. 28, no. 4, pp. 1809–1834, 1983.

[150] P. T. Yu and M. Cardona, *Fundamentals of Semiconductors: Physics and Materials Properties.* Berlin: Springer, 2001.

[151] H. Hsu and L. E. Reichl, "Selection Rule for the Optical Absorption of Graphene Nanoribbons," *Phys. Rev. B*, vol. 76, no. 4, p. 045418 (5pp), 2007.

[152] J. M. Soler, E. Artacho, J. D. Gale, A. García, J. Junquera1, P. Ordejón, and D. Sánchez-Portal, "The SIESTA Method for Ab Initio Order-N Materials Simulation," *J. Phys.: Condens. Matter*, vol. 14, pp. 2745–2779, 2002.

[153] R. Saito, G. Dresselhaus, and M. Dresselhaus, *Physical Properties of Carbon Nanotubes.* London: Imperial College Press, 1998.

[154] Y. Hancock, A. Uppstu, K. Saloriutta, A. Harju, and M. J. Puska, "Generalized Tight-Binding Transport Model for Graphene Nanoribbon-Based Systems," *Phys. Rev. B*, vol. 81, p. 245402 (6pp), 2010.

[155] D. Gunlycke and C. White, "Tight-Binding Energy Dispersions of Armchair-Edge Graphene Nanostrips," *Phys. Rev. B*, vol. 77, p. 115116 (6pp), 2008.

[156] M. Freitag, Y. Martin, J. Misewich, R. Martel, and P. Avouris, "Photoconductivity of Single Carbon Nanotubes," *Nano Lett.*, vol. 3, no. 8, pp. 1067–1071, 2003.

[157] S. Tasaki, K. Maekawa, and T. Yamabe, "π-Band Contribution to the Optical Properties of Carbon Nanotubes: Effects of Chirality," *Phys. Rev. B*, vol. 57, no. 15, pp. 9301–9318, 1998.

[158] A. Grüneis, R. Saito, G. G. Samsomidze, T. Kimura, M. A. Pimenta, A. Jorio, A. G. S. Filho, G. D. Dresselhaus, and M. S. Dresselhaus, "Inhomogeneous Optical Absorption Around the K Point in Graphite and Carbon Nanotubes," *Phys. Rev. B*, vol. 67, p. 165402 (7pp), 2003.

[159] M. Pourfath, *Non-Equilibrium Green's Function Method for Nanoscale Device Simulation.* Vienna: Springer, 2014.

[160] L. E. Henrickson, "Nonequilibrium Photocurrent Modeling in Resonant Tunneling Photodetectors," *J. Appl. Phys.*, vol. 91, no. 10, pp. 6273–6281, 2002.

[161] D. A. Stewart and F. Leonard, "Photocurrents in Nanotube Junctions," *Phys. Rev. Lett.*, vol. 93, no. 10, p. 107401, 2004.

[162] G. Dresselhaus and M. S. Dresselhaus, "Fourier Expansion for the Electronic Energy Bands in Silicon and Germanium," *Phys. Rev.*, vol. 160, no. 3, pp. 649–679, 1967.

[163] T. G. Pedersen, K. Pedersen, and T. B. Kriestensen, "Optical Matrix Elements in Tight-Binding Calculations," *Phys. Rev. B*, vol. 63, p. 201101 (4pp), 2001.

[164] U. Aeberhard and H. Morf, "Microscopic Momequilibrium Theory of Quantum Well Solar Cells," *Phys. Rev. B*, vol. 77, p. 125343 (9pp), 2008.

[165] R. Lake, G. Klimeck, R. C. Bowen, and D. Jovanovic, "Single and Multiband Modeling of Quantum Electron Transport Through Layered Semiconductor Devices," *J. Appl. Phys.*, vol. 81, no. 12, pp. 7845–7869, 1997.

[166] D. C. Harris and M. D. Bertolucci, *Symmetry and Spectroscopy: Introduction to Vibrational and Electronic Spectroscopy.* Courier Dover Publications, 1989.

[167] S. V. Goupalov, "Optical Transitions in Carbon Nanotubes," *Phys. Rev. B*, vol. 72, p. 195403 (5pp), 2005.

[168] H. Zheng, Z. Wang, T. Luo, Q. Shi, and J. Chen, "Analytical Study of Electronic Structure in Armchair Graphene Nanoribbons," *Phys. Rev. B*, vol. 75, no. 16, p. 165414 (6pp), 2007.

[169] K. i. Sasaki, K. Kato, Y. Tokura, K. Oguri, and T. Sogawa, "Theory of Optical Transitions in Graphene Nanoribbons," *Phys. Rev. B*, vol. 84, p. 085458 (11pp), 2011.

[170] H. C. Chung, M. H. Lee, C. P. Chang, and M. F. Lin, "Exploration of Edge-Dependent Optical Selection Rules for Graphene Nanoribbons," *Opt. Express*, vol. 19, no. 23, pp. 23 350–23 363, 2011.

[171] M. Pourfath, O. Baumgartner, S. Kosina, and S. Selberherr, "Performance Evaluation of Graphene Nanoribbon Infrared Photodetectors," in *Proceedings of the 9th International Conference on Numerical Simulation of Optoelectronic Devices*, Gwangju, 2009, pp. 13–14, Talk: Numerical Simulation of Optoelectronic Devices (NUSOD).

[172] K. Wakabayashi, K. I. Sasaki, T. Nakanishi, and T. Enoki, "Electronic States of Graphene Nanoribbons and Analytical Solutions," , vol. 11, p. 054504 (18pp), 2010.

[173] A. K. Gupta, O. E. Alon, and N. Moiseyev, "Generation and Control of High-Order Harmonics by the Interaction of an Infrared Laser with a Thin Graphite Layer," *Phys. Rev. B*, vol. 68, p. 205101 (13pp), 2003.

[174] L. Esaki and L. L. Chang, "New Transport Phenomenon in a Semiconductor "Superlattice","" *Phys. Rev. Lett.*, vol. 33, no. 8, pp. 495–498, 1974.

[175] L. L. Chang, L. Esaki, and R. Tsu, "Resonant Tunneling in Semiconductor Double Barriers," *Appl. Phys. Lett.*, vol. 24, no. 12, pp. 593–595, 1974.

[176] S. Ciraci and I. P. Batra, "Long-Range Order and Segregation in Semiconductor Superlattices," *Phys. Rev. Lett.*, vol. 58, no. 20, pp. 2114–2117, 1987.

[177] ——, "Self-Consistent Study of Confined States in Thin GaAs-AlAs Superlattices," *Phys. Rev. B*, vol. 36, no. 2, pp. 1225–1232, 1987.

[178] Y.-W. Son, M. Cohen, and S. Louie, "Half-Metallic Graphene Nanoribbons," *Nature (London)*, vol. 444, no. 7117, pp. 347–349, 2006.

[179] A. Y. Goharrizi, M. Pourfath, M. Fathipour, H. Kosina, and S. Selberherr, "An Analytical Model for Line-Edge Roughness Limited Mobility of Graphene Nanoribbons," *IEEE Trans. Electron Devices*, vol. 58, no. 11, pp. 3725–3735, 2011.

[180] Y. Yang and R. Murali, "Impact of Size Effect on Graphene Nanoribbon Transport," *IEEE Electron Device Lett.*, vol. 31, no. 3, pp. 237–239, 2010.

[181] A. Y. Goharrizi, M. Pourfath, M. Fathipour, H. Kosina, and S. Selberherr, "A Numerical Study of Line-Edge Roughness Scattering in Graphene Nanoribbons," *IEEE Trans. Electron Devices*, vol. 59, no. 2, pp. 433–440, 2012.

[182] D. Gunlycke and C. T. White, "Scaling of the Localization Length in Armchair-Edge Graphene Nanoribbons," *Phys. Rev. B*, vol. 81, p. 075434 (6pp), 2010.

[183] S. Dubois, A. Lopez-Bezanilla, A. Cresti, F. Triozon, B. Biel, J. Charlier, and S. Roche, "Quantum Transport in Graphene Nanoribbons: Effects of Edge Reconstruction and Chemical Reactivity," *ACS Nano*, vol. 4, no. 4, pp. 1971–1976, 2010.

[184] A. Y. Goharrizi, M. Pourfath, M. Fathipour, and H. Kosina, "Device Performance of Graphene Nanoribbon Field-Effect Transistors in the Presence of Line-Edge Roughness," *IEEE Trans. Electron Devices*, vol. 59, no. 12, pp. 3527–3532, 2012.

[185] Y. Yao, A. J. Hoffman, and C. F. Gmachl, "Mid-Infrared Quantum Cascade Lasers," *Nature Photonics*, vol. 6, no. 7, pp. 432–439, 2012.

[186] J. R. Freeman, J. Maysonnave, H. E. Beere, D. A. Ritchie, J. Tignon, and S. S. Dhillon, "Electric Field Sampling of Modelocked Pulses from a Quantum Cascade Laser," *Opt. Express*, vol. 21, no. 13, pp. 16 162–16 169, 2013.

[187] J. M. Dudley, G. Genty, and S. Coen, "Supercontinuum Generation in Photonic Crystal Fiber," *Rev. Mod. Phys.*, vol. 78, no. 4, pp. 1135–1184, 2006.

[188] E. A. Gibson, A. Paul, N. Wagner, R. Tobey, D. Gaudiosi, S. Backus, I. P. Christov, A. Aquila, E. M. Gullikson, D. T. Attwood, M. M. Murnane, and H. C. Kapteyn, "Coherent Soft X-Ray Generation in the Water Window with Quasi-Phase Matching," *Science*, vol. 302, no. 5642, pp. 95–98, 2003.

[189] R. Paiella, F. Capasso, C. Gmachl, H. Hwang, D. Sivco, A. Hutchinson, A. Y. Cho, and H. C. Liu, "Monolithic Active Mode Locking of Quantum Cascade Lasers," *Appl. Phys. Lett.*, vol. 77, no. 2, pp. 169–171, 2000.

[190] R. Paiella, F. Capasso, C. Gmachl, D. L. Sivco, J. N. Bailargeon, A. L. Hutchinson, A. Y. Cho, and H. C. Liu, "Self-Mode-Locking of Quantum Cacade Lasers with Giant Ultrafast Optical Nonlinearities," *Science*, vol. 290, pp. 1739–1742, 2001.

[191] V.-M. Gkortsas, C. Wang, L. Kuznetsova, L. Diehl, A. Gordon, C. Jirauschek, M. A. Belkin, A. Belyanin, F. Capasso, and F. X. Kärtner, "Dynamics of Actively Mode-Locked Quantum Cascade Lasers," *Opt. Express*, vol. 18, no. 13, pp. 13 616–13 630, 2010.

[192] A. Daničić, J. Radovanović, V. Milanović, D. Indjin, and Z. Ikonić, "Optimization and Magnetic-Field Tunability of Quantum Cascade Laser for Applications in Trace Gas Detection and Monitoring," *J. Phys. D: Appl. Phys.*, vol. 43, no. 4, p. 045101, 2010.

[193] M. T. Arafin, N. Islam, S. Roy, and S. Islam, "Performance Optimization for Terahertz Quantum Cascade Laser at Higher Temperature Using Genetic Algorithm," *Opt. Quant. Electron.*, vol. 44, no. 15, pp. 701–715, 2012.

[194] M. Beck, D. Hofstetter, T. Aellen, J. Faist, U. Oesterle, M. Ilegems, E. Gini, and H. Melchior, "Continuous Wave Operation of a Mid-Infrared Semiconductor Laser at Room Temperature," *Science*, vol. 295, no. 5553, pp. 301–305, 2002.

[195] Y. Bai, N. Bandyopadhyay, S. Tsao, S. Slivken, and M. Razeghi, "Room Temperature Quantum Cascade Lasers with 27% Wall Plug Efficiency," *Appl. Phys. Lett.*, vol. 98, no. 18, p. 181102, 2011.

[196] R. Maulini, A. Lyakh, A. Tsekoun, R. Go, and C. K. N. Patel, "High Average Power Uncooled Mid-Wave Infrared Quantum Cascade Lasers," *Electronics Letters*, vol. 47, no. 6, pp. 395–397, 2011.

[197] P. A. Sanchez-Serrano, D. Wong-Campos, S. Lopez-Aguayo, and J. C. Gutiérrez-Vega, "Engineering of Nondiffracting Beams with Genetic Algorithms," *Opt. Lett.*, vol. 37, no. 24, pp. 5040–5042, 2012.

[198] D. Gagnon, J. Dumont, and L. J. Dubé, "Multiobjective Optimization in Integrated photonics Design," *Opt. Lett.*, vol. 38, no. 13, pp. 2181–2184, 2013.

[199] R. Poli, J. Kennedy, and T. Blackwell, "Particle Swarm Optimization," *Swarm Intelligence*, vol. 1, no. 1, pp. 33–57, 2007.

[200] F. Grimaccia, M. Mussetta, and R. E. Zich, "Genetical Swarm Optimization: Self-Adaptive Hybrid Evolutionary Algorithm for Electromagnetics," *Antennas and Propagation, IEEE Transactions on*, vol. 55, no. 3, pp. 781–785, 2007.

[201] R. Y. Wang, W. P. Lee, and Y. T. Hsiao, "A New Cooperative PSO Approach for the Optimization of Multimodal Functions," in *Proceedings of the World Congress on Engineering, 2012, WCE*, 2012, pp. 418–424.

[202] D. Indjin, P. Harrison, R. W. Kelsall, and Z. Ikonić, "Self-Consistent Scattering Theory of Transport and Output Characteristics of Quantum Cascade Lasers," *J. Appl. Phys.*, vol. 91, no. 11, pp. 9019–9026, 2002.

[203] C. Wang, F. Grillot, V. I. Kovanis, J. D. Bodyfelt, and J. Even, "Modulation Properties of Optically Injection-Locked Quantum Cascade Lasers," *Opt. Lett.*, vol. 38, no. 11, pp. 1975–1977, 2013.

[204] G. Milovanovic and H. Kosina, "A Semiclassical Transport Model for Quantum Cascade Lasers Based on the Pauli Master Equation," *J. Comp. Electronics*, vol. 9, no. 3-4, pp. 211–217, 2010.

[205] R. Terazzi and J. Faist, "A Density Matrix Model of Transport and Radiation in Quantum Cascade Lasers," *New J. Phys.*, vol. 12, no. 3, p. 033045, 2010.

[206] T. Kubis, C. Yeh, P. Vogl, A. Benz, G. Fasching, and C. Deutsch, "Theory of Nonequilibrium Quantum Transport and Energy Dissipation in Terahertz Quantum Cascade Lasers," *Phys. Rev. B*, vol. 79, p. 195323, 2009.

[207] A. Wacker, M. Lindskog, and D. O. Winge, "Nonequilibrium Green's Function Model for Simulation of Quantum Cascade Laser Devices Under Operating Conditions," *IEEE J. Select. Topics Quantum Electron.*, vol. 19, no. 5, pp. 1–11, 2013.

[208] G. Beji, Z. Ikonić, C. A. Evans, D. Indjin, and P. Harrison, "Coherent Transport Description of the Dual-Wavelength Ambipolar Terahertz Quantum Cascade Laser," *J. Appl. Phys.*, vol. 109, no. 1, p. 013111, 2011.

[209] O. Baumgartner, Z. Stanojevic, and H. Kosina, "Efficient Simulation of Quantum Cascade Lasers Using the Pauli master Equation," in *Simulation of Semiconductor Processes and Devices (SISPAD)*, 2011, pp. 91–94.

[210] R. C. Iotti and F. Rossi, "Nature of Charge Transport in Quantum-Cascade Lasers," *Phys. Rev. Lett.*, vol. 87, no. 14, p. 146603 (4pp), 2001.

[211] C. Weber, A. Wacker, and A. Knorr, "Density-Matrix Theory of the Optical Dynamics and Transport in Quantum Cascade Structures: The Role of Coherence," *Phys. Rev. B*, vol. 79, no. 16, p. 165322 (14pp), 2009.

[212] M. V. Fischetti, "Master-Equation Approach to the Study of Electronic Transport in Small Semiconductor Devices," *Phys. Rev. B*, vol. 59, no. 7, pp. 4901–4917, 1999.

[213] M. Karner, A. Gehring, S. Holzer, M. Pourfath, M. Wagner, W. Goes, M. Vasicek, O. Baumgartner, C. Kernstock, K. Schnass, G. Zeiler, T. Grasser, H. Kosina, and S. Selberherr, "VSP-A Multi-Purpose Schrödinger-Poisson Solver for TCAD Applications," *J. Comp. Electronics*, vol. 6, no. 1-3, pp. 179–182, 2007.

[214] O. Baumgartner, Z. Stanojevic, K. Schnass, M. Karner, and H. Kosina, "VSP -a Quantum-Electronic Simulation Framework," *Journal of Computational Electronics*, vol. 12, no. 4, pp. 701–721, 2013.

[215] C. Jirauschek, G. Scarpa, P. Lugli, M. Vitiello, and G. Scamarcio, "Comparative Analysis of Resonant Phonon THz Quantum Cascade Lasers," *J. Appl. Phys.*, vol. 101, no. 8, p. 086109 (3pp), 2007.

[216] R. C. Iotti, E. Ciancio, and F. Rossi, "Quantum Transport Theory for Semiconductor Nanostructures: A Density-Matrix Formulation," *Phys. Rev. B*, vol. 72, no. 12, p. 125347 (21pp), 2005.

[217] O. Baumgartner, Z. Stanojevic, and H. Kosina, *Monte Carlo Methods and Applications*, K. K. Sabelfeld and I. Dimov, Eds.   Berlin: De Gruyter, 2012.

[218] E. S. Peer, F. van den Bergh, and A. Engelbrecht, "Using Neighbourhoods with the Guaranteed Convergence PSO," in *Swarm Intelligence Symposium, 2003. SIS '03. Proceedings of the 2003 IEEE*, 2003, pp. 235–242.

[219] Y. Shi and R. Eberhart, "A Modified Particle Swarm Optimizer," in *Evolutionary Computation Proceedings, 1998. IEEE World Congress on Computational Intelligence., The 1998 IEEE International Conference on*, 1998, pp. 69–73.

[220] J. Faist, *Quantum Cascade Lasers*.   Oxford: Oxford University Press, 2013.

[221] C. Gmachl, A. Tredicucci, F. Capasso, A. L. Hutchinson, D. L. Sivco, J. N. Baillargeon, and A. Y. Cho, "High-Power $\approx 8\mu m$ Quantum Cascade Lasers with Near Optimum Performance," *Appl. Phys. Lett.*, vol. 72, no. 24, pp. 3130–3132, 1998.

[222] S. Kumar, B. S. Williams, S. Kohen, Q. Hu, and J. L. Reno, "Continuous-Wave Operation of Terahertz Quantum-Cascade Lasers Above Liquid-Nitrogen Temperature," *Appl. Phys. Lett.*, vol. 84, no. 14, pp. 2494–2496, 2004.

[223] A. Benz, G. Fasching, A. M. Andrews, M. Martl, K. Unterrainer, T. Roch, W. Schrenk, S. Golka, and G. Strasser, "Influence of Doping on the Performance of Terahertz Quantum-Cascade Lasers," *Appl. Phys. Lett.*, vol. 90, no. 10, p. 101107 (3pp), 2007.

[224] H. Risken and K. Nummedal, "Self-Pulsing in Lasers," *J. Appl. Phys.*, vol. 39, no. 10, pp. 4662–4672, 1968.

[225] R. Graham and H. Haken, "Quantum Theory of Light Propagation in a Fluctuating Laser-Active Medium," *Zeitschrift für Physik*, vol. 213, no. 5, pp. 420–450, 1968.

[226] B. F. Levine, K. K. Choi, C. Bethea, J. Walker, and R. J. Malik, "New 10 μm Infrared Detector Using Intersubband Absorption in Resonant Tunneling GaAlAs Superlattices," *Appl. Phys. Lett.*, vol. 50, no. 16, pp. 1092–1094, 1987.

[227] F. R. Giorgetta, E. Baumann, M. Graf, Q. Yang, C. Manz, K. Kohler, H. E. Beere, D. A. Ritchie, E. Linfield, A. G. Davies, Y. Fedoryshyn, H. Jackel, M. Fischer, J. Faist, and D. Hofstetter, "Quantum Cascade Detectors," *IEEE J. Quantum Electron.*, vol. 45, no. 8, pp. 1039–1052, 2009.

[228] H. Schneider, P. Koidl, F. Fuchs, B. Dischler, K. Schwarz, and J. D. Ralston, "Photovoltaic Intersubband Detectors for $3 - 5\mu$m Using GaAs Quantum Wells Sandwiched Between AlAs Tunnel Barriers," *Semiconductor Science and Technology*, vol. 6, no. 12C, pp. C120–C123, 1991.

[229] H. Schneider, K. Kheng, M. Ramsteiner, J. D. Ralston, F. Fuchs, and P. Koidl, "Transport Asymmetry and Photovoltaic Response in (AlGa)As/AlAs/GaAs/(AlGa)As SingleBarrier QuantumWell Infrared Detectors," *Appl. Phys. Lett.*, vol. 60, no. 12, pp. 1471–1473, 1992.

[230] H. Schneider, "Optimized Performance of Quantum Well Intersubband Infrared Detectors: Photovoltaic Versus Photoconductive Operation," *J. Appl. Phys.*, vol. 74, no. 7, pp. 4789–4791, 1993.

[231] D. Hofstetter, M. Beck, and J. Faist, "Quantum-Cascade-Laser Structures as Photodetectors," *Appl. Phys. Lett.*, vol. 81, no. 15, pp. 2683–2685, 2002.

[232] L. Gendron, M. Carras, A. Huynh, V. Ortiz, C. Koeniguer, and V. Berger, "Quantum Cascade Photodetector," *Appl. Phys. Lett.*, vol. 85, no. 14, pp. 2824–2826, 2004.

List of Publications

Publications in Scientific Journals

[1] **M. Moradinasab**, M. Pourfath, H. Kosina: "Numerical Study of Graphene Superlattice-Based Photodetectors"; IEEE Transaction on Elecron Devices, 62 (2015), 593-600.

[2] **M. Moradinasab**, M. Pourfath, H. Kosina: "Performance Optimization and Instability Study"; IEEE Journal of Quantum Electronics, 51 (2015), 1-7.

[3] **M. Moradinasab**, H. Nematian, M. Pourfath, H. Kosina: "Analytical Models of Approximations for Wave Functions and Energy Dispersion in Zigzag Graphene Nanoribbons"; Journal of Applied Physics, 111 (2012), 7; 074318-1 - 074318-9.

[4] H. Nematian, **M. Moradinasab**, M. Pourfath, H. Kosina: "Optical Properties of Armchair Graphene Nanoribbons Embedded in Hexagonal Boron Nitride Lattices"; Journal of Applied Physics, 111 (2012), 9; 093512-1 - 093512-6.

[5] M. Noei, **M. Moradinasab**, M. Fathipour: "A Computational Study of Ballistic Graphene Nanoribbon Field Effect Transistors"; Physica E: Low-dimensional Systems and Nanostructures, 44 (2012), 7-8; 1780 - 1786.

Publications in Conference Proceedings

[1] <u>**M. Moradinasab**</u>, M. Pourfath, H. Kosina: "Improved Active Region Designs for Mode Locking in Quantum Cascade Lasers"; Poster: International Quantum Cascade Lasers School & Workshop, Policoro (Matera), Italy; 2014-09-07 - 2014-09-12; in "International Quantum Cascade Lasers School & Workshop 2014", (2014), 182-183.

[2] <u>**M. Moradinasab**</u>, M. Pourfath, M. Fathipour, H. Kosina: "A Numerical Study of Line-Edge Roughness in Graphene Superlattice-Based Photodetectors"; Talk: International Conference on Numerical Simulation of Optoelectronic Devices (NUSOD), Palma de Mallorca, Spain; 2014-09-01 - 2014-09-04; in "Proceedings of the 14th International Conference on Numerical Simulation of Optoelectronic Devices", (2014), 1-2.

[3] **M. Moradinasab**, M. Pourfath, H. Kosina: "An Instability Study in Terahertz Quantum Cascade Lasers"; Talk: Int. Conf. on Superlattices, Nanostructures and Nanodevices (ICSNN), Savannah, GA, USA; 2014-08-03 - 2014-08-08; in "Proceedings of International Conference on Superlattices, Nanostructures and Nanodevices (ICSNN)", (2014), 10.

[4] **M. Moradinasab**, M. Pourfath, H. Kosina: "Spin Filtering in Zigzag Graphene Nanoribbons Using 7-5 Defects"; Poster: Graphene Week, Chemnitz, Germany; 2013-06-02 - 2013-06-07; in "Book of Abstracts", (2013), 250.

[5] **M. Moradinasab**, H. Karamitaheri, M. Pourfath, H. Kosina: "On the Role of Stone-Wales Defects on the Performance of Graphene Nanoribbon Photo Detectors"; Poster: Graphene Week, Delft, Netherlands; 2012-06-04 - 2012-06-08; in "Book of Abstracts", (2012).

[6] **M. Moradinasab**, H. Nematian, M. Noei, M. Pourfath, M. Fathipour, H. Kosina: "Edge Roughness Effects on the Optical Properties of Zigzag Graphene Nanoribbons: A First Principles Study"; Poster: International Workshop on Computational Electronics (IWCE), Madison, WI, USA; 2012-05-22 - 2012-05-25; in "Proceedings of the 15th International Workshop on Computational Electronics (IWCE 2012)", (2012), 249 - 250.

[7] H. Nematian, **M. Moradinasab**, M. Noei, M. Pourfath, M. Fathipour, H. Kosina: "A Theoretical Study of BN-Confined Graphene Nanoribbon Based Resonant Tunneling Diodes"; Poster: International Workshop on Computational Electronics (IWCE), Madison, WI, USA; 2012-05-22 - 2012-05-25; in "Proceedings of the 15th International Workshop on Computational Electronics (IWCE 2012)", (2012), 217 - 218.

[8] **M. Moradinasab**, H. Nematian, M. Pourfath, M. Fathipour, H. Kosina: "Theoretical Study of Single and Bilayer Graphene Nanoribbons Photodetectors"; Meeting of the Electrochemical Society (ECS), Seattle, Washington, USA; 2012-05-06 - 2012-05-10; in "ECS Meeting", (2012).

[9] **M. Moradinasab**, M. Pourfath, O. Baumgartner, H. Kosina: "Performance Optimization and Instability Study in Ring Cavity Quantum Cascade Lasers"; Poster: The 12th International Conference on Intersubband Transitions in Quantum Wells (ITQW), New York, USA; 2013-09-15 - 2013-09-20.

106

	Author	Co-author	Total
Journals	3	2	5
Conferences	8	1	9
Total	11	3	14

Publication statistics from scholar.google.com: Citations=34, h-index=4, i10-index=2.

Curriculum Vitae

Since December 2011
>Vienna University of Technology, Austria
>PhD program at the Institute for Microelectronics

September 2008 – February 2011
>University of Tehran, Tehran, Iran
>PhD by course at the School of Electrical and Computer Engineering

September 2006 – September 2008
>University of Tehran, Tehran, Iran
>Graduate program in micro- and nano-electronic devices at the School of Electrical Engineering
>Masters's Thesis: "Modeling and Application of CNFETs"

September 2002 – September 2006
>Bachelor's of Electrical Engineering
>Concentration: Electronics circuits
>Graduation with high distinction and outstanding academic achievement